Development of 13.5-meter-tall Vibration Isolation System for the Main Mirrors in KAGRA

Koki Okutomi

January 10, 2019

Abstract

The direct detection of gravitational waves by Advanced Laser Interferometer Gravitational wave Observatory (LIGO) has triggered the birth of a new window in astronomy. The number of detected events with enough confidence amounts to ten for binary black hole mergers and one for a binary neutron star merger. As for the binary neutron star merger GW170817, starting with the early alert of gravitational wave detection by LIGO and Virgo, follow-up observations of the source with multiband electromagnetic telescopes were performed which yielded novel information of astrophysics and cosmology. Now we are quite sure that gravitational wave observations will play an important role in revealing a hidden side of the universe in the future.

KAGRA is a 3-km interferometric gravitational wave telescope constructed in Japan. The KAGRA interferometer has two unique features among the current 2nd-generation advanced detectors which are that it is located at an underground site with lower seismic disturbance, and that it uses cryogenic sapphire mirrors in order to reduce thermal noise. Since the location of KAGRA is far from both LIGO and Virgo, the participation of KAGRA in the global observatory network can offer benefits of not only accurate false positive rejection but also better source localization, better sky coverage, and more precise parameter estimation. At present, KAGRA is in the process of completing full configuration of the interferometer toward the joint observation with the LIGO and Virgo detectors scheduled in 2019.

Vibration isolation systems are the key instruments to suppress mirror fluctuation introduced by continuous and random seismic motion. Even in a quiet underground environment, since gravitational wave observation with the KAGRA interferometer requires spectral displacement fluctuation of the mirror to be less than $10^{-19}\,\mathrm{m/Hz^{1/2}}$ in its observational band above 10 Hz, one needs to attenuate the vibration transmission from the ground to the mirror by 8–10 orders of magnitude. This level of seismic attenuation can be acquired by suspending the mirror at the bottom of a multi-stage pendulum called suspension system, which provides vibration filtering at high frequencies above its mechanical resonances. The suspension system also serves as an interface of the interferometer control. The position and attitude of the mirror can be monitored and controlled with local sensors and actuators mounted on the suspension stages so that the optical cavities in the interferometer are kept in the resonant condition. Although the suspension system will enhance the amplitude of the mirror fluctua-

tion at the mechanical resonant frequencies outside of the observation band ($< 1\,\mathrm{Hz}$), it can be also suppressed by active feedback control with the electric instruments.

The study in this thesis develops the vibration isolation system for the main mirrors (test masses) in KAGRA, which is so-called Type-A suspension. The Type-A suspension is the largest pendulum with totally nine stages and 13.5-meter tall. It consists of two primary compositions that are the tower part representing top five stages at room temperatures, and the cryogenic payload representing bottom four stages at cryogenic temperatures ($\sim 20\,\mathrm{K}$). This study focuses on the tower part since the vibration isolation performance of whole the suspension system is determined by the installation and adjustments of the low-frequency oscillators such as inverted pendulums and geometric anti-springs (GASs) implemented at the top five stages.

The performance tests demonstrate that the installed Type-A tower system basically has the designed dynamic characteristics which satisfies the requirements. The frequency responses of the Type-A tower are measured and compared to the predictions of the nominal model. Although there is some amount of deviation, the obtained frequency responses can be regarded as acceptable to achieve the required vibration isolation performances except for the vertical direction. As for the vertical direction, the dynamics of the Type-A tower shows discrepancies between the measurement results and the model predictions, in particular in the mode shapes of its higher order resonances. It is suspected that the higher order oscillatory behavior has stronger dependence on the divergence of the mechanical parameters from the nominal values. However, due to the facts that the higher order modes have smaller impact on the RMS residual motion and that the measured mode frequencies are roughly distributed as expected, the discrepancies in the vertical mode dynamics seem to be within the permissible range. This tolerance is also plausible from the measured displacement spectrum at the dummy payload which is suspended instead of the actual cryogenic payload. One problem still remains is the effect of couplings from non-straightforwardly-controllable degrees of freedom such as a tilt of the middle GAS filter stages. The impact of the couplings on the test mass or the interferometer should be confirmed after integration with the cryogenic payload.

In two kinds of damping control implemented in the performance tests, torsion mode damping is firstly engaged at the bottom stage of the Type-A tower. Since a major fraction of the height of the Type-A suspension is accounted by a series of single suspension wires, the system possesses a behavior of a torsion pendulum with extremely low stiffness and then have a long duration of the torsional modes which turns to an issue in stabilizing alignment of the mirror. The Type-A tower is responsible to address this issue by providing a function of active damping control at the tower's bottom stage. The test of torsion mode damping proves that the long exponential decay time of the resonances can be successfully reduced to less than 1 minute by the active feedback control. In addition, the in-loop sensor indicates that the RMS residual angular fluctuation in torsion is suppressed sufficiently to a level of

acquiring arm cavity lock. Therefore, it is concluded that the Type-A tower has satisfactory performance of the torsion mode damping.

This study also presents an advanced control scheme called modal damping. The modal damping processes feedback signals in a decoupled modal basis instead of a conventional Cartesian basis, allowing us to simplify the servo design optimization and to access efficient actuation for a coupled oscillatory system. The control test demonstrates feasibility of modal damping for the coupled vertical modes of the Type-A suspension. Deriving a conversion law between the Cartesian basis and the modal basis from the mathematical model, coupled signals of the vertical modes can be decomposed into those of each orthogonal eigenmode. Moreover, the result of the modal damping shows that the eigenmodes can be damped independently of other modes. Although the availability of modal controllers is validated only for the vertical modes in this test, one can expect to apply this technique to other stages having less-powerful actuators such as the cryogenic payload.

After the sequence of those tower test, the installed Type-A tower was integrated with the cryogenic payload and incorporated into a global system of the KAGRA interferometer. This thesis includes the measurement of the vibration isolation ratio from the ground to the test mass. During the first cryogenic test operation of the simplified 3-km Michelson interferometer, we measured the vibration transmissivity from the top stage to the error signals of the inteferometer output. Combining the measured result with a model prediction of the transmissibity from the ground to the top stage derived from the tuned mathematical model, the total vibration isolation ratio of the Type-A suspension is estimated as 9×10^{-22} for the pure longitudinal contribution at 10 Hz. Although the estimated result is pursued by some amount of mismatch with respect to the nominal model prediction, the seismic attenuation performance of the real system seems to be a reasonable level to achieve the design sensitivity of KAGRA.

Contents

Chapter 1

Introduction

1.1   Nature of gravitational waves

1.1.1   Derivation in linearized general relativity

The concept of gravitational wave appears firstly in the Einstein's letter as an wave solution of the linearized equation of the gravitational field. In other words, gravitational waves are the variation of spacetime which structure is determined as a metric tensor $g_{\mu\nu}$. The structure of spacetime is expressed as the world interval $\mathrm{d}s$ between two neighboring points via the following equation,

$$\mathrm{d}s^2 = g_{\mu\nu}\,\mathrm{d}x^\mu \mathrm{d}x^\nu\,. \tag{1.1}$$

The symbols with Greek index $\mathrm{d}x^\mu$ ($\mu = 0,\ 1,\ 2,\ 3$) denotes the difference of two separated points in the 4-dimensional coordinate $(x^0,\ x^1,\ x^2,\ x^3) \equiv (ct,\ x,\ y,\ z)$ [1]. A flat spacetime without any gravity is called Minkowski spacetime which structure is described with the metric $\eta = \mathrm{diag}(-1,\ 1,\ 1,\ 1)$.

The existence of mass or energy forms curved structure in the spacetime. The Einstein equation associates the curved spacetime with the distribution of the mass and energy,

$$R_{\mu\nu} - \frac{1}{2}g_{\mu\nu}R = \frac{8\pi G}{c^4}T_{\mu\nu}\,. \tag{1.2}$$

Here, $R_{\mu\nu}$ and R on the left hand side is respectively the Ricci tensor and the Ricci scalar which are associated to the curvature of spacetime through the Riemann tensor $R^\lambda_{\mu\rho\nu}$ as

---

[1] On the other hand, the symbols with Roman indices such as $\mathrm{d}x^i$ denotes the difference of two points only in the spacial components, $i = 1,\ 2,\ 3$.

follows[2].

$$R^\lambda_{\mu\rho\nu} = \partial_\rho\Gamma^\lambda_{\mu\nu} - \partial_\nu\Gamma^\lambda_{\mu\rho} + \Gamma^\lambda_{\alpha\rho}\Gamma^\alpha_{\mu\nu} - \Gamma^\lambda_{\alpha\nu}\Gamma^\alpha_{\mu\rho} \tag{1.3}$$

$$R_{\mu\nu} \equiv R^\alpha_{\mu\alpha\nu} \tag{1.4}$$

$$R \equiv R_{\mu\mu} \tag{1.5}$$

In the right hand side of eq. (1.2), $T_{\mu\nu}$ is the energy-momentum tensor, G is the Newton's gravitational constant and c is the speed of light. Thence the Einstein equation gives the interpretation that the mass-energy distribution on the right hand side creates the curvature of spacetime described on the left hand side in 1.2.

The derivation of the gravitational wave is achieved in the weak-field approximation where tiny perturbation exists in the flat spacetime. In terms of the metric it can be expressed as the sum the linear perturbation $h_{\mu\nu}$ and the Minkowski metric,

$$g_{\mu\nu} = \eta_{\mu\nu} + h_{\mu\nu} \,. \tag{1.6}$$

Imposing conditions of vacuum, $T_{\mu\nu} = 0$, and the Lorentz gauge,

$$\frac{\partial h^\mu_\nu}{\partial x_\mu} = 0 \,, \tag{1.7}$$

and disregarding the higher order terms $\mathcal{O}(h^2_{\mu\nu})$, substitution of eq. (1.6) to the Einstein equation eq. (1.2) yields a wave equation,

$$\left(-\frac{1}{c^2}\frac{\partial^2}{\partial t^2} + \frac{\partial^2}{\partial x_i^2}\right) h_{\mu\nu} = 0 \,. \tag{1.8}$$

This equation indicates that the perturbation $h_{\mu\nu}$ propagates through the spacetime in the speed of light as a wave.

When we choose a spatial coordinate such that a gravitational wave travels along the z- or x^3-direciton, the plain wave solution can be derived as the following expression.

$$h_{\mu\nu} = A_{\mu\nu} \exp\left[i\omega\left(t - \frac{z}{c}\right)\right]$$
$$A_{\mu\nu} = \begin{pmatrix} 0 & 0 & 0 & 0 \\ 0 & h_+ & h_\times & 0 \\ 0 & h_\times & -h_+ & 0 \\ 0 & 0 & 0 & 0 \end{pmatrix} \tag{1.9}$$

Here ω is the angular frequency, h_+ and $h_\times$ are the independent constants denoting amplitude of the gravitational wave. This reveals the transverse and polarized natures of gravitational waves. The two polarization is known as the plus mode and the cross mode which are symmetric through 45-degree rotation, as shown in fig. 1.1.

---

[2] Following the Einstein's summation convention, we shall take the summation of all the degrees of freedom about the Greek indices which appear both in superscripts and subscripts.
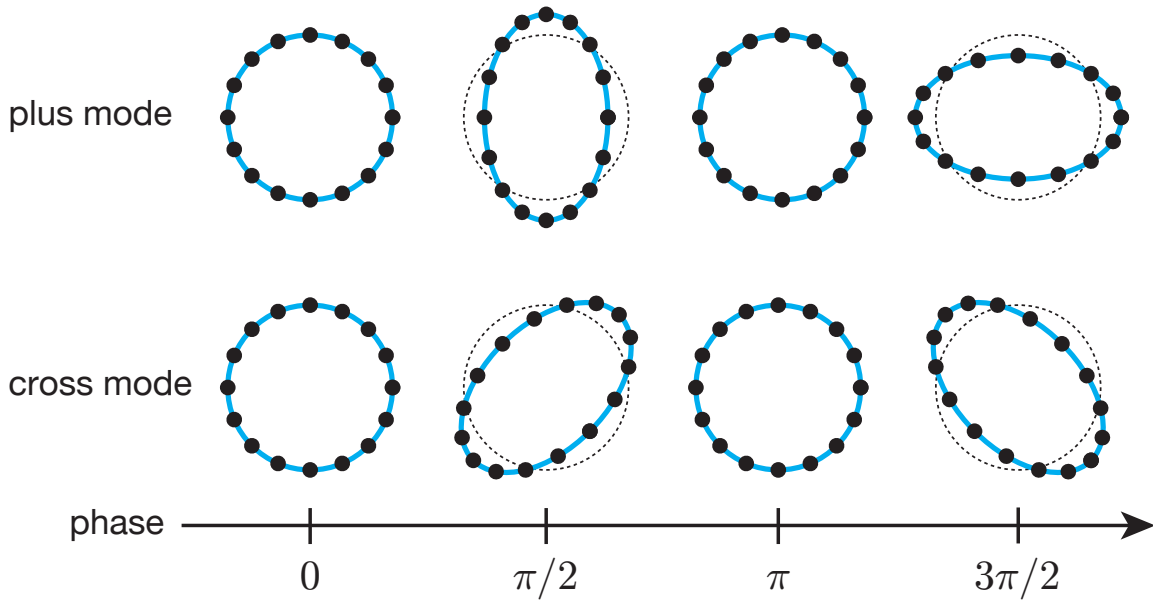
Fig. 1.1. Two polarizations of gravitational waves; +-mode and ×-mode. Each mode produces different shape of deformation in the free-falling point masses with circular configuration.

1.1.2 Observable effect of gravitational waves

Consider the situation that two free-falling point masses are positioned separately along the x- or x^1-axis with distance of ϵ. The effect of gravitational waves passing along the z-axis (described in eq. (1.9)) appears when wrinting the proper distance of the particles. Support that the particles are initially at rest, the proper distance δl is written as,

$$\delta l \equiv \int |\mathrm{d}s^2|^{1/2} = \int |g_{\mu\nu}\mathrm{d}x^\mu r dx^\nu|^{1/2}$$
$$= \int_0^\epsilon |g_{11}|^{1/2}\,\mathrm{d}x^1$$
$$\simeq |g_{11}|^{1/2} \simeq \left(1 + \frac{1}{2}h_{11}\right)\epsilon. \tag{1.10}$$

From eq. (1.10), it turns out that gravitational waves change the proper distance of the free-falling masses. This is the physical quantity observable for our laser interferometric telescopes. The absolute change of distance is proportional to both the initial separation ϵ and the amplitude h_{11}.

There are two polarizations in gravitational waves as shown in eq. (1.9). To understand interaction of those two modes with masses, consider a thought experiment in which the test masses are placed in circular configuration at $x^i = (\epsilon\cos\theta, \epsilon\sin\theta, 0)$. The proper distance of

the masses under the influence of gravitational waves is described as,

$$\begin{pmatrix} \delta l^x \\ \delta l^y \end{pmatrix} = \begin{pmatrix} \epsilon^x \\ \epsilon^y \end{pmatrix} + \frac{1}{2}\mathrm{e}^{i\omega(t-z/c)}\begin{pmatrix} h_+ & h_\times \\ h_\times & -h_+ \end{pmatrix}\begin{pmatrix} \epsilon^x \\ \epsilon^y \end{pmatrix} \tag{1.11}$$

$$= \begin{pmatrix} \epsilon^x \\ \epsilon^y \end{pmatrix} + \frac{1}{2}\mathrm{e}^{i\omega(t-z/c)}\begin{pmatrix} \epsilon^x \\ -\epsilon^y \end{pmatrix}h_+ + \frac{1}{2}\mathrm{e}^{i\omega(t-z/c)}\begin{pmatrix} \epsilon^x \\ \epsilon^y \end{pmatrix}h_\times . \tag{1.12}$$

The second term indicates the variation of the proper distance caused by the plus mode, while the third term indicates that by the cross mode. Figure 1.1 illustrates the interaction of two modes of gravitational waves with the free-falling masses. The plus mode distorts the circular arrangement into a "plus" shape, while the cross mode distorts into a "cross" shape. As mentioned above, the plus mode and the cross mode has symmetry through 45-degree rotation.

1.1.3   Gravitational wave radiation

A gravitaitonal wave is generated by accelerated masses analogous to the radiation of electro-magnetic wave which are induced by acceleration of charged particles. However a big difference is that the gravitational wave radiation requires quadrupole (or higher-order multipole) moment rather than a dipole moment which is the leading term for the electromagnetic radiation.

Starting from the wave equation eq. (1.8) in presense of the energy-momentum tensor on the right-hand side,

$$\left(-\frac{1}{c^2}\frac{\partial^2}{\partial t^2} + \frac{\partial^2}{\partial x_i^2} \right)h_{\mu\nu} = -\frac{16\pi G}{c^4}T_{\mu\nu} . \tag{1.13}$$

Introducing the retarded Green's function $G(\boldsymbol{x} - \boldsymbol{x}')$ written as,

$$G(\boldsymbol{x} - \boldsymbol{x}') = \frac{1}{4\pi|\boldsymbol{x} - \boldsymbol{x}'|}\delta(x_{\mathrm{ret}}^0 - x'^0) , \tag{1.14}$$

$$x_{\mathrm{ret}}^0 \equiv ct_{\mathrm{ret}} , \quad t_{\mathrm{ret}} = t - \frac{|\boldsymbol{x} - \boldsymbol{x}'|}{c} ,$$

just as in electromagnetism, one can obtain a solution of eq. (1.13) in the form of the retarded potential,

$$h_{\mu\nu}(x^0, \boldsymbol{x}) = \frac{4G}{c^4}\int \frac{T_{\mu\nu}\left(x^0 - \frac{|\boldsymbol{x}-\boldsymbol{x}'|}{c}, \boldsymbol{x}' \right)}{|\boldsymbol{x} - \boldsymbol{x}'|}\mathrm{d}\boldsymbol{x}' . \tag{1.15}$$

Support that the region of $T_{\mu\nu} \neq 0$ is small enough and the observer is far from the source, eq. (1.15) can be approximated to the lowest-order terms of the mass multipole expansion as,

$$h_{ij}(t, \boldsymbol{x}) = \frac{1}{r}\frac{2G}{c^4}\ddot{Q}_{ij}(t') , \tag{1.16}$$

where $r \equiv |\boldsymbol{x} - \boldsymbol{x}'|$, $t' \equiv t - r/c$ and Q_{ij} is the mass quadropole moment determined as,

$$Q_{ij}(t') = \int \rho(t', \boldsymbol{x}') \left(x_i' x_j' - \frac{1}{3}\delta_{ij} x^{i'} x^{j'} \right) \mathrm{d}\boldsymbol{x}' . \tag{1.17}$$

In eq. (1.16), the mass quadrupole moment appears as the leading term of the multipole expansion instead of monopole or dipole. It can be intuitively understood that the mass (= monopole) and the kinetic momentum (= dipole) are conservative quantities in an isolated system and thus provide no controbution to radiation process.

Radiated energy

Here the energy of gravitational wave radiation is briefly discussed. Using eq. (1.16), one can derive the total radiated energy all over the solid angle per unit time, or *gravitational luminosity* $\mathcal{L}$, as following expression.

$$\mathcal{L}_{\mathrm{gw}} = \frac{G}{5c^5} \left\langle \dddot{Q}_{ij} \dddot{Q}_{ij} \right\rangle . \tag{1.18}$$

Here the angle bracket $\langle ... \rangle$ indicates spatial average over many wavelength of emitted gravitational waves. This equation is equivalent to the Larmor's fomula in elecrtomagnetic radiation.

To estimate the magnitude of energy radiated as gravitational waves, we scale the $\dddot{Q}_{ij}$ with combination of physical parameters with basic units as

$$\dddot{Q}_{ij} \sim MR^2 T^{-3} \sim Mv^3 R^{-1} , \tag{1.19}$$

where M, R, T and v are the typical mass, spatial size, time scale and velocity of the source, respectively. Firstly, we consider to generate gravitational waves in laboratory-scale experiment that a dumbbell-like system, consists of two iron balls weighing 100 kg each connected with a 2-meter bar, is rotating in frequency of 100 Hz. Plugging eq. (1.19) to eq. (1.18), one can obtain

$$\begin{aligned} \mathcal{L}_{\mathrm{gw}} &\sim \frac{G}{5c^5} \frac{M^2 v^6}{R^2} \\ &\sim 2.4 \times 10^{-23} \left(\frac{M}{100\,\mathrm{kg}} \right)^2 \left(\frac{v}{4\pi\,\mathrm{m} \times 100\,\mathrm{Hz}} \right)^6 \left(\frac{R}{15\,\mathrm{cm}} \right) \, [\mathrm{erg/s}] . \end{aligned} \tag{1.20}$$

This energy emission rate is extremely small such that it takes about a thousand years to generate energy as equivalent to one photon of the cosmic microwave background. Therefore, it is desperate to construct an available source of gratitational waves on Earth and people pin their hope on the celestial sources.

For an astrophysical source usually bounded by its self gravity, we can assume that the kinetic energy and the potential energy of the system are comparable, so that

$$Mv^2 \sim \frac{GM^2}{R} . \tag{1.21}$$

Using this relation, the gravitational luminosity eq. (1.18) becomes

$$\mathcal{L}_{\mathrm{gw}} \sim 2.3 \times 10^{57} \left(\frac{R}{R_{\mathrm{sch}}} \right)^{-5} \, [\mathrm{erg/s}] \,. \tag{1.22}$$

Here the spatial size is scaled with the Schwarzschild radius defined by $R_{\mathrm{sch}} \equiv 2GM/c^2$. This estimation indicates that the size of the object is the key property for gravitational wave radiation.

Amplitude

To discuss the amplitude of the radiated gravitational waves, here the Newtonian source approximation is applied to eq. (1.16) such that

$$\begin{aligned} h &\sim \frac{1}{r} \frac{2G}{c^4} \frac{\partial^2}{\partial t^2} (MR^2) \sim \frac{1}{r} \frac{2GMv^2}{c^4} \\ &\sim \frac{R_{\mathrm{sch}}}{r} \left(\frac{v}{c} \right)^2 \,. \end{aligned} \tag{1.23}$$

one can parametrize the emission efficiency of gravitational waves with ϵ written as

$$\epsilon \sim \left(\frac{R_{\mathrm{sch}}}{R} \right) \,. \tag{1.24}$$

Thus rewritting eq. (1.23) with the parameter ϵ, an estimation of the gravitational-wave amplitude comes out.

$$h \sim \epsilon^{2/7} \frac{R_{\mathrm{sch}}}{2r} \tag{1.25}$$

$$\sim 1.5 \times 10^{-21} \left(\frac{\epsilon}{0.1} \right)^{2/7} \left(\frac{M}{M_\odot} \right) \left(\frac{r}{17 \, \mathrm{Mpc}} \right) \,. \tag{1.26}$$

Here the mass M and distance r is scaled by the solar mass $M_\odot = 1.989 \times 10^{30}$ [kg] and that from the Earth to the Virgo cluster of about 17 Mpc. Even if an optimistic radiation efficiency of $\epsilon = 10\,\%$ is assumed, the amplitude of gravitational waves from a system as heavy as the Sun is extremely small. For instance, when such a gravitational wave changes the proper distance between two free-falling masses separated apart by 3 km, the geometrical displacement is about 4.5×10^{-18} m.

1.2   Detected gravitational-wave sources

Since the Advanced LIGO detected the first gravitational wave (GW) event [4, 1], the number of the detected gravitational wave increases even in a few years' observation. Now the sources of all the detected events are the coalescence of compact star binaries such as

black holes and neutron stars [2, 3]. Recently the LIGO Scientific Collaboration and Virgo Collaboration opened a catalog of confident and merginal events of the gravitational wave detection [10]. It implies that the accumulation of the detected GW events expands our scope of the universe to its unrevealed fields. Here the astrophysical picture of the compact binary coalescence is presented.

1.2.1 Compact binary coalescence

Compact binary coalescences have been regarded as the most promising GW source for a long time and thus actually become the first GW event directly detected by human beings. A binary system of formed by compact stars such as neutron stars, black holes or white dwarfs, loses its orbital energy by gravitational radiation as the two stars approach to each other. The first evidence of this orbital energy loss is discovered by Hulse and Taylor in their long-period radio observation of the pulsar binary PSR B1913+16. The orbital decay of the pulsar binary shows precise agreeement with the energy loss which gravitational waves carry away from the system. In consequence of the fact that radiated energy grows as the two stars get closer to their center of gravity, the brightest gravitaional wave emission is expected at the moment of collision of two stars.

The typical compact binary coalescence scinario has three stages. The first stage is called *inspiral*, where the two stars revolve in quasi-stable circular or elliptic orbit with approaching to each other. Experiencing the last hundreds of revolution, the two stars fall into the region where the point mass approximation is no longer valid and then move to the second stage called *merger*. During the merger the two objects are mixed to form a single compact object. Then the last stage is *ringdown* where the newborn single object settles to a stationary state through the gravitational wave emission. The transitions through the whole process take places over a period of subseconds to minutes depending on the total mass of the system, although the lifetime of the binary before merging can be in the order of tens of millions of years.

Inspiral phase

A waveform of GWs in the inspiral phase, known as the *chirp* signal, is well predictable and hence the fact is extatcly the reason why the compact binary merger become the first event of the direct GW detection. Supporting a binary system with circular orbit (= sufficienlty small eccentricity), for such a two-body problem, it is convenient to use the relative coordinate $\boldsymbol{x}_0$ and the center-of-mass coordinate $\boldsymbol{x}_{\mathrm{CM}}$ which are determined as

$$\boldsymbol{x}_0 = \boldsymbol{x}_1 - \boldsymbol{x}_2\,, \tag{1.27}$$

$$\boldsymbol{x}_{\mathrm{CM}} = \frac{m_1\boldsymbol{x}_1 + m_2\boldsymbol{x}_2}{m_1 + m_2}\,, \tag{1.28}$$

where (m_1, m_2) and $(\boldsymbol{x}_1, \boldsymbol{x}_2)$ are the mass and the position of the corresponding star labeled as the subscription, respectively. We also denote the total mass by $m = m_1 + m_2$ and the reduced mass by $\mu = m_1 m_2 / m$. If we choose the frame such that $\boldsymbol{x}_{\mathrm{CM}} = 0$, what remains of interest is the single effective particle of mass μ and its coordinate $\boldsymbol{x}_0$. This procedure helps us to simplify the mass quadrupole moment in eq. (1.17), since $\rho(t, \boldsymbol{x}) = \mu \delta^3(\boldsymbol{x} - \boldsymbol{x}_0)$, into the following expression.

$$Q_{ij}(t) = \mu \left((x_0)_i (x_0)_j - \frac{1}{3} r_0^2 \, \delta_{ij} \right) . \tag{1.29}$$

For the moment we restrict the trajectory of the binary system in the xy-plane which is given by

$$
\begin{aligned}
x_0(t) &= r_0 \cos(\omega_{\mathrm{s}} t + \pi/2) \, , \\
y_0(t) &= r_0 \sin(\omega_{\mathrm{s}} t + \pi/2) \, , \\
z_0(t) &= 0 \, .
\end{aligned}
\tag{1.30}
$$

Here the initial phase $\pi/2$ is chosen just for covenience sake. Then substituting eq. (1.30) to eq. (1.29) and taking second derivative with respect to time, we can obtain

$$\ddot{Q}_{11} = 2\mu \, r_0^2 \, \omega_{\mathrm{s}}^2 \, \cos 2\omega_{\mathrm{s}} t \, , \tag{1.31}$$

$$\ddot{Q}_{12} = 2\mu \, r_0^2 \, \omega_{\mathrm{s}}^2 \, \sin 2\omega_{\mathrm{s}} t \, , \tag{1.32}$$

and $\ddot{Q}_{22} = -\ddot{Q}_{11}$. Recalling the equation of mass quadrupole radiation eq. (1.16) given by

$$h_+ = \frac{1}{r} \frac{G}{c^4} (\ddot{Q}_{11} - \ddot{Q}_{22}) \, , \tag{1.33}$$

$$h_\times = \frac{2}{r} \frac{G}{c^4} \ddot{Q}_{12} \, , \tag{1.34}$$

hence the amplitude of the two polarizations of GW is described with the source parameters of μ, r_0 and ω, as

$$h_+(t) = \frac{1}{r} \frac{4G\mu \, \omega_{\mathrm{s}}^2 \, r_0^2}{c^4} \cos 2\omega_{\mathrm{s}} t_{\mathrm{ret}} \, , \tag{1.35}$$

$$h_\times(t) = \frac{1}{r} \frac{4G\mu \, \omega_{\mathrm{s}}^2 \, r_0^2}{c^4} \sin 2\omega_{\mathrm{s}} t_{\mathrm{ret}} \, . \tag{1.36}$$

Now we release the trajectry of the binary system from the xy-plane to an orbit facing onto arbitrary direction. In such a situation we assumed that the observer is sufficiently far from the source, the observation of inclined plain waves can be regarded as that of axis-aligned plain waves with inclined line of sight as illustrated in fig. 1.2. From the observational point of view, we can access the information of the inclination of the source ι as the fainted amplitude which can be written as

$$h_+(t) = \frac{1}{r} \frac{4G\mu \, \omega_{\mathrm{s}}^2 \, r_0^2}{c^4} \left(\frac{1 + \cos^2 \iota}{2} \right) \cos 2\omega_{\mathrm{s}} t_{\mathrm{ret}} \, , \tag{1.37}$$

$$h_\times(t) = \frac{1}{r} \frac{4G\mu \, \omega_{\mathrm{s}}^2 \, r_0^2}{c^4} \cos \iota \, \sin 2\omega_{\mathrm{s}} t_{\mathrm{ret}} \, . \tag{1.38}$$
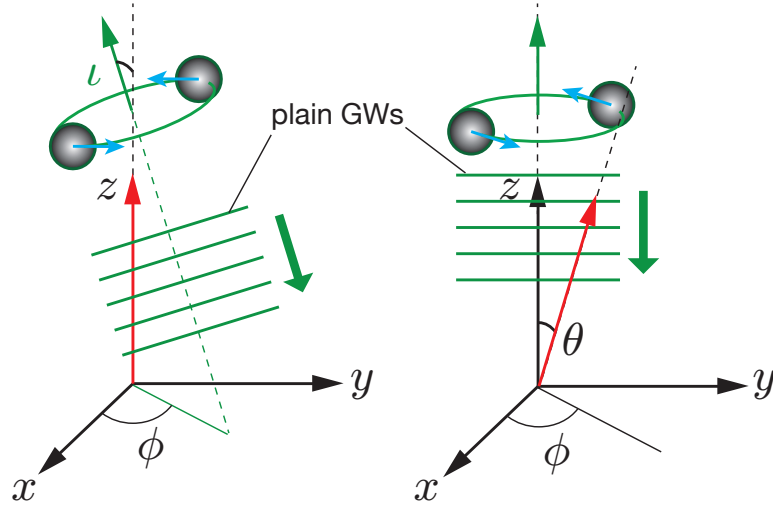
Fig. 1.2. Observation of plain GWs from the inclined binary system with line of sight aligned to the z-axis (*left*), and that from the face-on binary system with line of sight oriented to (θ, ϕ) direction (*right*).

To eliminate degeneracy of the source frequency $\omega_{\rm s}$ with the separation distance of the two stars r_0 as it gradually decreases holding the Kepler's harmonic law of $\omega_{\rm s}^2 = Gm/r_0^3$, we introduce the *charp mass* defined as

$$M_{\rm c} \equiv \mu^{3/5}\, m^{2/5} = \frac{(m_1 m_2)^{3/5}}{(m_1 + m_2)^{1/5}}\,. \tag{1.39}$$

Using this chirp mass, finally we obtain the expression of the chirp signal as

$$h_+(t) = \frac{4}{r}\left(\frac{GM_{\rm c}}{c^4}\right)^{5/3}\left(\frac{\pi f_{\rm gw}}{c}\right)^{2/3}\left(\frac{1+\cos^2 \iota}{2}\right)\cos(2\pi f_{\rm gw} t_{\rm ret})\,, \tag{1.40}$$

$$h_\times(t) = \frac{4}{r}\left(\frac{GM_{\rm c}}{c^4}\right)^{5/3}\left(\frac{\pi f_{\rm gw}}{c}\right)^{2/3}\cos \iota\,\sin(2\pi f_{\rm gw} t_{\rm ret})\,, \tag{1.41}$$

where $f_{\rm gw}$ is the frequency of the GWs associated with the source frequency such that $f_{\rm gw} = \omega_{\rm s}/\pi$. These expressions highlight the importance of the chirp mass $M_{\rm c}$ which summarizes the information of the source mass through the chirp signal.

The primary feature of the chirp signal is that its frequency $f_{\rm gw}$ grows up as the binary system evolves to coalescence, since the separation of the two stars must decrease compensating the energy loss to GWs. Recalling the Kepler's harmonic law, the orbital energy of the binary system can be written as

$$E_{\rm orbit} = -\frac{Gm_1 m_2}{2r_0^2} = -\left(\frac{G^2 M_{\rm c}^5 \omega_{\rm gw}}{32}\right)^{1/3}\,. \tag{1.42}$$

On the other hand, the luminosity of GW radiation can be obtained by substituting eq. (1.31) and eq. (1.32) to eq. (1.18).

$$\mathcal{L}_{\text{gw}} = \frac{32}{5}\frac{c^5}{G}\left(\frac{GM_{\text{c}}\omega_{\text{gw}}}{2c^3}\right)^{10/3} \tag{1.43}$$

Equating eq. (1.43) to $-\mathrm{d}E_{\text{orbit}}/\mathrm{d}t$ given in eq. (1.42), one can obtain

$$\dot{f}_{\text{gw}} = \frac{96}{5}\pi^{8/3}\left(\frac{GM_{\text{c}}}{c^3}\right)^{5/3}f_{\text{gw}}^{11/3} \tag{1.44}$$

The integration of this equation tells us that the frequency f_{gw} diverges at a finite value of time t_0. Here denotes the time to coalescence as $\tau \equiv t_0 - t$, the evolution of the chirp frequency follows the equation below.

$$f_{\text{gw}} = \left(\frac{5}{256}\right)^{3/8}\frac{1}{\pi}\left(\frac{GM_{\text{c}}}{c^3}\right)^{-5/8}\tau^{-3/8} \tag{1.45}$$

As shown in fig. 1.3, the frequency as well as the amplitude of the chirp signal sweeps up by the end of its inspiral phase. For instance, the chirp signal from a $1.4M_{\odot}$-$1.4M_{\odot}$ neutron star binary has frequency and amplitude of,

$$f_{\text{gw}} \approx 134 \text{ Hz} \left(\frac{M_{\text{c}}}{1.21\ M_{\odot}}\right)^{-5/8}\left(\frac{\tau}{1 \text{ sec}}\right)^{-3/8}, \tag{1.46}$$

$$h \approx 2.5 \times 10^{-22}\left(\frac{M_{\text{c}}}{1.21\ M_{\odot}}\right)^{5/3}\left(\frac{\tau}{1 \text{ sec}}\right)^{-1/4}\left(\frac{r}{17 \text{ Mpc}}\right)^{-1}, \tag{1.47}$$

The GW radiation in the chirp waveform finishes when the radial distance of the binary decreases beyond the innermost stable circular orbit (ISCO), where stable circular orbits are no longer allowed. In Schwarzschild stacetime, the orbital radius corresponding to ISCO is located at r_{ISCO}, which given by

$$r_{\text{ISCO}} = \frac{6Gm}{c^2} = 3R_{\text{sch}}. \tag{1.48}$$

Therefore the increase of the source frequency reaches its peak when $r_0 \simeq r_{\text{ISCO}}$. Using the Kepler's law again, the source frequency at the ISCO is calculated as

$$f_{\text{ISCO}} = \frac{1}{2\pi}\frac{1}{6\sqrt{6}}\frac{c^3}{Gm}$$
$$\simeq 2.2 \text{ kHz}\left(\frac{M_{\odot}}{m}\right). \tag{1.49}$$

Seeing eq. (1.49), f_{ISCO} turns out to depend on the source mass. For instance, a $1.4M_{\odot}$-$1.4M_{\odot}$ neutron star binary has $f_{\text{ISCO}} \sim 800$ Hz and a $30M_{\odot}$-$30M_{\odot}$ black hole binary has $f_{\text{ISCO}} \sim 36$ Hz. Note that its GW frequency is twice larger than the source frequency.
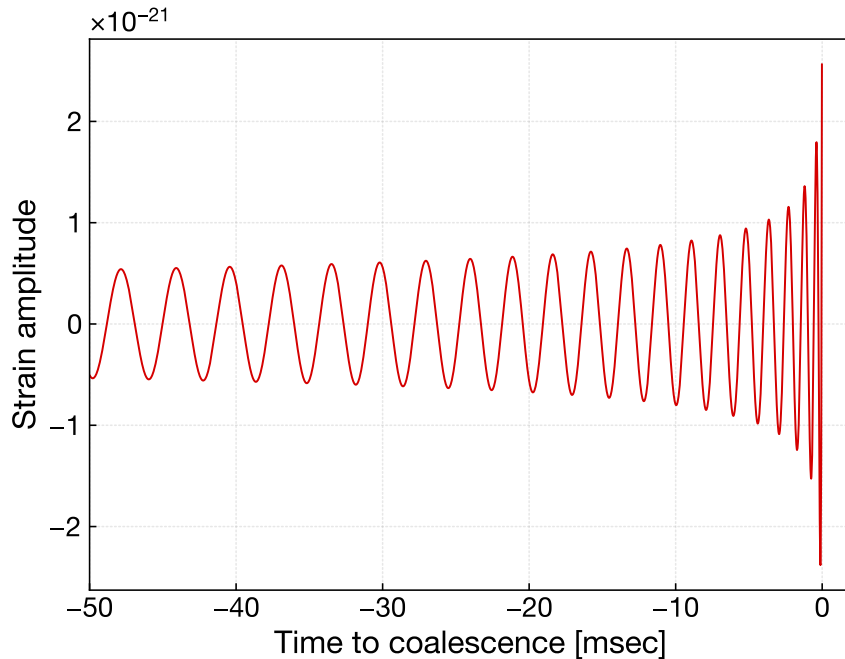
Fig. 1.3. A calculated chirp signal from a $1.4M_\odot$-$1.4M_\odot$ neutron star binary from 17 Mpc as distant as the Virgo cluster.

More precise prediction of the chirp waveform is a subject for the post-Newtonian expansion, which treats the background spacetime curvature with the velocity of the source as they are correlated to each other. In the framework of the post-Newtonian expansion, even though it still assumes low velocity and weak field, slightly-deviated chirp signal can be reproduced with $\mathcal{O}(v/c)$, the higher-order perturbations of relativistic terms. Thus the source parameters such as individual mass and spin of the binary can be extracted through the coefficients of the post-Newtonian terms. Moreover, precise estimation of the post-Newtonian terms enables to distinguish the modified theories of gravity as a successer of the general relativity.

To hunt these signals among the detecter noise, data analysts use *matched filter* algorithm that compares the detector output to the library of the waveform templates which scan the parameter space of binary coalescences.

Merger and ringdown phase

Whereas the waveform of GWs in the inspiral phase is predictable in sufficient precision, in the merger phase the dynamics of the binary system can be no longer approximated to point-mass-like or low-velocity ones. Therefore, numerical simulations, a field called *numerical relativity*, is one of the few powerful tools to demonstrate the coalescense including the effects of fluid dynamics, relativistic motions and evolution of background curvature.

The waveform in the ringdown phase is dominated by a characteristic oscillation called
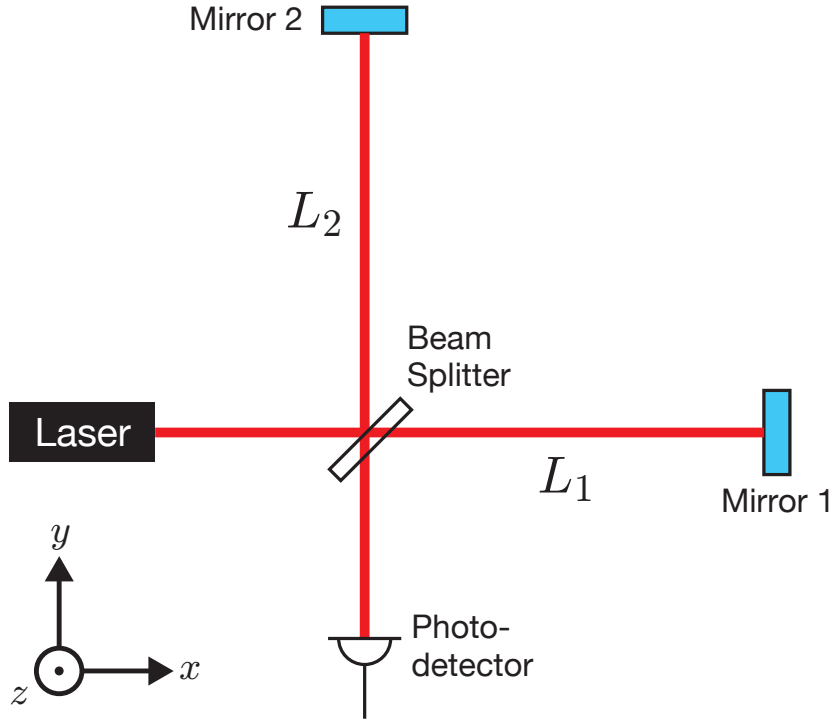
Fig. 1.4. Michelson interferometer

quasinormal mode (QNM) assuming the remnant object is a black hole. Since the black hole just after the coalescense has perturbed spacetime, it will decay to the stationary state through damped pulsation associated with gravitational wave radiation. It indicates that the gravitational waves from the quasinormal mode includes the information of the spacetime structure beyond the event horizon. Thus the gravitational waves can be used as a probe for properties of the black hole. Not only black holes but also neutron stars have their quasinormal modes for which gravitational waves can provide information about their equation of state to exclude inconsistent theoretical models.

1.3 Gravitational wave detection with laser interferometer

The electromagnetic field of the laser is written as,

$$E_{\text{in}} = E_0\, e^{i\Omega t}\,. \tag{1.50}$$

This laser beam is divided into two paths respectively in x-direction and y-direction at the beam splitter (BS). Both beams are reflected at the end mirrors and then recombined at

the BS again. Assuming that the phase shift in each arm as ϕ_1 and ϕ_2, one can write the electromagnetic field of the recombined beam as,

$$E = E_1 \, e^{i(\Omega t - \phi_1)} - E_2 \, e^{i(\Omega t - \phi_2)} \,. \tag{1.51}$$

Here E_1 and E_2 denote the amplitude of the field comes from each arm respectively. In the ideal case with completely symmetric mirrors, we have $E_1 = E_2 = E_0/2$. But in realistic case such that the reflectivity of the end mirrors differ from each other, the two beams are no longer symmetric and their amplitude holds $E_1 \neq E_2$. We can see the power of the incident light to the photodetector (PD) as,

$$P = |E|^2 = E_1^2 + E_2^2 + 2E_1 E_2 \cos(\phi_1 - \phi_2) \tag{1.52}$$

The power has a cosinusoidal from with respect to the phase difference $\phi_1 - \phi_2$. Therefore, one can regards the Michelson interferomter as an instrument to detect the phase shift between two beams with different paths.

Response of Michelson interferometer to GWs

Now consider +-mode gravitational waves coming to the Michelson intererometer in the z-direction. The world interval can be written as,

$$\mathrm{d}s^2 = -c^2 \mathrm{d}t^2 + (1+h)\mathrm{d}x^2 + (1-h)\mathrm{d}y^2 + \mathrm{d}z^2 \,. \tag{1.53}$$

Since the laser beam travels along the null vector which satisfy $\mathrm{d}s^2 = 0$, The beam along the x-axis is expressed as

$$\frac{\mathrm{d}x}{\mathrm{d}t} = \pm \frac{c}{\sqrt{1+h}} \simeq \pm \left(1 - \frac{1}{2}h\right) c \,. \tag{1.54}$$

Here we determined positive sign indicates the light going toward $+x$-direction. Integrating the $\mathrm{d}x$ along a round trip path between the BS and the x-end mirror such as,

$$\int \mathrm{d}x = 2L_1 = c \int_{t-\Delta t_1}^{t} \left(1 - \frac{1}{2}h(t')\right) \mathrm{d}t' \,, \tag{1.55}$$

the round trip time of the beam is

$$\Delta t_1 = \frac{2L_1}{c} + \frac{1}{2} \int_{t-2L_1/c}^{t} h(t')\mathrm{d}t' \,. \tag{1.56}$$

Consequently we can get the phase shift by the gravitational waves in the x-arm light.

$$\phi_1 = \Omega \, \Delta t_1 = \frac{2L_1\Omega}{c} + \frac{\Omega}{2} \int_{t-2L_1/c}^{t} h(t')\mathrm{d}t' \tag{1.57}$$

Applying the same approach, the phase shift in the y-ram is

$$\phi_2 = \Omega\,\Delta t_2 = \frac{2L_1\Omega}{c} - \frac{\Omega}{2}\int_{t-2L_2/c}^{t} h(t')\mathrm{d}t'\,. \tag{1.58}$$

Therefore the phase difference between the two beams $\phi_1 - \phi_2$ we get

$$\phi_1 - \phi_2 = \frac{2L_-\Omega}{c} + \delta\phi_{\mathrm{GW}} \tag{1.59}$$

$$\delta\phi_{\mathrm{GW}} = \Omega\int_{t-2L/c}^{t} h(t')\mathrm{d}t' \tag{1.60}$$

where assumed $L_1 \simeq L_2 \simeq L$、 $L_- \equiv L_1 - L_2$. Eq. (1.59) shows the change of the phase difference induced by the gravitational waves.

Frequency renponse of Michelson interferometer to GWs

Fourier transformation of the $h(t)$ is written as follows.

$$h(t) = \int_{-\infty}^{\infty} h(\omega)e^{i\omega t}\mathrm{d}\omega \tag{1.61}$$

Using (1.61) we can rewrite the equation of phase shift by GWs (**??**) as,

$$\delta\phi_{\mathrm{GW}} = \Omega\int_{t-2L/c}^{t}\int_{-\infty}^{\infty} h(\omega)e^{i\omega t'}\mathrm{d}\omega\mathrm{d}t'$$

$$= \int_{-\infty}^{\infty}\frac{2\Omega}{\omega}\sin\left(\frac{L\omega}{c}\right)e^{-iL\omega/c}h(\omega)e^{i\omega t}\mathrm{d}\omega$$

$$= \int_{-\infty}^{\infty} H_{\mathrm{MI}}(\omega)\,h(\omega)e^{i\omega t}\mathrm{d}\omega \tag{1.62}$$

$$H_{\mathrm{MI}}(\omega) = \frac{2\Omega}{\omega}\sin\left(\frac{L\omega}{c}\right)e^{-iL\omega/c}\,, \tag{1.63}$$

The $H_{\mathrm{MI}}(\omega)$ in this equation represents the frequency response of the Michelson interferometer to GWs.

The magnitude of the response $|H_{\mathrm{MI}}(\omega)|$ is maximized when the following condition is satisfied.

$$\frac{L\omega}{c} = \frac{\pi}{2} \tag{1.64}$$

From another point of view, we can decide an arm length L of the interferometer which maximizes its sensitivity to a given frequency of GWs. For instance, optimizing the response to GWs at 1 kHz, the arm length should be chosen as $L = 75$ km and increasing the arm length beyond the optimum will deteriorate the sensitivity.

On the other hand, constructing the laser interfometer with such a large baseline length is impractical for geographical or technical reasons. A circumvent is use of Fabry-Perot

cavities in the Michelson interferometer. In this configuration called "Fabry-Perot Michelson interferometer", the effective arm length can be elongated than the physical separation of the mirrors.

1.3.1 Fabry-Perot interferometer

A Fabry-Perot interferometer (or cavity) is composed of two mirrors facing each other as shown in Fig.1.5. The light entered from the front mirror is reflected back and forth between the two mirrors repeatedly. A fraction of the light stored in the cavity is reflected back to the incident direction and a fraction is transmitted through the end mirror. Now writing electric
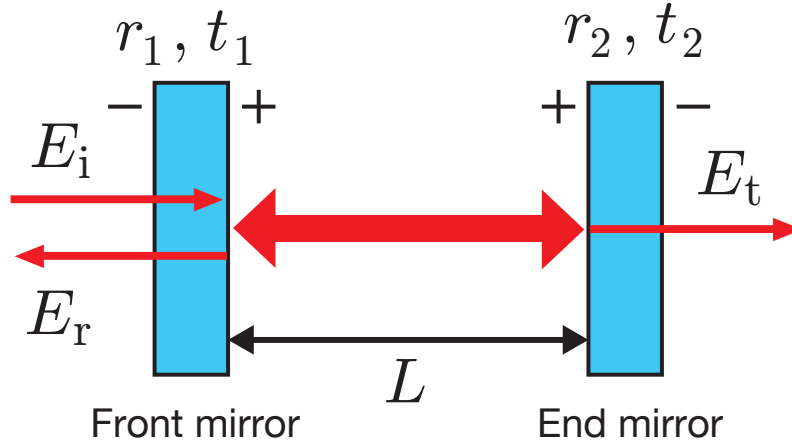
Fig. 1.5. Fabry-Perot interferometer

field of the input beam as E_i, the amplitude of the reflected light E_r is written as

$$E_r = E_i \left(r_1 - \frac{t_1^2 r_2 e^{-i\Phi}}{1 - r_1 r_2 e^{-i\Phi}} \right) . \tag{1.65}$$

Here, $\Phi = 2L\Omega/c$ is the phase shift through a round trip of the cavity, r_1 and r_2 are the amplitude reflectivities, t_1 and t_2 are the amplitude transmissivities. While the amplitude of the transmitted light E_t is written as

$$E_t = E_i \frac{t_1 t_2 e^{-i\Phi/2}}{1 - r_1 r_2 e^{-i\Phi}} . \tag{1.66}$$

With these expressions, we can get the amplitude reflectivity and amplitude transmissivity of the FP cavity, r_{cav} and t_{cav}, as

$$r_{\mathrm{cav}} = r_1 - \frac{t_1^2 r_2 e^{-i\Phi}}{1 - r_1 r_2 e^{-i\Phi}} , \qquad (1.67)$$

$$t_{\mathrm{cav}} = \frac{t_1 t_2 e^{-i\Phi/2}}{1 - r_1 r_2 e^{-i\Phi}} . \qquad (1.68)$$

The the power of the reflected and the transmitted light P_{r}, P_{t}, we get

$$P_{\mathrm{r}} = |E_{\mathrm{r}}|^2 = \frac{[(t_1^2 + r_1^2)r_2 - r_1]^2 + 4r_1 r_2 (r_1^2 + t_1^2) \sin^2(\Phi/2)}{(1 - r_1 r_2)^2 [1 + F \sin^2(\Phi/2)]} |E_{\mathrm{i}}|^2 , \qquad (1.69)$$

$$P_{\mathrm{t}} = |E_{\mathrm{t}}|^2 = \left(\frac{t_1 t_2}{1 - r_1 r_2}\right)^2 \frac{1}{1 + F \sin^2(\Phi/2)} |E_{\mathrm{i}}|^2 , \qquad (1.70)$$

where,

$$F \equiv \frac{4 r_1 r_2}{(1 - r_1 r_2)^2} . \qquad (1.71)$$

From the equation above, resonant condition can be determined as

$$\Phi = 2\pi n \qquad (n\text{: natural number}) , \qquad (1.72)$$

in which state the transmitted light and also the intracavity light have the maximum intensity. Rewriting the condition with the wavelength of the light,

$$2L = n\lambda \qquad (n\text{: natural number}) . \qquad (1.73)$$

Therefore in other words, the resonant condition is that the round trip distance of the FP cavity is whole-integer multiple of the wavelength.

Using Eq. (1.70), the transmittance with respect to the the laser frequency can be plotted as shown in Fig. 1.6. One can find that the transmittance has periodic peaks as the laser frequency shifts. The frequency range corresponding to the period is called *free spectral range (FSR)*, which is written as

$$\nu_{\mathrm{FSR}} = \frac{\omega_{\mathrm{FSR}}}{2\pi} = \frac{2L}{c} . \qquad (1.74)$$

Then with use of eq. (1.70), we can derive the full width at half maximum (FWHM) of the peak ν_{FWHM} from the following equation,

$$\frac{1}{1 + F \sin^2(\pi L \, \nu_{\mathrm{FWHM}}/c)} = \frac{1}{2} . \qquad (1.75)$$
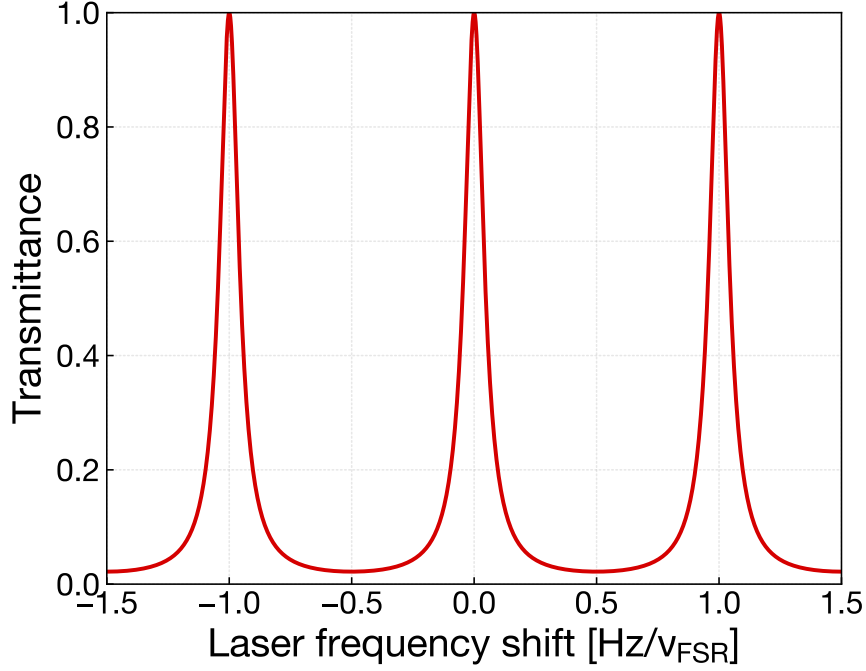
Fig. 1.6. Normalized transmittance of a Fabry-Perot interferometer with $r_1 = 0.75$, $r_2 = 0.99$ and $\mathcal{F} \simeq 10$

Under the approximation that $\pi L \nu_{\text{FWHM}}/c = \pi \nu_{\text{FWHM}}/2\nu_{\text{FSR}} \ll 1$ [3], one can perform Taylor expansion for the sine.

$$\nu_{\text{FWHM}} = \frac{c(1 - r_1 r_2)}{2\pi L \sqrt{r_1 r_2}} \tag{1.76}$$

Here the fraction of ν_{FWHM} and ν_{FSR} is called *finesse*, a value which represents the sharpness of the resonant peaks described as

$$\mathcal{F} \equiv \frac{\nu_{\text{FSR}}}{\nu_{\text{FWHM}}} = \frac{\pi \sqrt{r_1 r_2}}{1 - r_1 r_2}. \tag{1.77}$$

From eq. (1.77), it turns that the finesse is determined only through the reflectivity of the mirrors. With reflectivity closer to unity, the resonant peak becomes sharp.

Frequency response of Fabry-Perot interferometer to GWs

One can calculate the n times round trip time of the light in the FP cavity Δt_n in the same manner from eq. (1.53) to eq. (1.56).

$$\Delta t_n \simeq \frac{2L_1}{c}n + \frac{1}{2}\int_{t-2L_1 n/c}^{t} h(t')\mathrm{d}t' \tag{1.78}$$

---

[3] Because the FP interferometer has in general a finesse (described in later eq. (1.77)) much larger than unity, this approximation can be valid enough.

Through the Fourier transformation of **??**, Δt_n turns to

$$\Delta t_n \simeq \frac{2L_1}{c} n + \frac{1}{2} \int_{-\infty}^{\infty} h(\omega) \frac{1 - e^{-2iL\omega n/c}}{i\omega} e^{i\omega t} \mathrm{d}\omega \,. \tag{1.79}$$

Now recalling eq. (1.65), the reflected beam is

$$E_{\mathrm{r}} = E_{\mathrm{i}} \left(r_1 - t_1^2 r_2 \sum_{n=1}^{\infty} r_1^{n-1} r_2^{n-1} \right) e^{-i\Phi n} \,. \tag{1.80}$$

Substituting $\Phi n = \Omega \,\Delta t_n$ into the equation above and linealizing h under the assumption of $|h| \ll 1$, we can get

$$\frac{E_{\mathrm{r}}}{E_{\mathrm{i}}} \simeq r_1 - \frac{t_1^2 r_2 e^{-i\Phi}}{1 - r_1 r_2 e^{-i\Phi}} + \frac{t_1^2 r_2 e^{-i\Phi}}{1 - r_1 r_2 e^{-i\Phi}} \int_{-\infty}^{\infty} \frac{\Omega}{2\omega} h(\omega) \frac{1 - e^{iL\omega/c}}{1 - r_1 r_2 e^{-\Phi} e^{-iL\omega/c}} e^{i\omega t} \mathrm{d}\omega \,. \tag{1.81}$$

Assuming the resonance which satisfies $\phi = 2\pi n$, finally the following equation is obtained.

$$\frac{E_{\mathrm{r}}}{E_{\mathrm{i}}} \simeq \frac{r_1 - (r_1^2 + t_1^2) r_2}{1 - r_1 r_2} \left[1 - i \int_{-\infty}^{\infty} H_{\mathrm{FP}}(\omega) \, h(\omega) e^{i\omega t} \mathrm{d}\omega \right] \tag{1.82}$$

$$H_{\mathrm{FP}}(\omega) = \frac{\alpha_{\mathrm{c}} \Omega}{\omega} \frac{\sin(\omega L/c)}{1 - r_1 r_2 e^{-2i\omega L/c}} e^{-i\omega L/c} \tag{1.83}$$

$$\alpha_{\mathrm{c}} \equiv \frac{t_1^2 r_2}{r_1 - (r_1^2 + t_1^2) r_2} \tag{1.84}$$

The $H_{\mathrm{FP}}(\omega)$ indicates the frequency response of the FP interferometer to GWs.

For further understanding, taking magnitude of $H_{\mathrm{FP}}(\omega)$, we get

$$|H_{\mathrm{FP}}(\omega)| = \frac{\alpha_{\mathrm{c}} \Omega}{\omega(1 - r_1 r_2)} \frac{|\sin(\omega L/c)|}{\sqrt{1 + F \sin^2(\omega L/c)}} \,. \tag{1.85}$$

In the case of $\omega L/c \ll 1$,

$$|H_{\mathrm{FP}}(\omega)| \simeq \frac{\alpha_{\mathrm{c}} \Omega}{\omega(1 - r_1 r_2)} \frac{\omega L}{c\sqrt{1 + (\sqrt{F} L\omega/c)^2}}$$

$$= \frac{\alpha_{\mathrm{c}} \Omega}{\omega(1 - r_1 r_2)} \frac{1}{\sqrt{1 + (\tau\omega)^2}} \,, \tag{1.86}$$

$$\tau = \frac{\sqrt{F} L}{c} = \frac{2L}{\pi c} \mathcal{F} \,. \tag{1.87}$$

From this equation, we can find that the FP interferometer has 1st-order low pass response to GWs. The time constant τ determined by eq. (1.87) means the average of storage time of light inside the cavity. Hence the roll-off frequency of the low pass response is written as

$$\nu_{\mathrm{c}} = \frac{\omega_{\mathrm{c}}}{2\pi} = \frac{1}{2\pi\tau} \,. \tag{1.88}$$

1.3.2   Noise sources

Due to the tiny interaction of gravitational waves with matters, the GW detecters suffer from any noise sources. Here typical noise sources are briefly summarized.

Quantum noise

The interferometric GW detection has some fundamental noise sources which is often called quantum noise, caused by the use of laser power. The main sources of the quantum is shot noise and radiation pressure noise. Shot noise is a noise caused by the quantum fluctuation of number of photons in the laser beam. Radiation pressure noise is a noise induced by fluctuation of radiation pressure acting on the mirror surface. These quantum fluctuations are the conjugate quantities tied with the uncertainty principle, therefore having a trade-off in the contribution to the inteferometer sensitivity.

Thermal noise

The thermal vibration of the atoms with finite temperature causes fluctuations of the surface axial position and elastic shapes of the mirror, turning into the fluctuation of the optical path length of the interferometer. This noise is generally called *thermal noise.* Thermal noise can be categorized into two contributions; the one originates from the substrate or the coating layers of the mirror is called *mirror thermal noise*, while the one caused by the suspension wires is called *suspension thermal noise.*

The impact of thermal noise is related to the the mechanical loss of the materials via the fluctuation-dissipation theorem. To reduce the impact of the thermal noise, one should choose a material with high quality factor for the mirrors and the suspension components. Some of advanced gravitational wave detectors employ fused silica as the material of the mirror substrate and the suspension fibers due to its high mechanical Q-factor ($\sim 10^7$) at room temperature. Another way to mitigate thermal noise is to lower the temperature which is the strategy KAGRA took. Owing to dependence of the mechanical quality factor on temperature, fused silica no longer shows better performance in cryogenic situation. On the other hand, sapphire and silicon show high mechanical quality in cryogenic temperatures and thus become a candidate material for the mirror substrate.

Seismic noise

Seismic noise is an inevitable disturbance for the graviational wave detectors constructed on the Earth. Continuous and random motion of the ground always shake the mirror which results in unsertainty of the optical cavity length. This noise is the main target for the vibration isolation system to attenuate its impact on the gravitational wave detector. Hence more detailed description will be presented in the next chapter.

1.4   Targets and outline of this thesis

The goal of this research is to build vibration isolation systems for KAGRA and to achieve required performances for the design sensitivity of the interferometer. In particular, this research focuses on the 13.5-meter-tall vibration isolation system, a largest one for the main mirrors forming 3 km arm cavities. The main implementation of this study was held in the period of upgrade campaign of KAGRA where the primary components of optics, machanics, and electonics are installed and tested toward fully-configured operation. The vibration isolation system for the main mirrors was firstly assembled, installed, and tested in this study at the underground site since it's difficult to perform a prototype experiment due to its large dimension. Although the mechanical components had been individually tested, the performance of the whole assembly is determined by the installation and adjustments at the practical site. Moreover, the electric devices for the control of the vibration isolation system should be tuned according to the infrastructure of the digital system adopted in KAGRA. Therefore, the installation and performance test of the vibration isolation systems are the indispensable work to realize the gravitational wave observation of KAGRA with its design sensitivity.

The outline of this thesis is as follows. Chapter 2 describes the basics of the vibration isolation and suspension systems. Some mechanisms of low-frequency oscillator used in the KAGRA suspension systems are also presented. Chapter 3 explains the details of the vibration isolation system for the main mirrors, called Type-A suspension. In this chapter, overviewing the global system of the KAGRA interferometer at first, the conceptual design of the suspensions and required performances on them are mentioned. Then the detailed setup of the instuments such as mechanical components and electic devices are described. Chapter 4 discusses the control design of the vibration isolation systems. As explained in this chapter, the vibration isolation systems needs to have controllability of the suspended stages to allow the interferometer to secure stable operation. Since the dynamics of the vibration isolation systems can be represented with a mathematical model in good accuracy, it is helpful to predict the behavior of the nominal system in order to comapare with the measurement results. In addition, the feasibility and expected performance of the advanced technique of the damping control, called modal damping, is also discussed in this chapter. Chapter 5 is the main achievement of this study describing the experimental results of the performance test of the Type-A suspension. As mentioned later, the Type-A suspension can be divided into two sections, namely tower and payload. This study focuses on the former, representing top five stages, which has the key components important for the vibration isolation performance. This chapter presents the measured performance of the Type-A tower and discusses its agreement with the requirements. Finally in chapter 6 the results of the performance test are summarized and then the conclusion and further prospects of this research

are mentioned.

Chapter 2

Vibration isolation system

Vibration isolation is an essential technique for terrestrial gravitational wave telescopes. Mirrors in a laser interferometer on the Earth always suffer from seismic disturbances. The simple ideas to reduce the mirror's fluctuation caused by the ground motion are:

1. To place the mirrors at a quiet site.

2. To isolate the mirrors mechanically from the ground.

This chapter describes the basic concepts how to reduce the impact of seismic disturbance onto the interferometric gravitational wave observation. Section 2.1 mentions the nature of seismic background noise, the source of vibrations.

2.1 Seismic noise

The nature of seismic background noise is studied by J. Peterson. He made a catalog of seismic background noise spectra obtained from a world wide network of the seismograph stations. From the data, one model of the ground specta called *New High/Low Noise Model* (NHNM/NLNM) is established which provides the upper and lower bounds of the measured seismic motion. Figure 2.1 shows the power spectral density of the NHNM/NLNM together with the seismic specta measured at all over the world.

At low frequency below 1 mHz, the spectra of seismic motion grows rapidly due to tidal deformation of the Earth. Such low-frequency seismic motion doesn't disturb gravitational wave observation since the test masses of terrestrial detecters move commonly following to the ground.

There is a protrusion around 0.1–1 Hz in the spectrum which is known as *microseismic peak*. The microseism is caused by ocean waves beating land shores, hence it has a clear trend to be observed strongly at locations close to the coasts and weakly in the middle of continents.
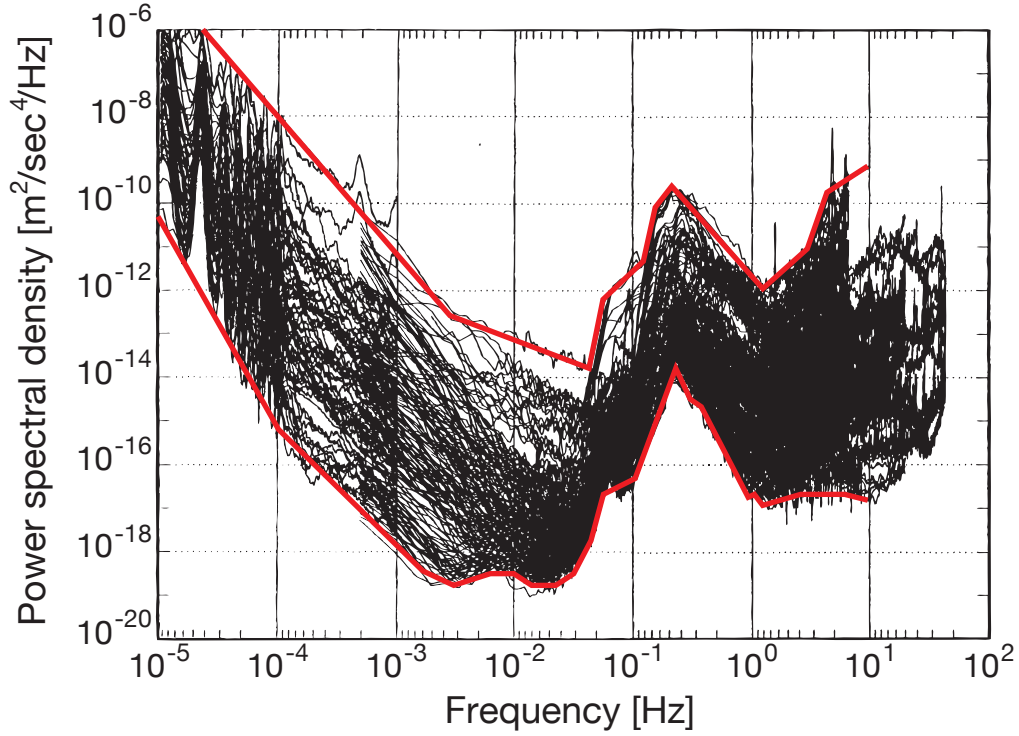
Fig. 2.1. The New High/Low Noise Model (red curves) with the seismic spectra measured in the world wide network of seismometers

Since the microseismic motion around 0.1–1 Hz is not coherent between the test masses located kilometers apart, it can be an obstacle to stable operation of the interferometer.

Seismic motions at high frequency above 1 Hz is of interest for those in the field of gravitational wave detection, since the terrestrial GW telescopes have the best sensitivity in the frequency band. Figure 2.2 shows typical seismic noise spectra at the places where gravitational wave detectors are located. In this frequency region, the magnitude of seismic motion is isotopic, and can be approximated to a simple power law model written as

$$\tilde{x}_{\mathrm{seis}}(f) = A \times \left(\frac{f}{1\,\mathrm{Hz}} \right)^{-2} \quad [\mathrm{m/Hz}^{1/2}] . \tag{2.1}$$

Here the amplitude factor A is typically in the range 10^{-8}–10^{-6} which depends on the site.

The seismic spectra at the underground site in Kamioka is by 1–3 order of magnitude smaller than the other sites of the GW detectors. It is explained that the impact of seismic waves on Earth's surface originated from atmospheric and human activities significantly decreases in underground environment due to the hard bedrock. Thus underground site benefits in the basic vibration level of the ground in the observational frequency region. On the other hand, the microseism around ~ 0.2 Hz is not attenuated so much since it propagates through the continents.
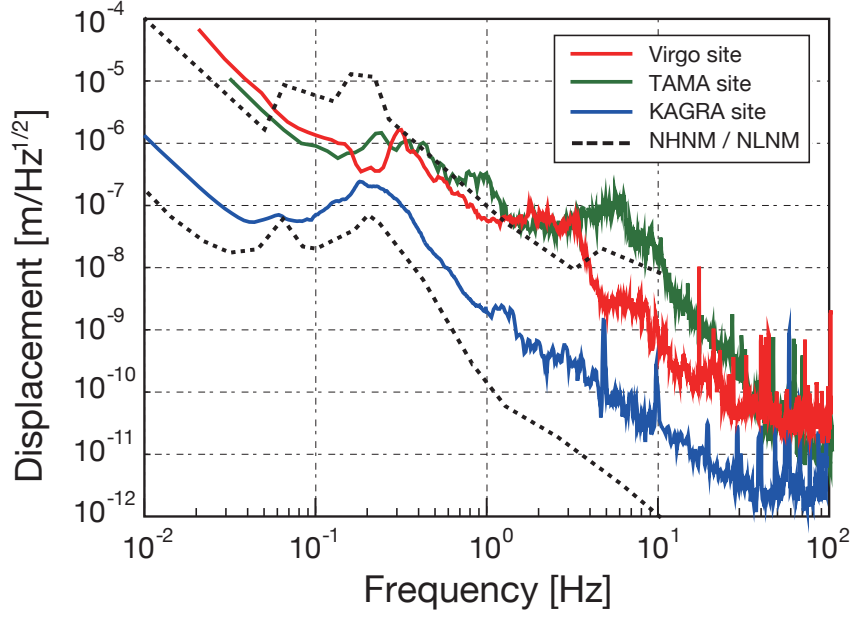
Fig. 2.2. Typical power spectrum density of seismic motions at each sites of the GW detector

The seismic motion in the KAGRA site is typically around 10^{-12}–10^{-10} in 10–100 Hz. Taking into account the magnitude of displacement induced by gravitational waves in the kilometer-scale interferometer as the order of 10^{-20} m, the required seismic attenuation factor is about 10^{-8}–10^{-10}.

2.2 Passive vibration isolation

Vibrations propagate via mechanical waves over connected masses and solid mechanical connections conduct vibrations more efficiently. Passive vibration isolation makes use of soft materials or frexible connections to attenuate the mechanical waves in their transmission path.

Passive vibration isolators can be modeled as a system contains mass, spring, and damping elements and behaves like a harmonic oscillator. Now we consider a simple one-dimensional harmonic oscillator with a spring and a mass, forgetting the damping elements at once, as depicted in the left panel of fig. 2.3. In absense of any external force applied on the suspended mass, the equation of motion of this system is written as

$$M\ddot{x}(t) + k\left(x(t) - x_0(t)\right) = 0 \,, \tag{2.2}$$

where M is the mass of the payload, k is the spring constant or stiffness, x and x_0 are the displacements of the payload and the ground respectively. This equation can be solved in the

frequency domain by taking the Fourier transform then it becomes

$$H(\omega) \equiv \frac{\tilde{x}(\omega)}{\tilde{x_0}(\omega)} = \frac{1}{1 - (\omega/\omega_0)^2} . \tag{2.3}$$

Here we introduced the resonant angular frequency ω_0 of the harmonic oscillation, defined as $\omega_0 \equiv 2\pi f_0 = \sqrt{k/M}$. In eq. (2.3), the $H(\omega)$ is the frequency response of the payload to the ground motion called *vibration isolation ratio*, which indicates how large vibration of the supporting point transmits to the suspended payload in the frequency region.
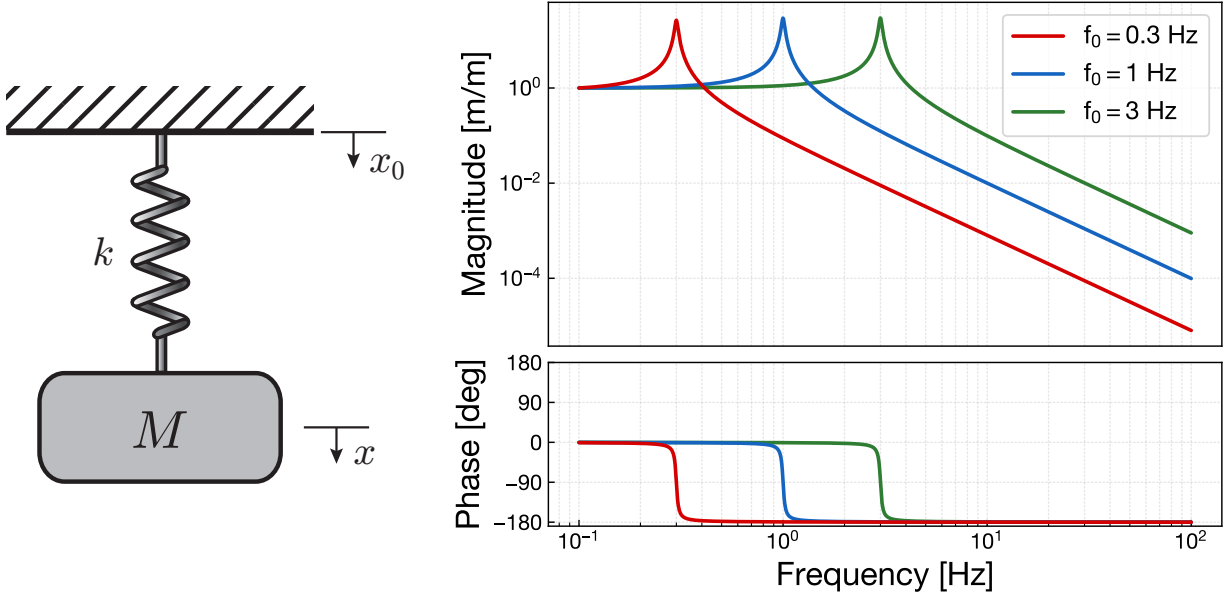
Fig. 2.3. A simple harmonic oscillator composed of a spring and a payload (*left*), and its vibration isolation ratio or frequency response to the ground motion with various resonant frequencies (*right*). For practical appearance, it assumes the quality factor of the resonances as $Q \sim 30$.

The right panel of fig. 2.3 shows the vibration isolation ratio of the harmonic oscillator with changing its resonant frequency. At higher frequencies such that $f \gg f_0$, the amplitude of the vibration isolation ratio rolls off proportional to f^{-2}. It means that the higher frequency of vibration above the resonance, the higher filtering effect the harmonic oscillator realizes. Hence considering a given frequency region of interest such as 10–100 Hz for terrestrial GW observation, a mechanical oscillator with lower resonant frequencies can acquire better seismic attenuation performance, which are shown as the difference of the several curves in fig. 2.3.

To put it the other way around, the mechanical oscillator doesn't have function of vibration filtering in all frequency region. At lower frequencies of $f \ll f_0$ the ground motion transfers directly to the payload without being attenuated. It can be interpreted that, for non-oscillatory variation, the position of the payload follows to that of the suspension point. This behavior is exhibited as the plateau in the magnitude plot of the response in fig. 2.3.
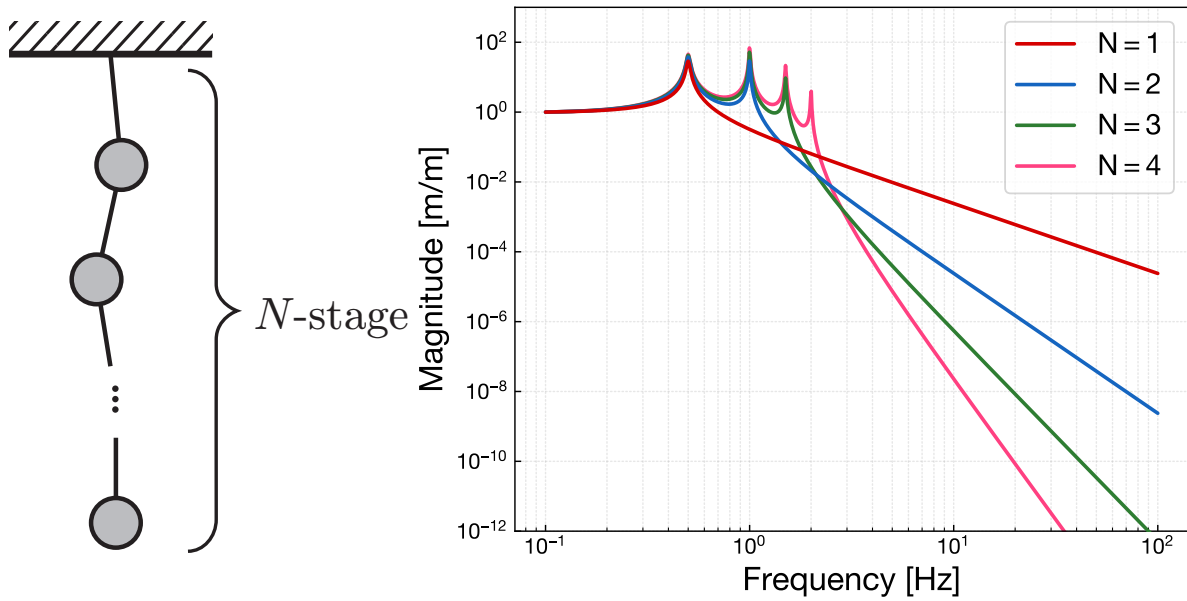
Fig. 2.4. An illustration of N-stage pendulum (*left*), and its vibration isolation ratio with various number of stages (*right*).

The significant feature of the mechanical oscillator is the resonance, around which frequency of f_0 the ground motion gets rather amplified through the system. This behavior appears as the peak in the magnitude plot and the $-180°$ delay in the phase plot. In the case of an ideal harmonic oscillator with no dissipation, the magnitude of the peak goes infinity at the resonant frequency. However, in a practical system the oscillation cannot diverge due to the existense of finite dissipation.

Multistage pendulum

In a kilometer-scale interferometric gravitational wave telescope requires seismic attenuation factor of $\sim 10^{-8}$–10^{-10} around 10–100 Hz. To achieve this attenuation performance with a single pendulum for instance, its length must be order of 10^6 m which is unreasonable in practice. The required attenuation performance can be obtained by cascading mechanical oscillators whose resonant frequenies are sufficiently lower than the frequency region of interest ($\gtrsim 10$ Hz). In an N-stage chain of pendula, the vibration isolation ratio is proportional to f^{-2N} at a higher frequency than the resonant frequencies of the chain. Figure 2.4 illustrates the seismic atternuation performance for various numbers of multistage pendulum chain.
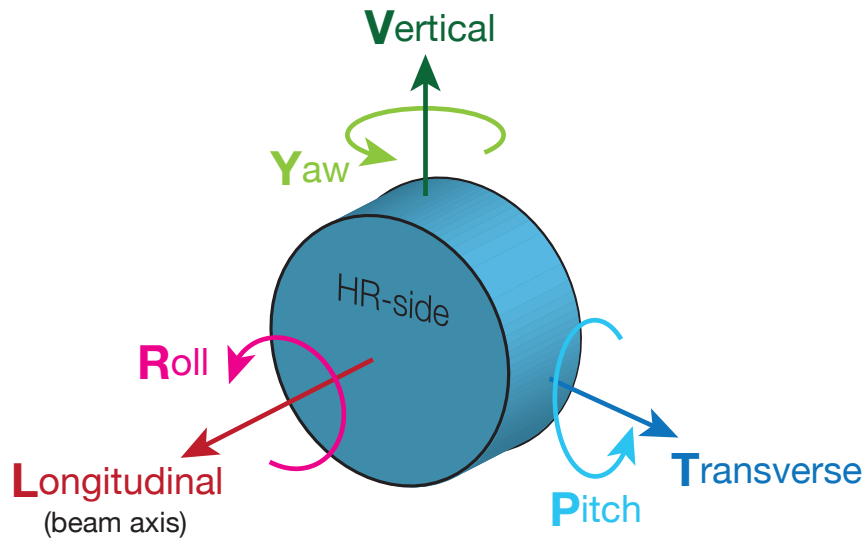
Fig. 2.5. Definition of the degrees of freedom of the suspension's motion. The "HR-side" indicates the surface with high-reflectivity coating. In this thesis, these six degrees of freedom (DoFs) are sometimes abbreviated to their initial letter such as (L, T, V, R, P, Y).

2.3   Suspension's degrees of freedom

In previous section, we considered only one-dimensional motions. However, extending objects to 3-dimensional rigid bodies but still regardless of internal motions such as elastic vibration, we must consider motions in totally 6 degrees of freedom (DoFs) for each body. Conventionally we determine these 6 DoFs, namely longitudinal, transverse, vertical, roll, pitch, and yaw, as illustrated in fig. 2.5. Three translational axes are the right-handed basis for center-of-mass motions, while three rotational axes are defined so that rotations in right-handed screw around the translational axes are positive directions. In this thesis, these six DoFs are sometimes abbreviated to their initial letter such as (L, T, V, R, P, Y) hereafter.

To constract optical cavities and an interferometer, the mirror's motions in not only londitudinal but also other DoFs are of considerable importance. Regarding the mirror as an optical component, one can easily imagine that the longitudinal translation couples directly to the change of the optical path length, and the pitch and yaw rotation affects beam alignment. However, in the case of gravitational wave detectors which are required to achieve ultimate sensitivity, further effects of coupled DoFs need to be taken into account.

One of the coupled DoFs inevitable on the Earth is vertical-to-longitudinal coupling. For the gravitational wave detectors with long arm length constructed on the Earth, because of the finite curvature of the Earth's surface, the direction of the local gravity at the places far apart results imperfect parallelism of verticality. It causes the coupling from local vetical motion of the mirror to global longitudinal variation of the optical cavity, as depicted in
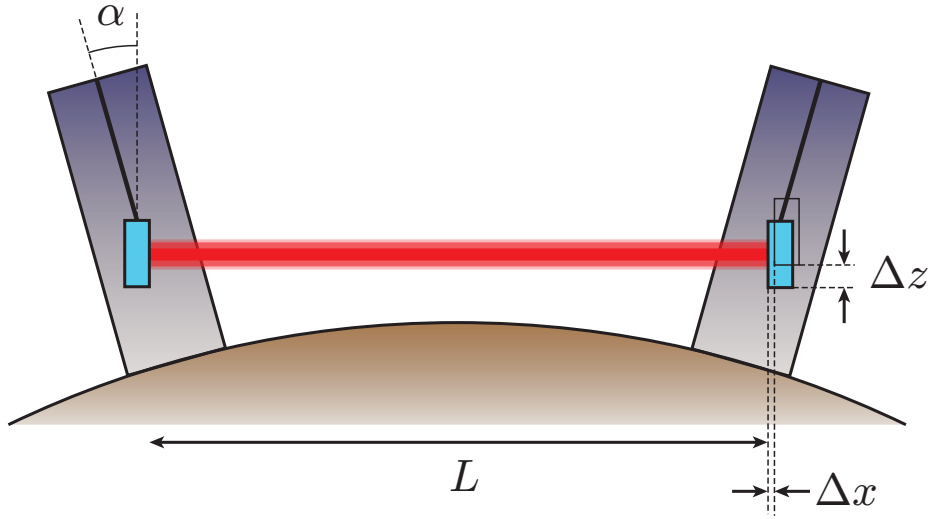
Fig. 2.6. Vertical-to-longitudinal coupling of the mirror motion due to the Earth's curvature.

fig. 2.6. The impact of coupling, $\Delta x = \alpha \, \Delta z$, is related by the factor α which is associated with the separation distance of the mirrors L and the local radius of the Earth $R_{\oplus}$, through the relation $\alpha = L/2R_{\oplus}$. In the case of 3-kilometer separation, one can estimate the typical vertical-to-longitudinal coupling as $\alpha \sim 2.4 \times 10^{-4}$. Achieving the displacement noise of about 10^{-20} m in the observational frequency band, under the isotropic seismic disturbance, we must recognize the necessity of the vibration isolation also in the vertical direction.

2.4 Anti-spring mechanisms

As mentioned in section 2.2, seismic attenuation performance in a given frequency region (e.g. 10–100 Hz for terrestrial gravitational wave detector) can be improved by lowering resonant frequencies of the mechanical oscillators. While using multiplied stages of pendulum, implementation of mechanical oscillators with lower-frequency resonance in a practical dimension is also needed to construct a gravitational wave detector.

This section desctibes two types of harmonic oscillator implemented in the KAGRA suspension systems, an inverted pendulum and a geometric anti-spring filter. Their design incorporates an anti-spring effect which can reduce the effective spring constant of the oscillators, resulting low resonant frequencies while still having compact dimensions. An anti-spring is a system that incorporates a force to push away from its equilibrium point once it displaces. In combination of the anti-spring system with the positive spring constant inherent to most of the mechanical oscillator, the overall stiffness of the system can be tuned to nearly zero.

2.4.1   Inverted pendulum (IP)

An inverted pendulum (IP) is a system that the center of mass of its oscillator is positioned higher than the supporting point on the ground. Unlike an inverted pendulum on a cart in the context of stabilization problems of control theory, we fixed the foot of the IP with a flexure joint onto the ground to obtain a positive angular stiffness k_θ so that the system acquires quasi-stability. By tuning the amount of weight loaded on the top of the IP, it is possible to realize an ultimate low resonant frequency of $\lesssim 100$ mHz in horizontal motion.
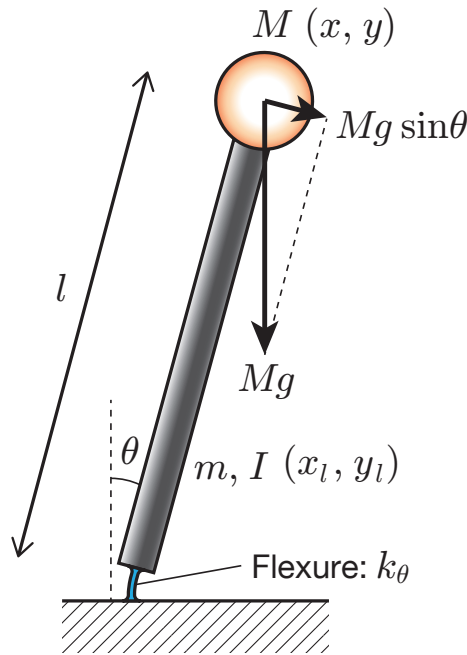
Fig. 2.7. Working principle of an inverted pendulum

Table 2.1. Denotations of the inverted pendulum model

M	mass of the payload
l	length of the IP leg
m	mass of the IP leg
I	moment of inertia about the center of mass of the IP leg
(x, z)	position of the payload
(x_l, z_l)	position of the IP leg
(x_0, z_0)	position of the fixed point of the flexure on the ground
θ	angle of the IP leg with respect to the vertical axis
k_θ	rotational spring constant of the flexure

Working principle

The dynamics shows how the anti-spring effect acts on the intrinsic stiffness of the IP. Given an IP depicted in fig. 2.7 with physical properties which are summarized in table 2.1, the Lagrangian L of the system is determined as

$$L = K - U, \tag{2.4}$$

$$K = \frac{1}{2}M\left(\dot{x}^2 + \dot{z}^2\right) + \frac{1}{2}m\left(\dot{x}_l^2 + \dot{z}_l^2\right) + \frac{1}{2}I\ddot{\theta}, \tag{2.5}$$

$$U = Mgz + mgz_l + \frac{1}{2}k_\theta\theta^2, \tag{2.6}$$

where K and U represent the kinetic and the potential energy, respectively. Under the geometrical constraints as follows,

$$
\begin{aligned}
x_l &= \frac{1}{2}(x + x_0) \\
z_l &= \frac{1}{2}z \\
x &= l\sin\theta + x_0 \\
z &= l\cos\theta
\end{aligned}
\tag{2.7}
$$

the kinetic energy and the potential energy can be simplified as

$$K = \frac{1}{2}M\dot{x}^2 + \frac{1}{8}\left(\dot{x} + \dot{x}_0\right)^2 + \frac{1}{2}I\left(\frac{\dot{x} - \dot{x}_0}{l}\right)^2, \tag{2.8}$$

$$U = Mgl\cos\left(\frac{x - x_0}{l}\right) + \frac{mgl}{2}\cos\left(\frac{x - x_0}{l}\right) + \frac{1}{2}k_\theta\left(\frac{x - x_0}{l}\right)^2. \tag{2.9}$$

The Euler-Lagrange equation of motion is therefore, with the 1st-order approximation, written as,

$$\frac{\mathrm{d}}{\mathrm{d}t}\frac{\partial K}{\partial \dot{x}} = \frac{\partial U}{\partial x}, \tag{2.10}$$

$$\left(M + \frac{m}{4} + \frac{I}{l^2}\right)\ddot{x} + \left(\frac{m}{4} - \frac{I}{l^2}\right)\ddot{x}_0 = -\left[\frac{k_\theta}{l^2} - \left(M + \frac{m}{2}\right)\frac{g}{l}\right](x - x_0). \tag{2.11}$$

One can regard (2.11) as the equation of motion of a harmonic oscillator with an effective spring constant k_{eff},

$$k_{\text{eff}} = \frac{k_\theta}{l^2} - \left(M + \frac{m}{2}\right)\frac{g}{l}. \tag{2.12}$$

The first term of k_{eff} represents the elastic restoring force of the flexure. In contrast, the second term appears the repulsive force which acts to reduce the effective stiffness of the harmonic oscillation. This effect is called *gravitational anti-spring force*. Since the gravitational anti-spring force is proportional to the mass of the payload and the IP leg, the effective spring constant can be tuned by changing the load on the IP.
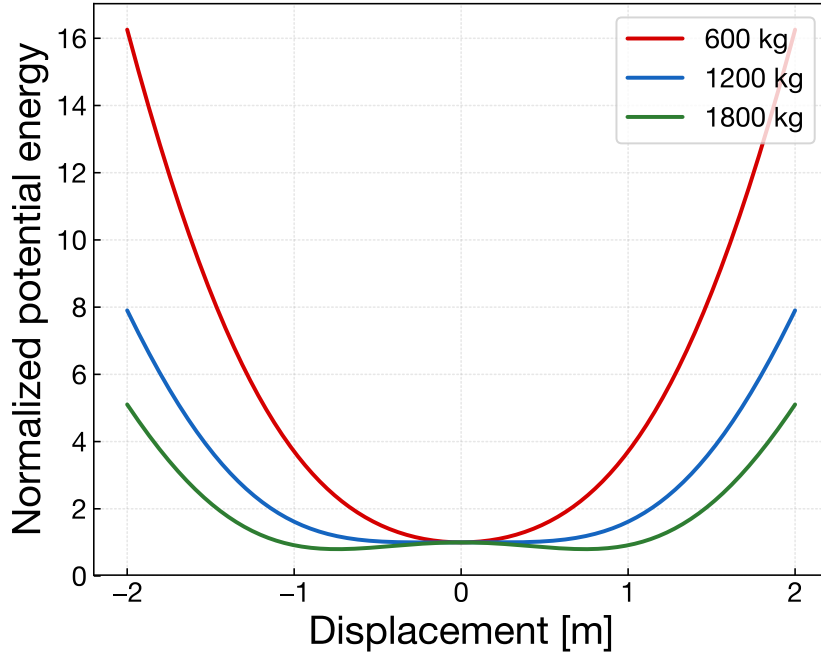
Fig. 2.8. Potential energy of the IP with different loads

However, perfect cancellation of the restoring force and repulsive force makes the system no longer oscillatory with a single equilibrium point. Recalling (2.9), the potential energy of the IP with various loads is plotted in Fig 2.8. When the IP is not sufficiently loaded, its potential energy can be approximated to a parabolic curve dominated by the third term of (2.9). As more weight loaded on the IP, the potential curve gets flattened around its equilibrium point of $x = x_0$. Beyond the critical loading, the first term of (2.9) become raised and the system shows bistability having two equilibrium points. For stable operation of the vertically-standing IP, the load must be small enough to keep the effective spring constant to be a positive value.

In a stable condition that the IP has only one equilibrium point, from (2.12), the resonant frequency of the IP is determined as

$$f_0 = \frac{1}{2\pi} \sqrt{\frac{k_{\text{eff}}}{M + \frac{m}{4} + \frac{I}{l^2}}} \; . \tag{2.13}$$

With a set of parameters shown in table, the dependence of the resonant frequency on the mass of load is presented in Fig. 2.9. When increasing the load on the IP, the resonant frequency gradually decreases and then drastically drops at the last moment the system goes unstable.
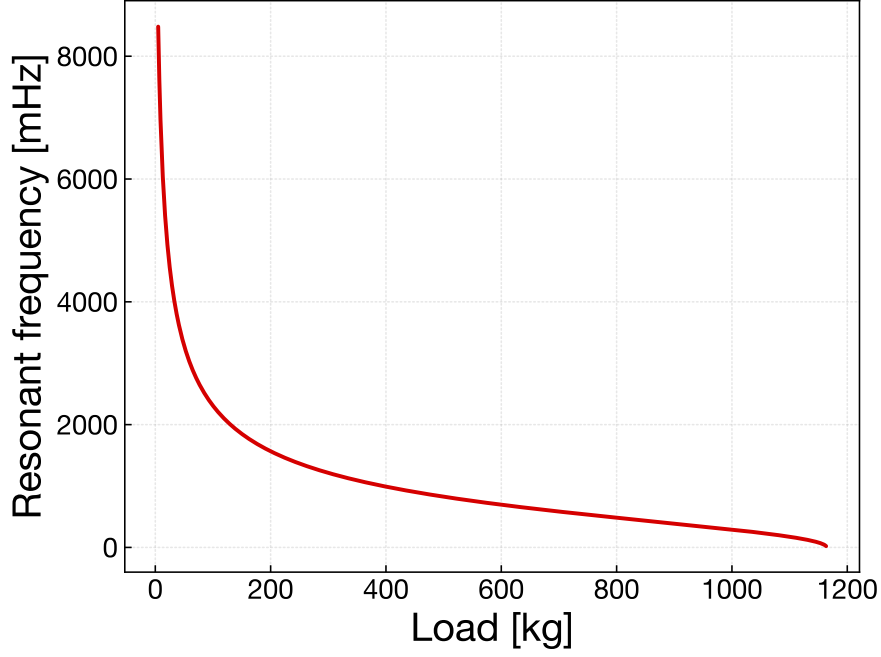
Fig. 2.9. Change of the resonant frequency of the IP with respect to the mass of load

Attenuation performance

The transfer function from the ground motion to the payload is obtained by solving eq. (2.11) in frequency domain.

$$H_{\text{IP}}(\omega) = \frac{\tilde{x}}{\tilde{x}_0} = \frac{k_{\text{eff}} + \left(\frac{m}{4} - \frac{I}{l^2}\right)\omega^2}{k_{\text{eff}} - \left(M + \frac{m}{4} + \frac{I}{l^2}\right)\omega^2}$$
$$= \frac{A + B\omega^2}{A - \omega^2}, \tag{2.14}$$

where,

$$A = \frac{k_{\text{eff}}}{M + \frac{m}{4} + \frac{I}{l^2}}, \quad B = \frac{\frac{m}{4} - \frac{I}{l^2}}{M + \frac{m}{4} + \frac{I}{l^2}}. \tag{2.15}$$

Seeing the plotted curve of this transfer function in Figure 2.10, the IP behaves similarly to an ideal harmonic oscillator up to a certain frequency above the resonance. However, the attenuation performance of the IP saturates at a level due to the coefficient B appeared in eq. (2.14).

This saturation is due to a residual momentum transfer from the leg to the payload caused by so-called *center of percussion effect*. When an inpulsive force is applied onto a rigid body, the blow accelerates the body both in translation of its center of mass and in rotation around its center of mass, as illustrated in fig. 2.11. At this moment there exists a point where the translation and rotation cancel each other out and the net initial velocity
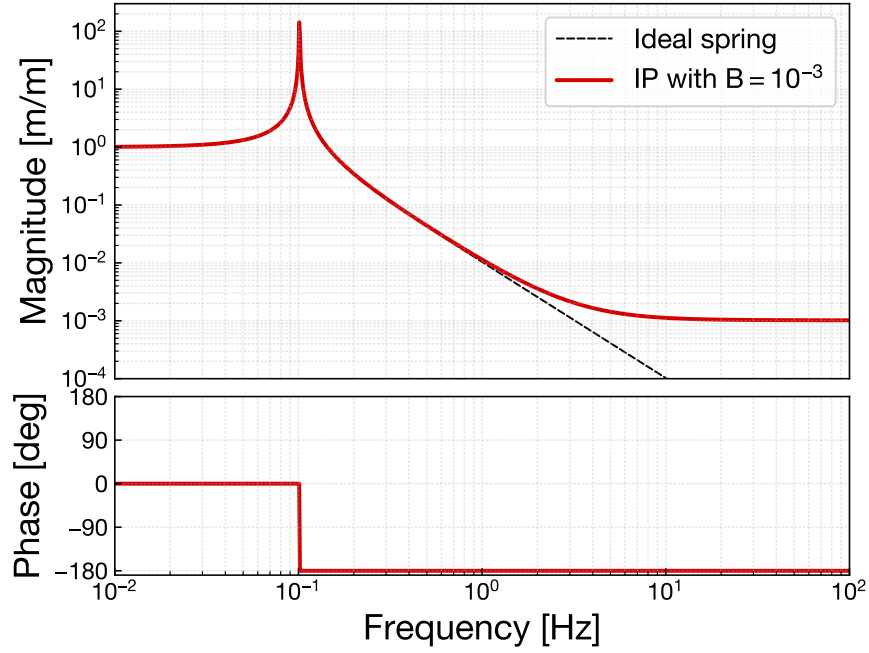
Fig. 2.10. Transfer function from the ground motion to the payload of the IP. That of an ideal harmonic oscillator is also plotted for comparison.

becomes zero. This point is called *pivot point* or in other fields *sweet spot*, which we can regard as the momentary center of rotation for the impulse. The location of the pivot point is determined by the mass distribution of the body and not necessarily within the boundary of the body.

The pivot point has a complementary point on the opposite side of the center of mass, the *center of percussion* (CoP). As mentioned before, a perpendicular impulse applied at a CoP will produce no reactive force at its corresponding pivot point. The position of CoP and pivot point from its center of mass is tied with the following equation.

$$r_\text{f}\, r_\text{p} = \frac{I_\text{body}}{M_\text{body}} \tag{2.16}$$

Here r_f and r_p are the radius of the CoP and that of the pivot point (see fig. 2.11), and M_body and I_body are the mass and moment of inertia of the body, respectively. This relationship indicates that the CoP and pivot point will swap positions when the impulse is applied on the other side of the center of mass.

In the case of IP legs, they have mechanical constraint that one end is conencted to the payload and the other is fixed to the ground via the flexure, not allowing to rotate freely. This constraint is substantial at low frequencies so that the IP behaves as expected like an harmonic oscillator with a low-frequency resonance. However, the constraint becomes fainter at higher frequencies which allows the IP leg to perform free rotation around its pivot point.
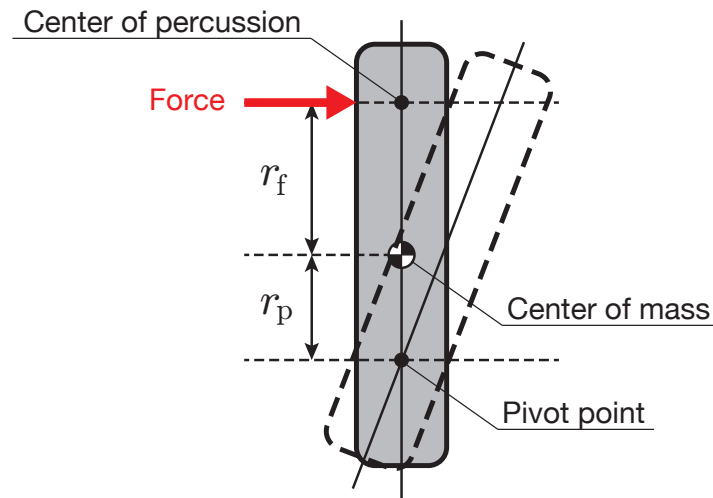
Fig. 2.11. Illustration of the center of percussion. When a rigid body receives an impulsive force which is not aligned to its center of mass, the body is subject to momentary acceleration both in translation of its center of mass and in roration around its center of mass. There exists a point *pivot point*, where the translation and rotation cancel each other out and the net initial velocity becomes zero. The *center of percussion* is the comprementary point for the pivot point located at the other side of the center of mass. In other words, the center of percussion is the point where a perpendicular impulse doesn't produce any reactive force at the given pivot point.

In order to reduce the residual momentum transfer from the leg to the payload, one needs to let the position of the center of percussion corresponding to the top end of the IP leg coincide with the foot of the flexure where the external force (ground motion) is applied. This allows the IP leg to rotate around its top end as the pivot point without exerting a force on the payload.

One solution to adjust the position of the CoP is to add a counterweight to the bottom of the IP leg since its position depends on the mass distribution of the body. Figure 2.13 shows improvement of the saturation level in the vibration isolation ratio by introducing the counterweight. Typically, adjusted counterweights can mitigate the saturation level by 1–2 orders of magnitude in practice. For instance, the IP of the HAM-SAS developed for Advanced LIGO achieved $\sim 10^{-3}$ attenuation without counterweights and $\sim 10^{-5} - 10^{-4}$ with them, with well-cared lightness of the aluminum hollow leg of about 0.2 kg. The presence of a notch followed by the plateau depends on which direction (upper or lower) the position of the pivot point is offset from the target point.
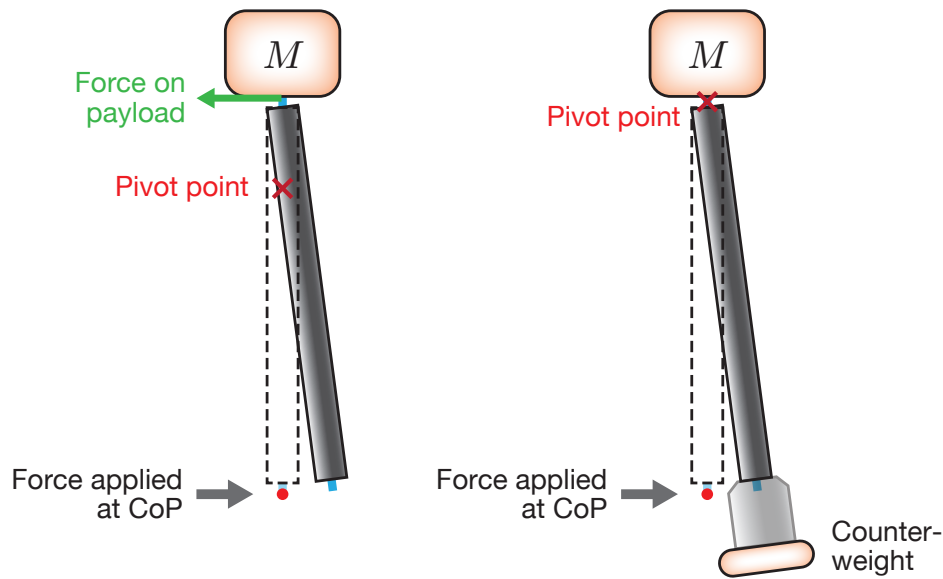
Fig. 2.12. Illustration of the effect of a counterweight on the pivot point. In general, the pivot point complementary to the center of percussion located at the bottom flexure doesn't coincide with the connecting part of the payload. Adding a counterweight at the bottom of the leg can place the pivot point to the top connecting part so that the IP leg can rotate without exerting a force on the payload, thereby improving its isolation performance from the ground.

2.4.2   Geometric Anti-Spring (GAS) filter

A geometric anti-spring (GAS) filter is a mechanical oscillator with use of radially converging compressed cantilever blades to obtain a low resonant frequency in vertical direction under heavy load. The quasi-triangular cantilever blades are positioned

Working principle

Here a brief dynamics of the GAS filter is presented to understand implementation of its anti-spring mechanism. The behavior of a GAS filter is modeled as a system that a payload is supported with a combination of normal vertical spring and a set of horizontal springs which are compressed each other, as illustrated in fig. 2.14. Owing to the radially symmetric configuration of the cantilever blades, the horizontal components of the reaction forces against compression vanish out and thereby the keystone is constrained to move only in vertical direction.

The keystone of the GAS filter stays at a working point $z = z_{\mathrm{eq}}$, where the constant load Mg and the static force of the vertical spring are balanced, as well as the conceptual horizontal springs become orthogonal to the z-axis ($\theta = 0$) and experience maximum compression. Here
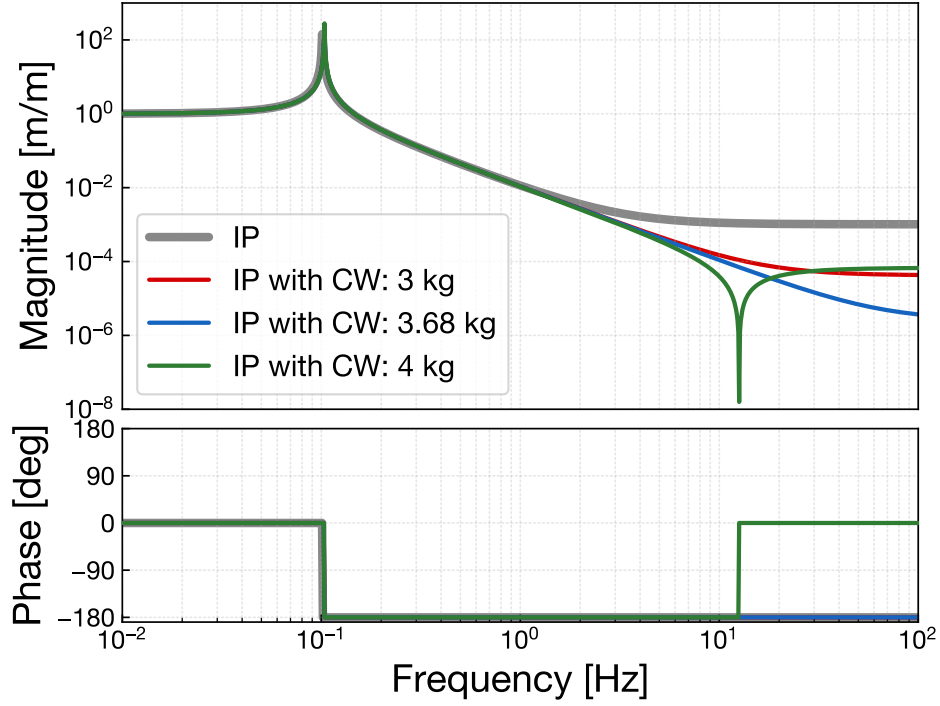
Fig. 2.13. Vibration isolation ratio of the IP with different loads of the counterweight (CW). The saturation level can be improved by 1–2 orders of magnitude with the counterweights. The presence of a notch at the frequency of ~ 12Hz depends on which direction (upper or lower) the pivot point is offset from the target position.

g denotes gravitational acceleration, M the mass of the payload. When the keystone is displaced from the equilibrium, its equation of motion is described as,

$$M\ddot{z} = -k_z(z - z_{\text{eq}}) - k_x(l_x - l_{x0})\sin\theta\,, \tag{2.17}$$

where k_z and k_x are the spring constant of the vertical and horizontal spring, l_x and l_{x0} are the actual length and the natural length of the horizontal spring, respectively. In addition, the working point can be written as $z_{\text{eq}} = Mg/k_z$ due to the balance condition. Considering only the small motions around the working point, eq. (2.17) can be linearized as,

$$M\ddot{z} = -\left[k_z - \left(\frac{l_{x0}}{x_0} - 1\right)k_x\right](z - z_{\text{eq}})\,, \tag{2.18}$$

where x_0 denotes the length of the horizontal spring at the equilibrium. From this equation, we can obtain the effective spring constant of the GAS filter as,

$$k_{\text{eff}} \sim k_z - \left(\frac{l_{x0}}{x_0} - 1\right)k_x\,. \tag{2.19}$$

This formula indicates that the effective spring constant decreases when the horizontal springs are under compression ($x_0 < l_{x0}$). The second term proportional to k_x corresponds to the
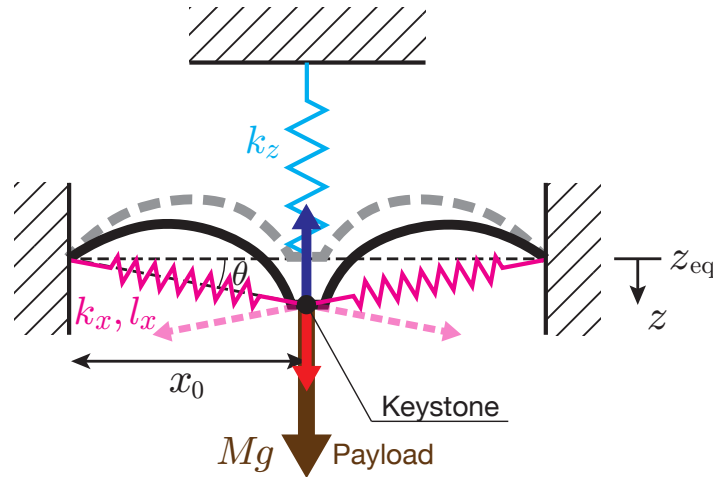
Fig. 2.14. Conceptual representation of a geometric anti-spring (GAS) filter. A set of cantilever blades are compressed each other supporting the keystone subject to the payload. The system can be modeled with a normal vertical spring (light blue) and a combination of compressed horizontal springs (pink). When the keystone is displaced, the horizontal components of the reaction forces against compression cancel each other out (faint dotted pink arrow) and the net repulsive force along the z-axis (red arrow) remains. The resultant stiffness of the keystone is the sum of contributions from the intrinsic vertical spring and the net horizontal springs.

repulsive force along the z-axis which mitigates the intrinsic stiffness k_z. The geometric constraint on the keystone or the tip of the cantilever blades enables the stiffness cancellation in vertical motions and therefore the mechanism is called *geometric anti-spring* effect. Since this anti-spring mechanism is a local effect around the working point, the capability to support a heavy payload is maintained.

Attenuation performance

The transfer function from the reference frame to the keystone can be written as the same equation as the IP's one in eq. (2.14). Due to the CoP effect, the seismic attenuation performance of the GAS filter saturates at high frequencies which is typically limited to $\sim 10^{-3}$. It can be improved by mounting a compensation wand in parallel to the blades with couterweight. With a proper amount of the counterweight adjusting the position of the CoP to correspond to the fixing radius of the blades, the saturation level can be mitigated to about 10^{-4}.

Thermal stability

The soft supporting of the GAS in vertical direction is provided by the compressed blade springs with their elastic deformation. Thus the strength of its repulsive force is sensitive to the change of the physical properties of the blade. In particular, the temperature dependency of the Young modulus can cause the drift of the working point of the keystone. The amount of the change in the keystone's working point becomes larger when the resonant frequency of the GAS is tuned to be lower, which relationship can be typically evaluated as,

$$\frac{\Delta z}{\Delta T} = \frac{g}{E\omega_0^2}\frac{\partial E}{\partial T}$$

$$= 0.69 \text{ [mm/K]} \left(\frac{0.33 \text{ Hz}}{\omega_0^2/2\pi}\right)^2 \left(\frac{\frac{1}{E}\frac{\partial E}{\partial T}}{3.0 \times 10^{-4} \text{ K}^{-1}}\right), \tag{2.20}$$

where ΔT is the temperature change, E is the Young modulus of the blade material, ω_0 is the angular resonant frequency of the GAS. It indicates that a non-negligible change of the height (in the order of millimeters) will take place in the optics suspended at the bottom when the suspension has plural stages of the GAS filter. For this reason, the environmental temperature of the instruments has to be kept sufficiently stable.

2.5 Active vibration isolation

While the passive vibration isolation utilizes intrinsic low-pass characteristics of mechanical oscillators, the seismic attenuation is valid only at high frequencies above its resonant frequency. If one aims to isolate the objects in a low frequency region such as the microseismic disturbance around 0.2–0.5 Hz, the passive isolation scheme feels awkward with the issue without using the negative-stiffness components. On the other hand, active vibration isolation which implements sensors, actuators, and controllers can be effectively reduce the seismic transmissivity to the target object in an arbitary frequency band in principle.

The basic concept of the active vibration isolation is a feedback control with an inertial sensor mounted on the target object supported with spring-like elements. The inertial sensor monitors the absolute motion of the object with respect to the inertial frame. The signal from the inertial sensor is processed via the servo controller and then sent to the actuator in order to generate a motion-canceling force on the suspended body. This method can be effective as long as the intertial sensor has enough sensitivity to detect the motion of the target object without being limited by the sensor noise in the frequency region of interest. However in practice, because of the AC-coupled feature of the general inertial sensors, the active isolation requires supplementary sensors and control loops such as relative displacement sensor for low-frequency stabilization and witness sensors placed on the ground for feedforward control and sensor correction.

The active vibration isolation is implemented on the inertial seismic isolators in Advanced LIGO suspensions. Detailed discussion on the active isolation strategy and instrumentation is available in [**Matichard2015**].

Chapter 3

KAGRA Type-A Suspension

In this chapter, we describe the design and setup of Type-A suspension system, the suspension system for KAGRA test masses and charanterized in this study. Section 3.1 briefly mentions the overall configuration of the KAGRA interferometer. In section 3.2, we review the suspension systems used for vibration isolation in KAGRA. From section 3.3 the detailed design of Type-A suspension is explained, containing mechanical components, electric devices such as sensors and actuators, and control systems. Although this chapter focuses on describing the Type-A suspension as the main subject of the study, most of the components enumerated above are shared with other types of suspension systems. Thus not only the Type-A suspension but also all suspension systems in KAGRA are the topic of this chapter.

3.1 Overview of KAGRA interferometer

KAGRA is a power- and signal-recycling (also reffered to as *dual recycling*) Fabry-Perot Michelson interferometer with 3 km arm length. At the time of writing this thesis, KAGRA was in a major upgrade campaign where suspension systems for core optics have been installed and the outline of the full configuration was getting into practice. In May 2018, KAGRA once experienced a test operation with simplified Michelson interferometer formed by a cryogenic test mass. After the major upgrade until 2019, KAGRA will perticipate the joint observation with Advanced LIGO and Advanced Virgo, called *observation run 3* or O3 in short, with imcomplete sensitivity corresponding a few (tens of) megaparsec of inspiral range. KAGRA will start observations with its full sensitivity in 2020s.

3.1.1 Conceptual design

The sensitivity of KAGRA is shown in fig. 3.1 which is generated from the design parameters summarized in table 3.1. There are two types of operational mode in KAGRA,
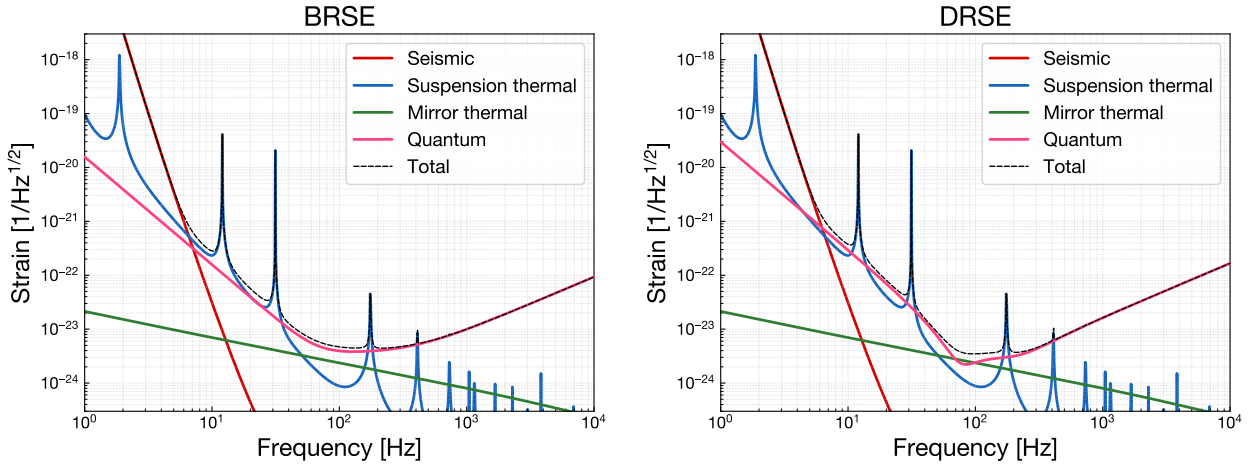
Fig. 3.1. Sensitivity curves and breakdowns of noise contributions in two operational modes of KAGRA interferometer. The *left* panel shows the broadband RSE (BRSE) configuration, while the *right* panel shows the detuned RSE (DRSE) configuration.

broadband resonant sideband extraction (BRSE) and detuned resonant sideband extraction (DRSE). In the BRSE operation, there is additionally an option of homodyne detection. We can switch the operational mode of the interferometer depending on which purpose we give priority to.

The sensitivity curve is designed to be dominated by the fundamental quantum noises, the shot noise at high frequencies and the radiation pressure noise at low frequencies[7]. Although some peaks from suspension thermal noise exceeds the quantum noises, it would be less problematic. At the most sensitive frequency region the mirror thermal noise, mainly contributed from the thermal dissipation of reflective coating layers, shows predominance even with cryogenic temperature. The sensitivity below 10 Hz is dominated by seismic noise and gravity-gradient noise.

In the design of KAGRA, we introduces two unique features to improve its sensitivity, a use of underground environment and cryogenic test masses. These are some of advanced options to be implemented in the next generation gravitational wave telescopes. Therefore KAGRA has an aspect of a laboratory to demonstrate feasibility and usefulness of these techniques.

Underground environment

Underground environment of the Kamioka mine is one of the unique features among the 2nd-generation gravitational wave observatories. The central station of KAGRA is situated at 36.41°N and 137.31°E inside the 1300-meter-high mountain Ikenoyama, where other observatories of high-energy physics such as Super-Kamiokande and XMASS are also constructed. Even though the KAGRA tunnel occupies L-shaped space 3 km on a side, in addition the

**Table 3.1.** Main design parameters for KAGRA interferometer.

Parameter	Design value
Baseline length	3 km
Laser wavelength	1064 nm
Laser power at BS	674 W
Material of test mass substrate	Sapphire
Material of test mass coating	Silica/Tantala
Test mass diameter	22 cm
Test mass thickness	15 cm
Test mass weight	22.8 kg
Temperature of test mass	22 K
Suspension wire for test mass	Sapphire
Inspiral range (BRSE)	128 Mpc
Inspiral range (DRSE)	153 Mpc

end of the arms reaches close to the foot of the mountain, the end test masses are at least 200 m below the ground surface[6].

The first explicit advantage of the underground environment is tranquility of the seismic vibraiton as described in sec. 2.1. This low seismic vibration helps us to achieve required displacement noise in the observation band and stable operation of the interferometer.

In advance of the selection of KAGRA location, a joint research project of the Disaster Prevention Research Institute and Cryogenic Laser Interferometer Observatory (CLIO) performed a long period observation of the seismic vibration in the Kamioka mine. T. Sekiguchi's analysis of a 1.5-year data (2009.09–2011.02) from the measurement formulated the seismic noise models plotted in fig. 3.2. The three curves represent seismic noise spectra at the 90th (high), 50th (mean), and 10th (low) percentile levels respectively. The spectra below 1 Hz are the measured data in the 1.5-year observation, while those above 1 Hz are the extrapolation of the measurement results assuming proportional to f^{-2}. Since the seismometer CMG-T3 used in the measurement has worse noise level above 1 Hz, the f^{-2}-proportionality at higher frequenies is confirmed through another measurement by M. Beker who uses a different seismometer Trillium 240 at the CLIO site. Note that the spectra below 50 mHz is also contaminated by the sensor noise of the CMG-T3.

The microseismic peak around 0.2 Hz shows large variation in magnitude since the amplitude depends on the oceanic activity and thus on the weather condition. The RMS displacement of the seismic motion (cumulatively integrated down to 10^{-2} Hz) varies in the range of 0.08–0.5 μm with the 10–90 percentile range. In the following discussions, we take the high noise model in fig. 3.2 as the seimic vibration spectrum for a conservative estimate.
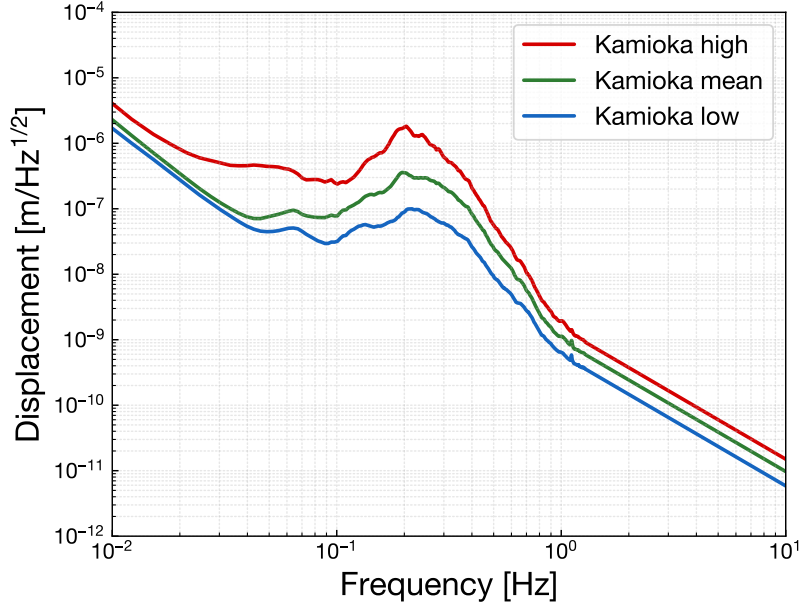
Fig. 3.2. Seismic noise spectra of the Kamioka mine. The three curves represent the seismic noise spectrum of 90th (high, *red*), 50th (mean, *green*), and 10th (low, *blue*) percentile levels respectively. The spectra below 1 Hz are the measurement results, while those above 1 Hz are the extrapolation of the measured data assuming proportional to f^{-2}.

Figure 3.2 indicates that the spontaneous displacement noise in the Kamioka mine is $\sim 10^{-11}$ m/Hz$^{1/2}$ at 10 Hz. Therefore, required attenuation ratio at that frequency is about 10^{-8} for the test masses.

The second advantage of the underground environment is low gravity-gradient noise which can potentially limit the sensitivity at the lower end of the observation band. Gravity-gradient noise originates from both atmospheric and seismic density fluctuation, producing a varying gravitational force on the test mass. The main sources of this noise can be surface waves of human-induced activity, a bulk motion of the ground or atmospheric phenomena. Unlike the direct transmission of the seismic noise, the gravity-gradient noise cannot be attenuated with any shields or filters in the path of gravitational coupling. Hence, the situation of the interferometer determines the available noise limit.

The underground situation can improve the gravity-gradient noise from both surface waves of the ground and atmospheric fluctuation. J. Harms estimated the gravity-gradient noise from these sources at the Kamioka mine as $\sim 10^{-20}$ m/Hz$^{1/2}$ at 10 Hz, based on a seismic vibration measurement at the CLIO site. This value is by 2–3 orders of magnitude smaller than the requirement and $\sim 10^{-2}$–10^{-1} times as large as that of the site of Advanced LIGO. Meanwhile, the contribution from water flow near the interferometer may generate gravitational potential perturbation in considerable magnitude since a substantial amount of water is welling anywhere inside the tunnel. The impact of gravity-gradient noise from this

Table 3.2. Material properties of the candidates for mirror components

| Material	Sapphire	Silicon	Fused silica
Density [g/cm^3]	3.98		
Young modulus [GPa]	398		
Poisson ratio	0.22		
Thermal contuctivity [W m^{-1} K^{-1}]	4300	2330 @ 10 K	0.7
Q-factor (20K)	10^8	10^8	10^3
Q-factor (300K)	3×10^6	10^6	10^7
Absorption @ 1064 nm			

water flow is under investigation.

Cryogenic sapphire test masses

The use of cryogenic mirrors is a simple solution to improve the noise contamination originated from thermal fluctuations, since energy of the thermal noise is proportional to the product of temperature and mechanical dissipation. Therefore it is effective to cool the mirrors down to the cryogenic temperatures and to select a high-Q material as the substrate. In the setup of a laser interferometer, two thermal processes violate the gravitational wave detection; the suspension thermal noise, which is fluctuation of the suspension point causes translation of the center of mass of the mirror, and the mirror thermal noise, which is the sum of mechanical dissipations in the substrate and coating of the mirror.

In KAGRA, sapphire is chosen as a material for the substrate and suspension wire of the test masses. The properties of the candidate materials for mirror components of gravitational wave detectors are summarized in table 3.2. Among the candidate materials, sapphire has propeteies of high Q-factor, high thermal conductivity, and low optical absorption of 1064 nm wavelength laser at cryogenic temperatures. The high density feature of sapphire also helps to make the mirror heavier with a given volume, resulting high inertia. However fused silica used for mirrors in Advanced LIGO shows characteristics suitable to the laser interferometer, cooling down to cryogenic temperatures deteriorates its Q-factor roughly from 10^7 to 10^3, by 4 orders of magnitude.

3.1.2 Optical layout

The KAGRA interferometer is composed of a number of optical components including not only the main parts of the dual-recycled Fabry-Perot Michelson interferometer but also input, output and auxiliary optics. A schematics of the optical layout of the KAGRA is shown in fig. 3.3.
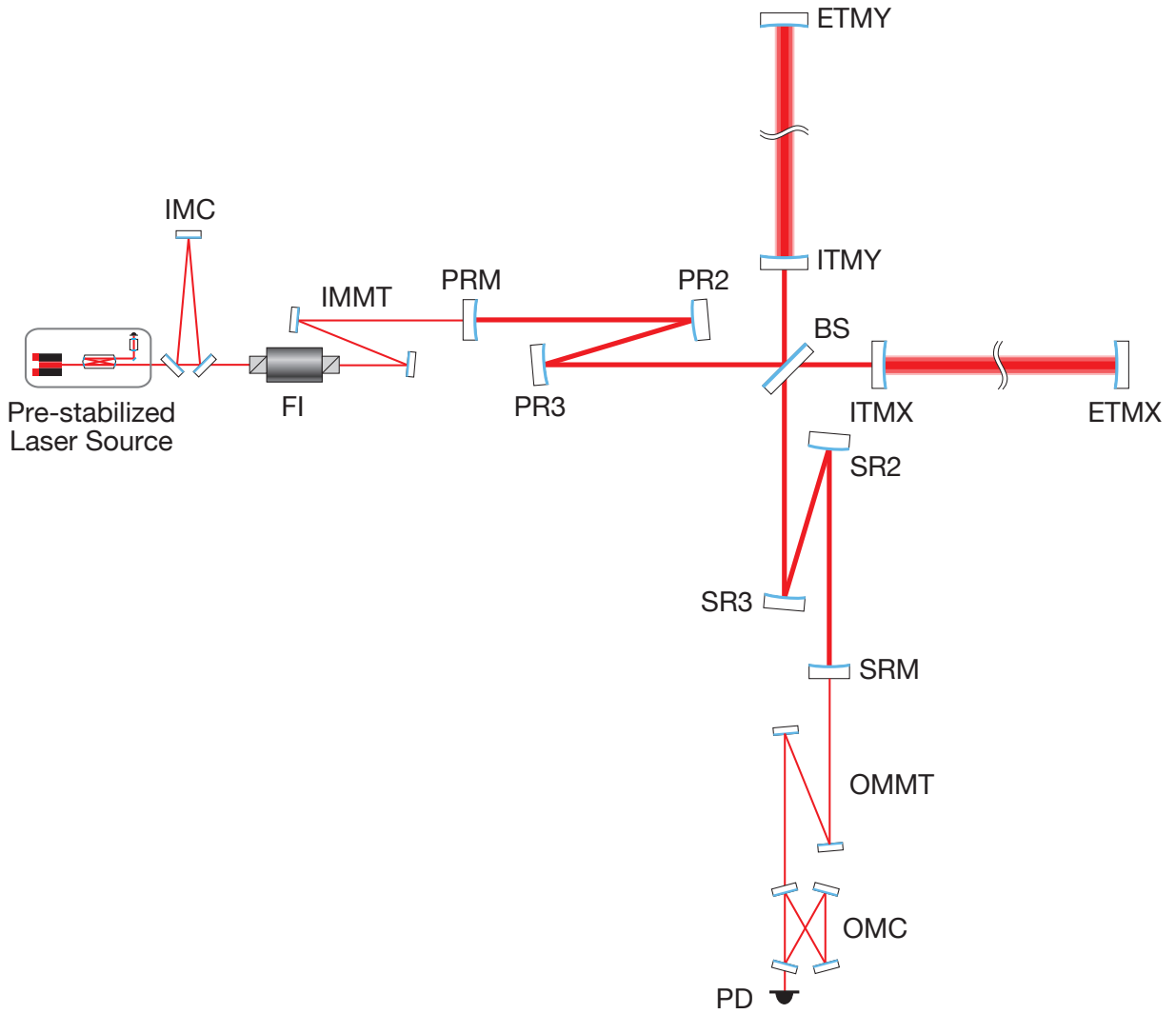
Fig. 3.3. A schematics of the optical layout of the KAGRA interferometer.

The laser source is a Nd:YAG non-planar ring oscillator (NPRO) which has very low intensity noise. Passing through the solid-state amplifier with increasing power of about ~ 200 W, the laser beam goes to the pre-stabilization stage which applies further intensity stabilization with a pre-mode cleaner, a bow-tie shaped rigid cavity, and frequency stabilizaiton with a rigid reference cavity with high finesse. These pre-stabilization processes are implemented on an in-air breadboard, while following optical path and components are placed under vacuum environment.

The pre-stabilized laser beam is sent to the input mode cleaner (IMC), a triangular cavity with suspended mirrors for the purpose of spacial mode shaping and further frequency stalbilization. The transmitted beam from the IMC goes through an Faraday isolater (FI) which blocks back-streaming light by a combination of Faraday rotator and two polarizer to

force one-way trip on the passing beam. Then the outcoming beam is magnified through the input mode matching telescope (IMMT) which has a function of spatial mode shaping to match the beam to the following optical cavities. Thus after these preprocessing the dressed beam is sent to the main part of the interferometer.

The main part of the interferometer is a dual-recycled Fabry-Perot Michelson interferometer with two 3 km-long arm length. The arm cavities are conventionally called X-arm and Y-arm, formed by the input test masses (ITMs) and the end test masses (ETMs). The incoming beam is divided into two perpendicular directions at the beam splitter (BS) and send to the arm cavities. The reflected beams from the arm cavities are recombined at the BS. Their interference condition on the BS is retained such that all the power is going back to the incoming direction called symmetric port.

There are two folded recycling cavities at the input and output of the main interferometer. At the input (symmetric port), the power recycling mirror (PRM) reflects the back-coming beam again to the arm cavities. The power recycling cavity, formed by the PRM and equivalent ITM (a virtual ITM located at the averaged distance of the ITMX and ITMY from the BS) stores the reflected power from the arm cavities, resulting to amplify the effective intracavity power of the arms. Similarly, a signal recycling cavity is implemented at the output (anti-symmetric port) of the Michelson interferometer. Although the interfered light is kept dark during observation, a tiny amount of power leaks out at the anti-symmetric port when gravitational waves pass through the interferometer. The signal recycling mirror (SRM) send the leaked photons (signal of the GWs) back to the arm cavities in order to make more interaction of the photons with the gravitational waves.

Finally the leaked beam from the signal recycling cavity is detected at the photo-detector (PD), with post-processing through the output mode matching telescope (OMMT) and the output mode cleaner (OMC). The OMMT diminishes the beam radius with shaping its spacial mode in order to match to the following OMC cavity. The OMC is a bow-tie shaped cavity mounted on a monolithic breadboard with less thermal expansion.

3.2 Overview of KAGRA suspension systems

The main interferometer of KAGRA consists of a number of optics, whose fluctuation has different level of impact on gravitaitonal wave detection depending on its position. Hence, we employ three types of suspension systems for the optics of the main interferometer, namely Type-A, Type-B, and Type-Bp suspension in the order from larger size. The overview and configuration of these three types of suspensions are shown in fig. 3.4 and fig. 3.5, respectively. A basic information of the suspension types are also listed in table 3.3.

The Type-A suspension is the largest vibration isolation system for the cryogenic test masses in the 3 km arm cavity. Since the local motion of the test masses directly couples to

Table 3.3. Basic specification of the three types of the KAGRA suspension systems

	Type-A	Type-B	Type-Bp
Assigned optics	ITMX	BS	PRM
	ITMY	SRM	PR2
	ETMX	SR2	PR3
	ETMY	SR3	
Horizontal stages	9 (IP included)	5 (IP included)	3
Vertical stages	5	3	2
payload type	cryogenic	room temperature	room temperature
	parallel	branch	branch

the change of differential arm length, we apply the highest vibration isolation on them. The Type-A suspesnion has 9 suspended stages including IP pre-isolation stage and 5 GAS filter with 13.5-meter tall. Due to the height of the system, the base of the Type-A suspension sits on the upper floor of the tunnel which is separately excurvated at a higher elevation. The bottom 4 stages are called *cryogenic payload*, containing a sapphire test mass and being operated under ~ 20 K. The cryogenic payload is a parallel chain of the main masses and the reaction masses. The reaction is connected to a cooling bar inside a double-shielded cryostat so as for conductive cooling via heat links. The detailed design of the Type-A suspension will be described in the following sections.

The Type-B suspension is the second largest vibration isolation system used for the BS and the signal recycling mirrors. It has totally 5 suspended stages and contains IP pre-isolation stage as well as the Type-A suspension. The base of the Type-B suspension sits on an external support frame bedded on the ground floor of the tunnel. The payload of the Type-B suspension is a branched chain of the main masses and the reaction masses, which is operated in room temperatures. In the setup of a branched chain, a main mass and its recoil mass are suspended from the next main mass of the upper stage. On the other hand, in the parallel chain such as the Type-A suspension, the main mass and its recoil mass are separately suspended from their own next upper masses.

The Type-Bp suspension is the reduced version of the Type-B suspension, used for the power recycling mirrors. It has 3 suspended stages and 2 GAS filters with the height of 2 m, while the IP pre-isolation stage and the number of GAS filters are omitted For the reason of budgetary constraints. The base of the Type-Bp suspension sits on an inner frame of the vacuum chamber. The absense of the IP stage leads impossibility of adjusting position of suspension point and controlling the fundamental mode of the whole translation. The first problem, the position adjustment of the suspension point, is solved by using a motorized base called *traverser*. The second problem, the control of the whole-chain translational modes, can

Table 3.4. Longitudinal displacement noise requirements at 10 Hz on core optics of the KA-GRA main interferoemter. The stricter value in two operational mode of the interferometer is chosen.

Optics	Displacement noise [m/Hz$^{1/2}$] @ 10 Hz
TM	8×10^{-20}
BS	6×10^{-18}
PRM	1×10^{-15}
PR2, PR3	5×10^{-16}
SRM	5×10^{-18}
SR2, SR3	2×10^{-18}

be overcome with an additional recoil mass applied on the bottom GAS filter. Thus the Type-Bp suspension became totally a branched suspension from the top to the bottom. The design of the payload is shared with that of the Type-B suspension and is operated also in room temperatures.

The basic speficication of these suspension systems are determined by the required seismic attenuation performance, or the required displacement noise under the seismic excitation of the Kamioka underground site. The sensitivity of the KAGRA main interferometer in the observational band is limited by the suspension thermal noise and quantum noise. The goal of the vibration isolation system is to attenuate other noise source contrubutions low enough compared to these fundamental noises. To say quantatively, the requirements of the mirror displacement noise are set as small as 1/10 of the sensitivity curve above 10 Hz. The spectral requirements for the suspensions in each oprational modes of the interfrerometer are plotted in fig. 3.6, and the their values at 10 Hz is sumamrized in table 3.4. In table 3.4, the stricter requirement in two operational modes of the interferometer is listed. Comparing to the smallest requirements on the test masses on the Type-A suspension, allowed displacement noise for the Type-B optics is by 10^1–10^2 larger and for the Type-Bp optics 10^4–10^5 larger. The folding mirrors in the power/signal recycling cavities have by a half smaller requirements than PRM/SRM, since their longitudinal displacement alters the cavity length by twice.

The discussion of the requirements above is not the subject of only longitudinal seimic attenuation but also couplings from other DoFs or other noise sources. We need vibration isolation in vertical direction due to the vertical-to-longitudinal (V-to-L) coupling, as described in the previous chapter. In the case of 3 km separation, the V-to-L coupling caused by the curvature of the Earth is estimated at most 1%. In addition, there are another path of the V-to-L coupling which comes from the inclination of the KAGRA tunnel. KAGRA is not constructed on the exactly horizontal plane for a practical reason; since there are many groundwater spring inside the Kamioka mine, the L-shaped tunnel has been excurvated with

a tilt of 1/300 for drainage. Owing to this inclination, the local vertical motion of the mirrors alters the longitudinal cavity variation at least by 0.3% even without other mechanical couplings. Taking these considerations into account, we assumes the V-to-L coupling in the suspension system as 1% in the following discussions.

Fig. 3.4. Overview of the suspension systems in KAGRA, rendered in a reduced scale. Three types of suspensions, namely Type-A, Type-B, and Type-Bp suspension, are employed for vibration isolation of the core optics.
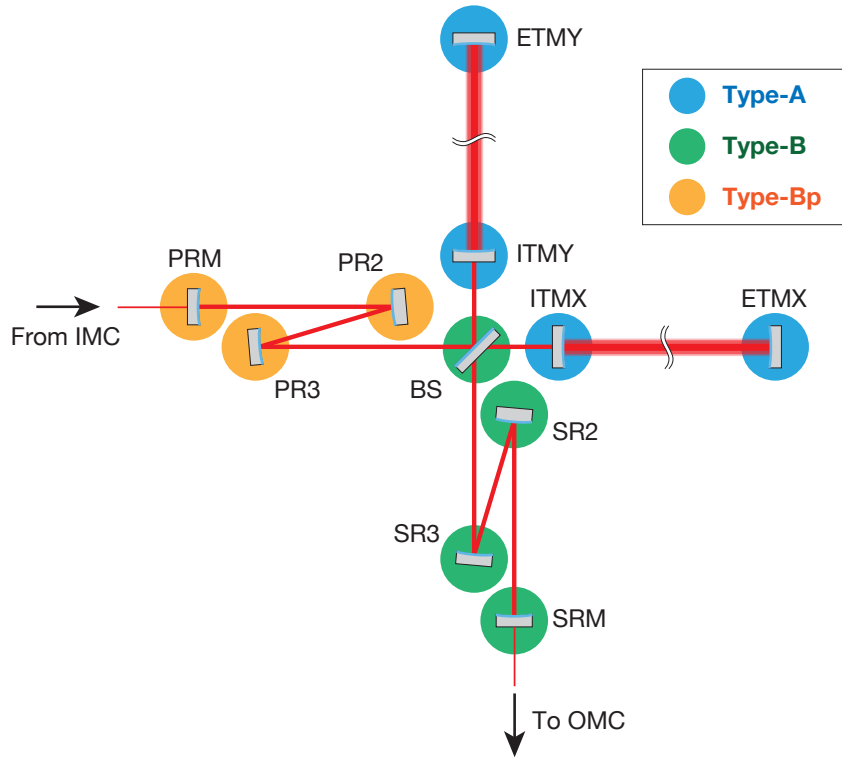
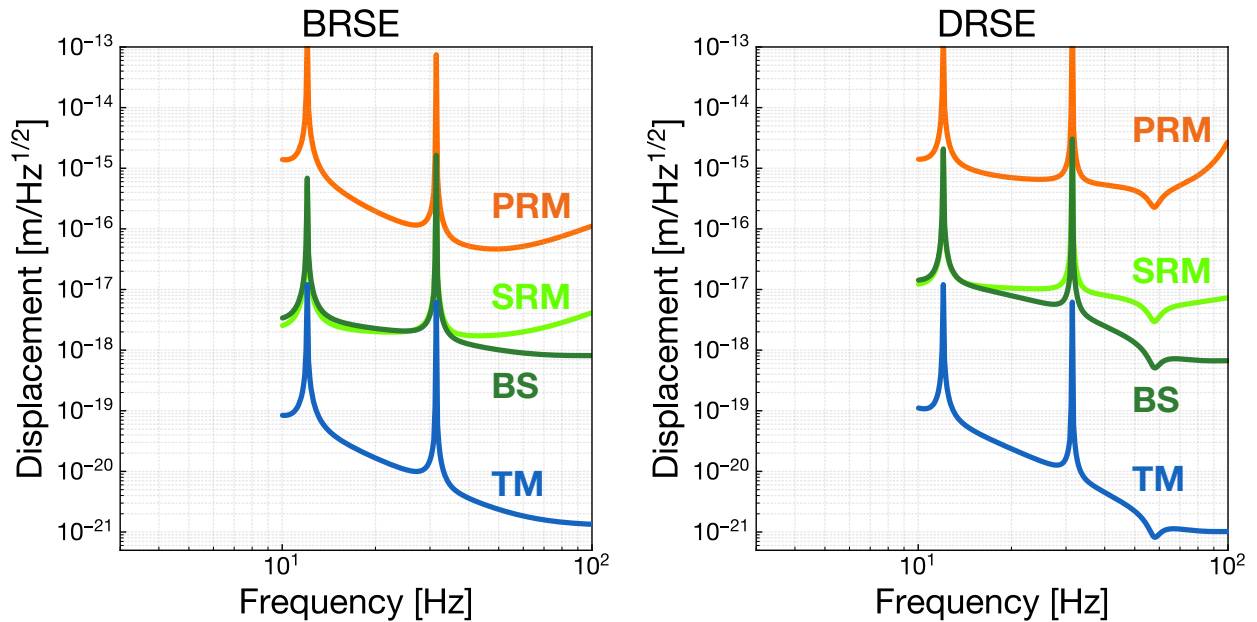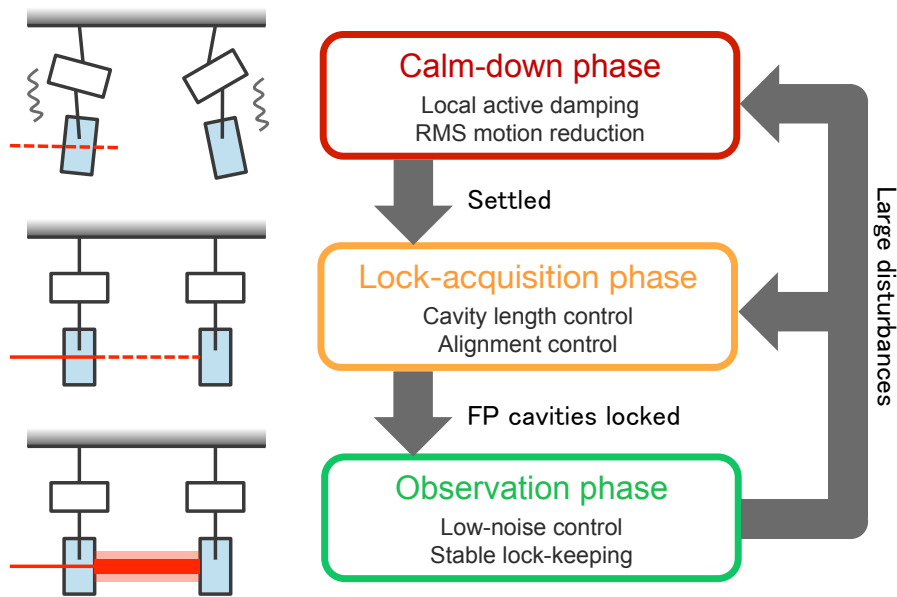**Fig. 3.5.** Configuration of the suspension systems in the KAGRA main interferometer.

Fig. 3.6. Longitudinal displacement noise requirements on core optics of the KAGRA main interferometer in two operational modes.

3.2.1 Control phases

The KAGRA main interferometer is formed by optics individually suspended from their vibration isolation systems. While the optics need to be controlled globally to realize the interferometer operation as the whole, each optic is subject to uncoherent disturbance caused by the seismic noise. Although the suspension systems achieve sufficient seismic attenuation in the frequency band of gravitational wave observation, they also have to suppress the out-of-band mirror fluctuation to construct an global interferometer system. The suspension systems enhance mirror vibration at their mechanical resonances as they stand, which typically have high quality factors, or long decay times in other words.

We govern the suspension systems with active control in order to suppress these low frequency motions of the optics. The active control is based on linear feedback control making use of several kinds of vibration sensors, contactless actuators and digital servo systems. The mechanical resonances can be damped also by passive dampers such as eddy current dampers, which have better stability of working when they once installed. Active control requires careful dedication to the servo design for stable operation, thus in this point it has troublesome complexity. On the other hand, the flexibility of active control, which can easily switch the control strategy depending on the states of the interferometer even after the mechanics of the suspension system is installed, that merit outweighs the difficulties of handling.

In the view point of the suspension systems, the states of the interferometer control can be categorized into three phases, namely calm-down phase, lock acquisition phase, and observation phase. The transition strategy between these phases are visualized in fig. 3.7. The calm-down phase is the state where the optics are swinging with large amplitudes and the interferometer is no longer kept aligned to produce any meaningful signals. In this phase, the suspension systems needs to suppress the vibration of the optics to restore its nominal positions so that the interferometer can start lock acquisition. Here the control gives importance to rather robustness against large disturbances than quiescence of the control noise. Hence, the actual topic in the calm-down phase turns to mode damping of its mechanical resonances. Second, the lock acquisition phase is the state where the interferometer recovers the Fabry-Perot cavities to be locked in their resonant conditions. Since the linear region of the interferometer (PDH) signals is considerably small, the control have to reduce the velocity of the suspended optics small enough to stop it with a limited actuation power. The local control is also required to suppress the angular fluctioation so that the control loop with more sensitive sensors of the interferometer such as the wave front sensors can be engaged. Finally, all the cavities of the interferometer are locked and the control moves to the observation phase where the gravitational wave detection is in operation. The most important point in this phase is less control noise to perform the observation with a better interferometer sensitivity, as well as to keep the mirror displacements and orientations in a certain range for

Fig. 3.7. Phases of the interferometer control in KAGRA. The topics of each control phase is also summarized.

stable operation.

3.2.2   Requirements

The suspension systems need to provide sufficiently stabilized mirrors which residual motion is in the level suitable to the phase of the interferometer control. Thus the requirements on the Type-A suspension are set in each control phase, as summarized in table 3.5. The derivation of each type of requirements are described in the following subsections.

1/e modal decay time

The calm-down phase gives importance to quick recovery of the interferometer signals. However, a large amplitude of the mirror's residual motion, which is usually driven by the mechanical resonances of the suspension system, makes the signals unavailable. Thus the requirement has been set that the 1/e decay time of the mechanical resonances involving in the interferometer operation has to be less than 1 minute. This value is empirically determined so as not to prevent the interferometer from trying lock acquisition for a long time [14].

RMS residual motions for calm down

Other requirements in the calm-down phase are basically intended to settle the excited vibrations into a level in a usual stationary state for the smooth transition to the next lock acquisition phase. Thus the requirements on the RMS displacement (L) and the RMS angles

Table 3.5. Requirements on the vibration isolation and active control of the Type-A suspension. The abbreviations of the suspension's DoFs are as mentioned in section 2.3.

Calm-down phase		
Item	Requirement	For/Determined by
$1/e$ modal decay time	< 1 min	Quick recovery
RMS displacement (L)	$< 50\,\mu$m	Smooth transition to next phase
RMS displacement (T, V)	< 0.1 mm	Miscentering
RMS angle (P, Y)	$< 50\,\mu$m	Smooth transition to next phase
Lock acquisition phase		
Item	Requirement	For/Determined by
RMS velocity (L)	$< 240\,\mu$m/s	Auxiliary laser locking
RMS displacement (T, V)	< 0.1 mm	Miscentering
RMS angle (P, Y)	< 880 nrad	Optical gain degradation $< 5\%$
Observation phase		
Item	Requirement	For/Determined by
Displacement noise (L) @ 10 Hz	$< 8 \times 10^{-20}$ m/Hz$^{1/2}$	Sensitivity
Displacement noise (V) @ 10 Hz	$< 8 \times 10^{-18}$ m/Hz$^{1/2}$	Sensitivity (1% coupling to L)
RMS displacement (T, V)	< 0.1 mm	Miscentering
RMS angle (P, Y)	< 200 nrad	Beam spot fluctuation < 1 mm
DC drift (P, Y)	< 400 nrad/h	Sustainable lock for 1 day left

(P, Y) are set as $50\,\mu$m and $50\,\mu$rad, respectively [14]. The RMS displacement for the other translational DoFs (T, V) are required for another reason which is mentioned shortly later.

RMS velocity for lock acquisition

The arm length stabilization of the Fabry-Perot interferometer is accomplished by using modulated laser beams which is called Pound-Drever-Hall (PDH) technique or frontal modulation technique [8]. The amplitude or phase of the laser is modulated at radio frequencies before entering the main interferometer. By demodulating laser power detected at the photodetector in the proper phase, one can obtain an error signal proportional to the displacement from the working point. Instead of yielding the small linear region of the proportionality of the error signal, the control locked with this scheme can stabilize the laser frequency or the position of the optics in an extreme precision. The width of the linear region is determiend by the finesse of the cavity $\mathcal{F}$ and wavelength of the laser λ with the following equation,

$$\Delta L_{\mathrm{lin}} = \frac{\lambda}{2\mathcal{F}} \ . \tag{3.1}$$

According to the finesse of 1550 for the arm cavities and the wavelength of 1064 nm for the main laser in the KAGRA interferometer, the width of the linear region can be interpreted as the geometrical displacement of the cavity of 3.4×10^{-10} m.

Acquiring the lock of the optical cavity means that the velocity of the cavity length variation has to be zero with respect to the resonant peaks aligned with the interval of the free spectral range. Hence the feedback force needs to stop the suspended mirror while the mirror is passing across the small linear region. However, the test mass actuators will often lack sufficient authority to gain control for nulling the mirror velocity since their design follows the policy of mitigating force noise. For supporting the lock acquisiton of the arm cavities, the KAGRA interferometer adopts so-called *green lock* scheme [13], which introduces an frequency-doubled auxiliary laser with lower finesse for the arm cavities.

The requirement of the RMS velocity in the longitudinal direction has been derived from the condtion that the time scale where the mirror goes across the linear region of the PDH signal is sufficiently longer than the duration of the control bandwidth. Thus the incident velocity of the mirror to acquire the cavity lock should satisfy the following inequality,

$$v_{\mathrm{in}} \lesssim \omega_{\mathrm{b}} \Delta L_{\mathrm{lin}} = \frac{\omega_{\mathrm{b}} \lambda}{2 \mathcal{F}} \ . \tag{3.2}$$

Here ω_{b} denotes the control bandwidth. In the case of Type-A suspension, accomplishment of the green lock can be equivalent to the lock acquisition in the scope of local control. Therefore the incident velocity required for the green lock is calculated as 334 μm/s for $\omega_{\mathrm{b}}/2\pi = 10$ Hz, $\lambda = 532$ nm, and $\mathcal{F} = 50$.

Actual incident velocity of the mirror shows a stochastic behavior because the mirror is driven by random disturbances. Assuming that the velocity of the mirror follows Gaussian distribution, the incident velocity of the optical cavity will have the following probability distribution [11],

$$f(v) = \frac{v}{v_{\mathrm{RMS}}} \exp\left(\frac{v^2}{2v_{\mathrm{RMS}}^2}\right) \ , \tag{3.3}$$

where v_{RMS} denotes the RMS velocity of the cavity length variation. Imposing probability of the lock acquisition higher than 50% in this model, the RMS velocity of the length variation should be suppressed lower than $0.72\,v_{\mathrm{max}}$, where v_{max} is the maximum acceptable velocity. From the discussions above, the requirement on the RMS velocity has been set as 240 μm/s for the Type-A suspension [14].

RMS alignment angles (P, Y)

The mirror rotation in the alignment angles, namely pitch and yaw, causes beam spot fluctuation and spatial mode mismatch in the interferometer. Since the test masses are placed in kilometers separation, even small fluctuations of the mirror angles result in large beam spot

displacements. The requirement in the lock acquisition phase is come from the requirement that the intracavity power doesn't degrade with the loss more than 5% [9], while the one in the observation phase comes from the fact that the beam spot fluctuation at the 3-km distance should be less than 1 mm.

3.3   Mechanical design

The Type-A suspension is a nine-stage pendulum composed of the assembly of IP pre-isolation stage, the chain of GAS filters and the parallelized payload. The 3D drawing of the overall Type-A suspension is shown in fig. 3.8. To overview briefly from the top, the pre-isolation stage consists of the base ring, inverted pendulum legs and the top GAS filter is sitting on the base frame fixed on the ground. The first top stage is supported by three inverted pendulum (IP) legs. The chain of GAS filters starts from the top filter (F0) mounted on the top stage, followed by the succeeding stages named filter 1, 2 and 3, (F1, F2 and F3 in short, respectively,) and then ends with the fifth stage called bottom filter (BF). The stages suspended from the BF is called *cryogenic payload* (also called *payload* or CRYp in short) which begins with the platform (PF). From the PF, two chains of three-stage pendulum, namely test-mass (TM) chain and recoil-mass (RM) chain, is suspended in parallel. The three stages in the TM chain is named the marionette (MN), intermediate mass (IM) and the test mass (TM) which is exactly the sapphire mirror reacts to GWs. The RM chain has mass stages which surround the corresponding mass in the TM chain to apply actuation force isolated from the ground disturbance.

The suspension wires above the PF is made of maraging steel with heat treatment to increase their tensile strength. In the payload, the sapphire fibers are designed for the suspension wire for the TM paying special attention to the thermal conductivity. Other wires in the payload is made of maraging steel or copper beryllium depending on the location to be used.

There is some auxiliary mechanics connected to the suspension chain. One is the magnetic damper (MD), which applies viscous-damping force on the neighboring F1 stage. The magnetic damper is suspended from the top stage with three maraging wires. Another one is the heat link connected from the cooling bar to the marionette-recoil mass for the purpose of quick cooling via conductive heat transfer.
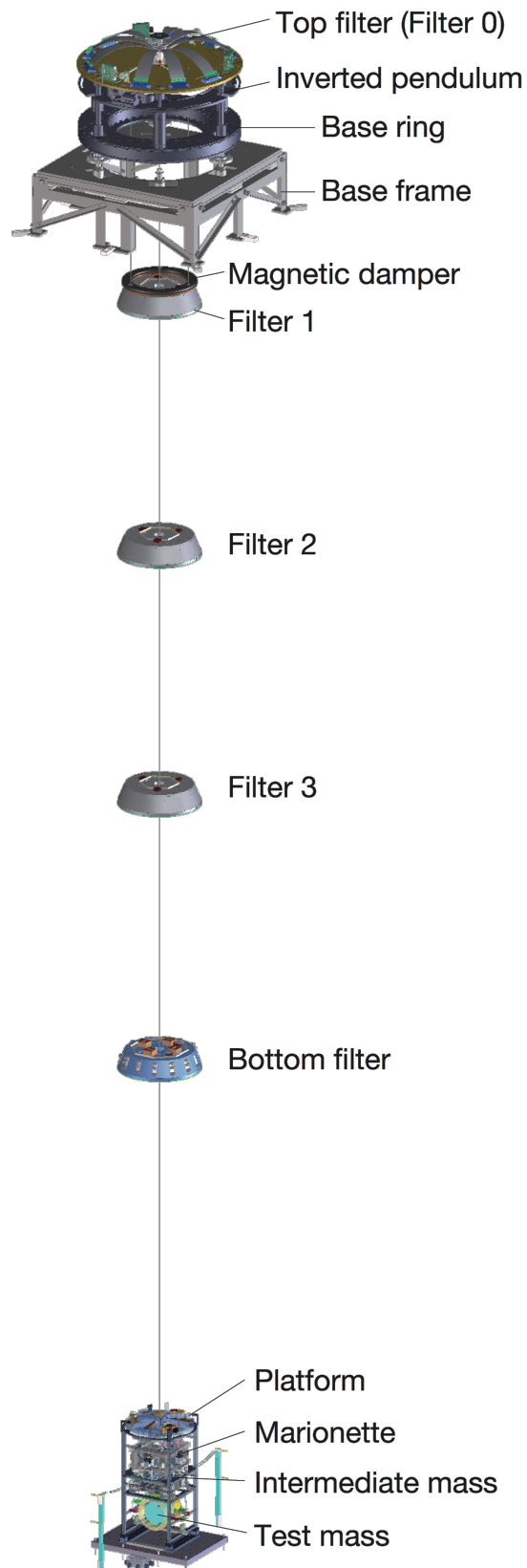
Fig. 3.8. An overview of the Type-A suspension from the top to the bottom.

3.3.1   IP pre-isolation stage

The IP pre-isolation stage, called *pre-isolator*, is a composition of IP legs, a base ring, and the top GAS filter. The function of this stage is to provide the first mechanical resonance below 0.1 Hz for horizontal motion. Since the position of the suspension point for the following chain is determined by the translation of this stage, it also provides controllability of the static position and yaw orientation of the mirror.

An overview drawing of the pre-isolator is shown in fig. 3.9. The top stage is supported by three IP legs in each 120° rotation. Three pillars placed at the mid point of the IP legs connects rigidly the base ring to the reference frame where units of the sensor-actuator device and the lock pillar to fix mechanically the top stage for safety are mounted. On the top stage, the thinner tip of the cantilever blades is connected to the keystone enclosed by the central structure of the top filter. The velocity sensors, commercial products named *geophone L-4C*, packaged in the vacuum canister is mounted on the top stage for the use of inertial sensor independent of the ground disturbance. One of the suspension wires for the main chain is set at the keystone of the top GAS filter, while the other three wires for the magnetic damper are directly set on the ceiling of the top stage.

The detailed dimension of the IP leg is shown in fig. 3.10. The total height of the IP leg is 520 mm, which is much smaller than that used in the Virgo Superattenuator of 6-meter-tall. This IP has the flexure joints at both ends of the hollow cylinder of the leg. The flexure joints are made of maraging steel, a special arroy known for its superior strength and toughness after aging treatment, allowing robust elastic bending beside the top stage displacement. The hollow legs of ~ 0.3 kg each mitigate the saturation of the attenuation performance at higher frequencies. A skirt around the bottom flexure where the counter weights are mounted enables to coincide the center of percussion to the fixing point of the flexure. The saturated attenuation factor which is usually $\sim 10^{-3}$ can be improved to $\lesssim 10^{-4}$ by introducing the counter weights. Each IP stands on the cone bellows supported by in-air screw jacks which enables us to adjust the height of the IP's feet so as the ground plane to be horizontal.

The details of the top GAS filter will be presented in the next subsection, since its structure and functions are similar to those of the standard GAS filter. The sensors and actuators are also explained later.
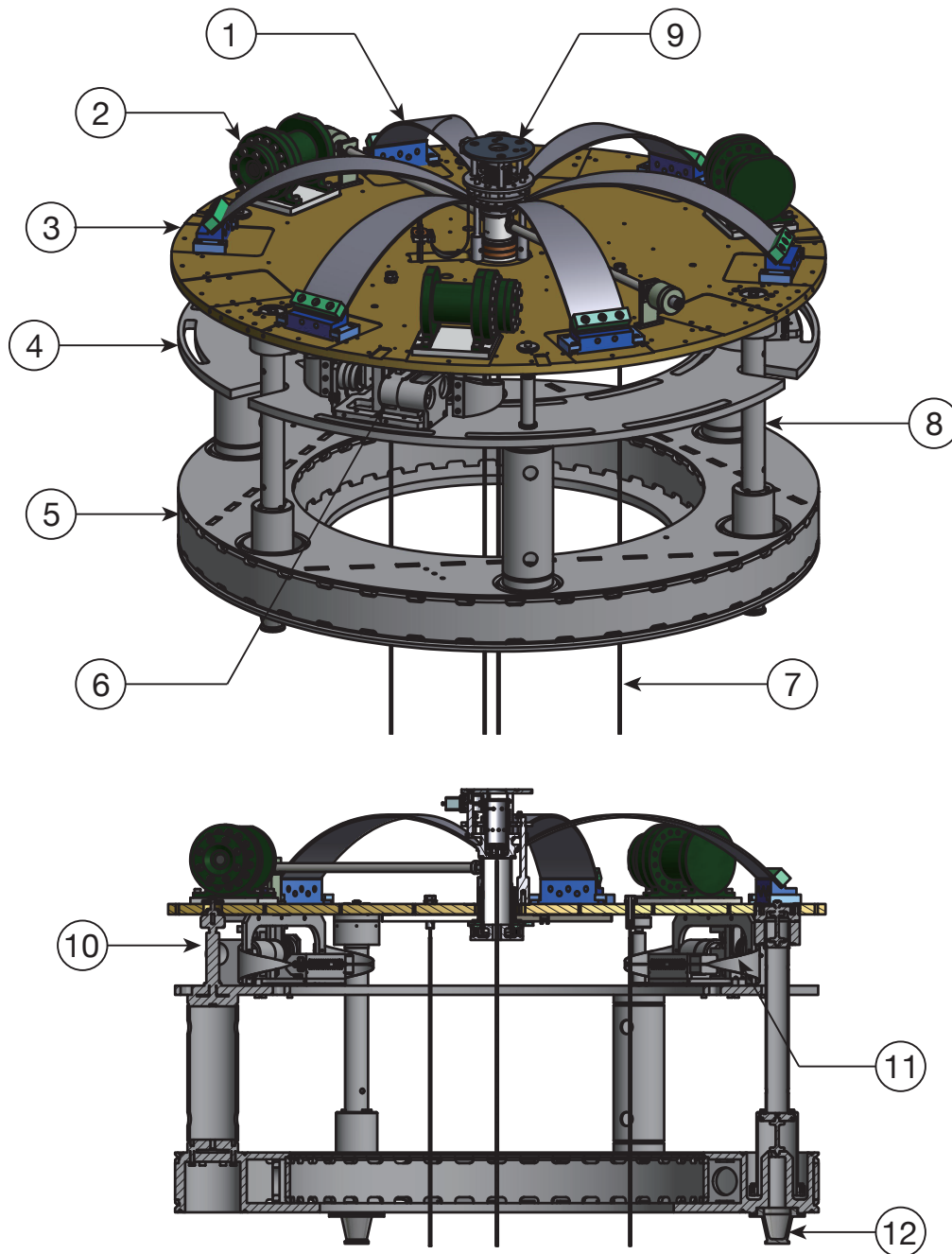
Fig. 3.9. An overview of the pre-isolator (*top*) and its cross-section view (*bottom*). The numbered components are the 1) cantilever blade, 2) geophone capsulated in a vacuum canister, 3) table of the top stage, 4) reference frame ridigly connected to the base ring, 5) base ring, 6) unit of the LVDT and the coil-magnet actuator, 7) suspension wires, 8) IP leg, 9) keystone and the surrounding structure of the top filter, 10) lock pillar for the top stage, 11) motorized blade spring for static position control of the top stage and 12) cup of the cone bollows.

Top stage

Flexure joint

50

φ250

520

φ6.8

50

Counter weight

Base ring

Cone bellows
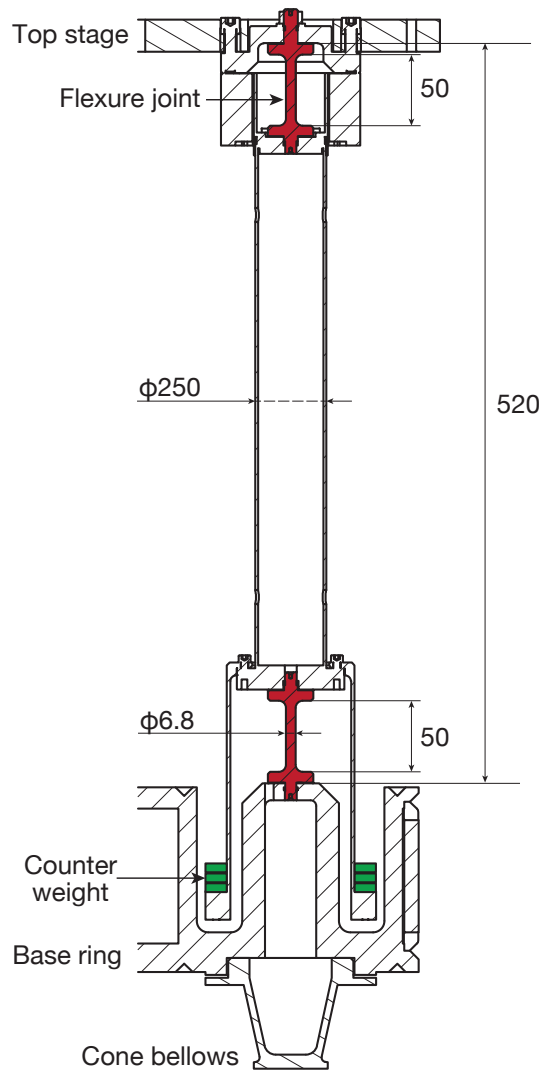
Fig. 3.10. A cross-section view of the IP leg.

3.3.2 GAS filter chain

Type-A suspension has 5 stages of GAS filter chain cascading from the IP pre-isolation stage in order to meet the required seismic attternuation both in horizontal and vertical directions. The first GAS stage, called *top GAS filter*, is implemented directly on the top stage. In the following three stages, we use a GAS filter with more compact design which is called *standard GAS filter*. The last stage of the tower part, called *bottom GAS filter*, has basically same mechanical design as the standard GAS filters have. However the bottom filter is distinguished from the other standard filters because of some functions important as an interface between the tower and the payload.
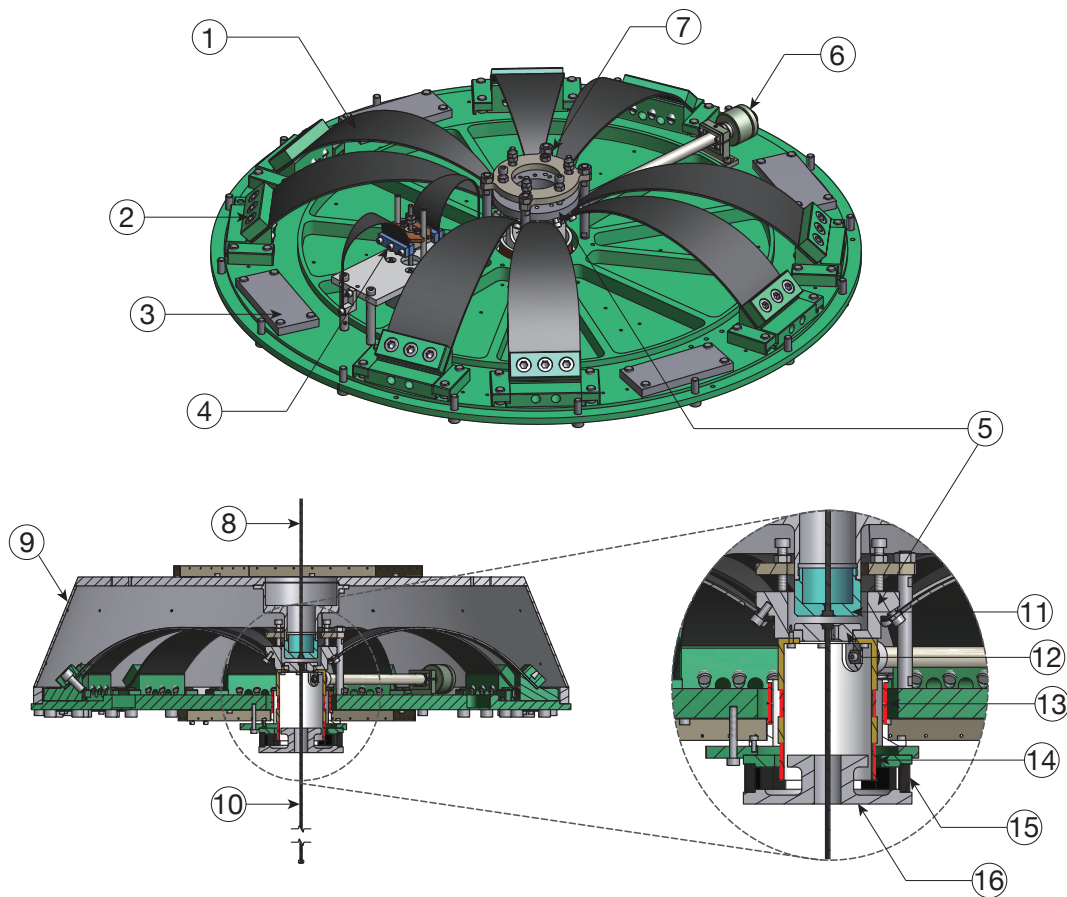
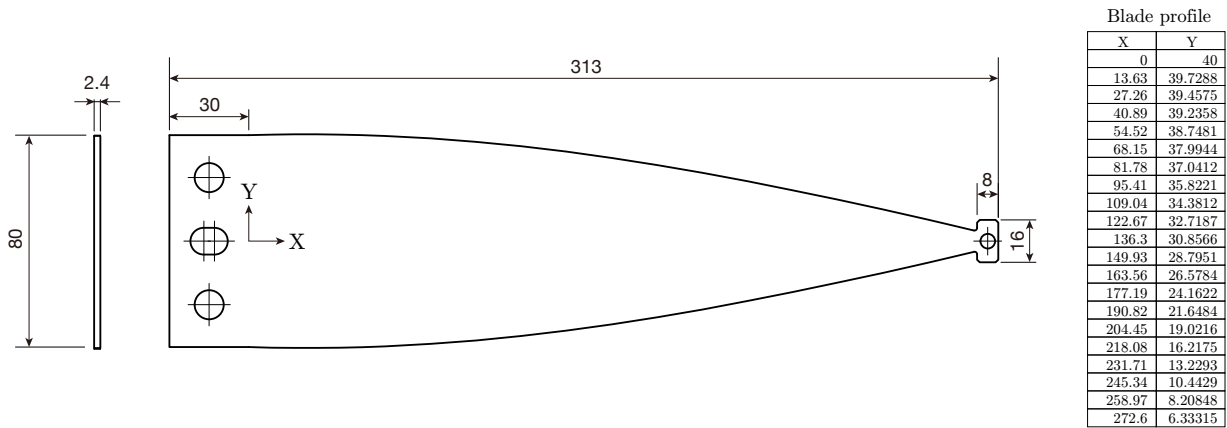**Fig. 3.11.** An overview of the standard GAS filter without the cap (*top*) and its cross-section view with the cap (*bottom*). The numbered components are the 1) cantilever blade, 2) blade clamp, 3) ballast mass, 4) fishing rod, 5) keystone, 6) magic wand, 7) lock screws and nuts, 8) upper suspension wire, 9) filter cap, 10) lower suspension wire, 11) wire receptacle for the upper wire, 12) wire receptacle for the lower wire, 13) coils for LVDT displacement sensor, 14) actuator coil, 15) magnets and 16) iron yoke.

Blade profile	
X	Y
0	40
13.63	39.7288
27.26	39.4575
40.89	39.2358
54.52	38.7481
68.15	37.9944
81.78	37.0412
95.41	35.8221
109.04	34.3812
122.67	32.7187
136.3	30.8566
149.93	28.7951
163.56	26.5784
177.19	24.1622
190.82	21.6484
204.45	19.0216
218.08	16.2175
231.71	13.2293
245.34	10.4429
258.97	8.20848
272.6	6.33315

Fig. 3.12. Dimension of a cantilever blade for the standard GAS filter in Type-A suspension.

The basic structure of a standard GAS filter is implemented on a disk-shaped base plate as shown in fig. 3.11. As the working principle is described in section 2.4.2, quasi-triangular cantilever blades are radially mounted on a base plate. A tip of the bent blades are fixed to the keystone where a suspension wire for the lower stages is hooked. Due to this axisymmetric constraint, the keystone can oscillate only in vertical direction. The wire from the upper stage will be hooked at the center of the cap which shape is like a trancated cone and clamped on the base plate with screws at its radial edge. The wire receptables on both the cap and the keystone is positioned such that the suspension points become closer to its center of mass. In addition, a magic wand is attached on the keystone to compensate the center of percussion effect.

Each cantilever blades are designed to be subject to uniform stress distribution in the compressed situation. All the GAS blades in the KAGRA suspension systems have cosine profiles similar to the standard one, as drawn in fig. 3.12. Note that the surface stress is proportional to the thickness and inverse of the length of the blade, indicating this ratio is kept constant in usual design procedure.

The width, thickness, and number of the GAS blades are adjusted so that its optimal load is equal to the suspended weight from the stage. Intuitively speaking, a stage which supports heavier load requires larger anti-spring effect to achieve the given resonant frequency. Therefore, the top GAS filter has thicker blades and the upper standard GAS filters have a greater number of blades. The blade parameters for each GAS filter are listed in table 3.6.

The vertical oscillation of the keystone is monitored with a LVDT displacement sensor, as well as controlled with a coil-magnet actuator. These apparatuses are implemented coaxially at the bottom of the base plate. For static position adjustment, a motorized blade spring, called *fishing rod*, is attached on the upper part of the keystone. Although the total stiffness of the keystone increases by adding the blade spring of the fishing rod, we confirmed that deterioration of its resonant frequency is less than 10 % increase for all GAS filters.

Table 3.6. Blade parameters of the GAS filter in Type-A suspension.

Stage	Thickness [mm]	Base width [mm]	# of blades
Filter 0 (top)	5.0	125	6
Filter 1 (standard)	2.4	80	12
Filter 2 (standard)	2.4	80	10
Filter 3 (standard)	2.4	80	8
Bottom filter	2.4	80	5
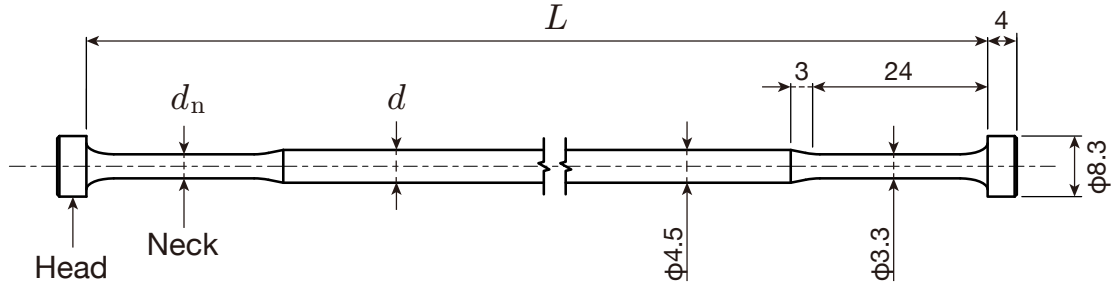
Fig. 3.13. Design of the maraging wire.

3.3.3 Maraging wire

The main chain from the top stage to the platform in the cryogenic payload is connected with single maraging wires. The maraging wire is capable of suspending heavy payload with enough mechanical stability.

Maraging steel, the material used for not only the suspension wires but also the blades in the GAS filters and flexure joints in the IP legs, is an low-carbon-content ($\lesssim 0.03\%$) iron alloy with nickel, cobalt, and molybdenum. Through martensitic transformation and age hardening [1], maraging steel acquires ultimate tensile strength of $\gtrsim 1600$ MPa. In the use of suspension systems in gravitational wave detectors, it is known as its low mechanical shot noise induced by microscopic creeps under stress, which is accumulation of quantized yielding process such as movement of dislocations and diffusion of vacancies in crystalline structure, resulting long-term plastic deformation even below the yield stress of the material.

The dimension of the wire is not uniform; it has thicker heads at both ends which will be hooked on the wire receptacle at the keystone or the cap, also has thinner neck over a few centimeters, as shown in fig. 3.13.

The neck part with smaller diameter is machined in order to reduce the effective bending offset from the suspension point. In an ideal rigid body model with massless wire connections, the wire bends exactly at the clamping point on the body. However, in reality the wire has

---

[1] Actually, the name of "maraging steel" is a compound of *martensitic* and *aging*.

bending elasticity and thus bends at an offset point from the clamping point with a finite radius of curvature. This effect, sometimes reffered to as *bending point effect*, will deteriorate the seismic atternuation performance because the effective length of the pendulum become shortened, having higher resonant resonant frequency. The offset of the bending point Δ is calculated through the following relationship.

$$\Delta = \sqrt{\frac{EI}{T}} \tag{3.4}$$

Here E is the Young modulus (modulus of longitudinal elasticity), I is the second moment of area, and T is the tension on the wire. The wire with diameter of d has second moment of area of $I = \pi d^4/64$. In the case of the suspension systems in KAGRA, the offset of the bending point stays in the scale of mm–cm, much smaller than that of the wire length $L \sim$ a few meters, therefore the bending point effect can be negligible.

The diameter of the neck is designed such that the maximum Mises stress under loading is below the yield stress of the maraging steel with a safety factor of 2. The fillet part between the head and neck is machined to be an elliptic dimension which is optimized to mitigate stress concentration.

The chain of single-wire suspensions behaves also as a torsion pendulum with very low resonant frequency in general. The torsional oscillation is driven by the stiffness of the wire independently of the gravitational restoring force. The spring constant of the torsional motion is written as,

$$k_{\mathrm{tor}} = G \frac{\pi d^4}{32L} \ , \tag{3.5}$$

where G is the shear modulus, the factor $\pi d^4/32$ originates from the polar moment of inertia of area. The torsional stiffness is calculated as an integration over the wire length, while the bending point offset described above is determined by the diamemeters in a few centimeters just from its clamping point. Thus the maraging wire has smaller thickness at the both ends and larger thickness in the middle. However, even with the thickness treatment, the single-wire suspension chain still possesses low-frequency torsional modes (< 0.1 Hz) that leads large angular fluctuation of the mirror in yaw and misaligns interferometer configuration. The Type-A suspension overcomes this torional-mode problem with implementation of passive and active dampers, which will be explained in the following subsections.

3.3.4   Magnetic damper

As discussed in the previous subsection, a single-wire suspension chain behaves as a torsion pendulum with a very low resonant frequency ($\lesssim 0.1$ Hz). This torsional oscillation, when once excited, lasts for a long time due to its high quality factor originating from the

intrinsic mechanical loss of the wire. For quick recovery of the inteferometer operation, we have to decrease the torsional motions corresponding to the horizontal alignment of the mirror,

The magnetic damper is an passive damping mechanism using eddy currents. An eddy current damper consists of parmanent magnets fixed on the reference side and conductive plates attached on the oscillator side to be damped. When a conductive object feels alternation of neaby magnetic fields, it generates eddy currents on its surface so as to oppose the time-varying magnetic fields. It results to produce a breaking force onto the oscillator (or breaking torque for rotational oscillation).

The conceptual design of the magnetic damper in the KAGRA suspensions is a ring with arrayed parmanent magnets suspended from the pre-isolation stage by three wires and placed just above the first standard GAS filter (F1). The magnets are arranged such that the overall magnetic dipole moment cancels out. The damper ring faces copper plates attached on the top of the F1 stage, with a gap of ~ 5 mm.

Notwithstanding, the signle magnetic damper is not adequate to damp the torsion mode of the long chain of the Type-A suspension, since the magnetic damper can apply a breaking torque only onto the F1 stage which is close to the node of the open-ended fundamental torsion mode. To damp an specific natural mode which mode shape is known, it is effective to implement a damper at the position of its antinode where the mode has large amplitude. Thus the second torsion-mode-damping mechanism is implemented on the bottom filter in the Type-A suspension, as described in the next subsection.

3.3.5 Bottom filter

Bottom filter is the last GAS stage in the tower part of the Type-A suspension. Although the basic mechanical design is same as that of the standard GAS filter, the bottom filter is distinguished from them due to some additional functions useful to interface the upper stages with the payload assembly, not only in Type-A suspension but also in other types of the suspension systems.

One of the important role of the bottom filter is providing controllability at the lower point of the susupension with comparably large actuation range. The bottom filter is equipped with sensor-actuator-unified devices named as *BF LVDT* (sometimes also reffered to as BF damper) for 6 DoFs measurability and controllability of the bottom filter motion with respect to the ground (exactly speaking, the ground means the security structure or the vacuum chamber which surrounds the suspension chain and fixed onto the ground). We can implement a larger actuation range on the bottom filter than the payload stages owing to less anxiety of the actuator-induced noise transmitted to the bottom optic stage.

The BF LVDT allows us to actively damp the torsional motion of the single-wire suspen-

sion. In most cases, the torsional oscillation is driven by the translational seismic motions coupled through some paths such as imperfect centering of the suspension point due to inaccurate assemblings. Thereby, since its low-frequency mechanical resonances provides sufficient atternuation in the yaw direction, the torsional motions are less problematic in terms of displacement noise which contaminates the interferometer sensitivity. However, when the yaw motion is once excited by somewhat of kicks, it takes long time (typically > 1000 seconds) to decay, leading misalignment of the mirror and decrease of the duty cycle of the interferometer. Since the position of the bottom filter is far from the node of the fundamental yaw mode (the suspension point on the top GAS filter), the actuation on the bottom filter can apply effective damping. One concern remains is that the bottom filter is in contrast close to the node of the second yaw mode and thus less controllable in the Type-A suspension. We should treat this problem with some tricky way of a control strategy.

Other than the BF LVDT, the bottom filter has some additional functions. In Type-B and Type-Bp suspension, the next stages, namely intermediate mass (IM) and intermediate recoil mass (IRM), are suspended divergingly from the bottom filter. The 6-DoFs relative position of the IM with respect to the IRM is monitored and actuated in order to provide a further controllability of the mirror's displacement and alignment. Since the IM is connected with a single wire while the IRM is with three wires, a tilt of the bottom filter turns into a relative translation of the IM and IRM. In order to adjust the tilt, the bottom filter is equipped with a motorized weight on the cap. In addition, the static yaw position can be adjusted with a picomotor, implemented on the keystone of the bottom filter. Thus the bottom filter is not only one of the GAS filter but also an interface providing functions to adjust the payload conditions.

3.3.6   Cryogenic payload

The suspension systems in KAGRA have bottom stages called *payload* which includes the core optics. The one in the Type-A suspension is called *cryogenic payload* cooled down to operate at cryogenic temperatures. Since the detailed design and characteristics (both vibratory and thermal) will be presented in [**Miyamoto2019**] as a main topic, here we don't go beyond brief description of the basic information of the cryogenic payload.

The cryogenic payload consists of 4 stages with a parallelized pair of chains. A computed-aided drawing of the cryogenic payload is shown in fig. 3.14. A disc-shaped stage called *platform* (PF) is suspended from the bottom filter with a 3.3-meter-long single maraging wire. There are two chains suspended from the PF in parallel, namely TM-chain and RM-chain. The first stage of the TM-chain is *marionette* (MN), a cross-shaped mass supported at a point close to its center of mass with a single maraging wire in order to have low stiffnesses in its rotational DoFs. The next *intermediate mass* (IM) is the penultimate stage
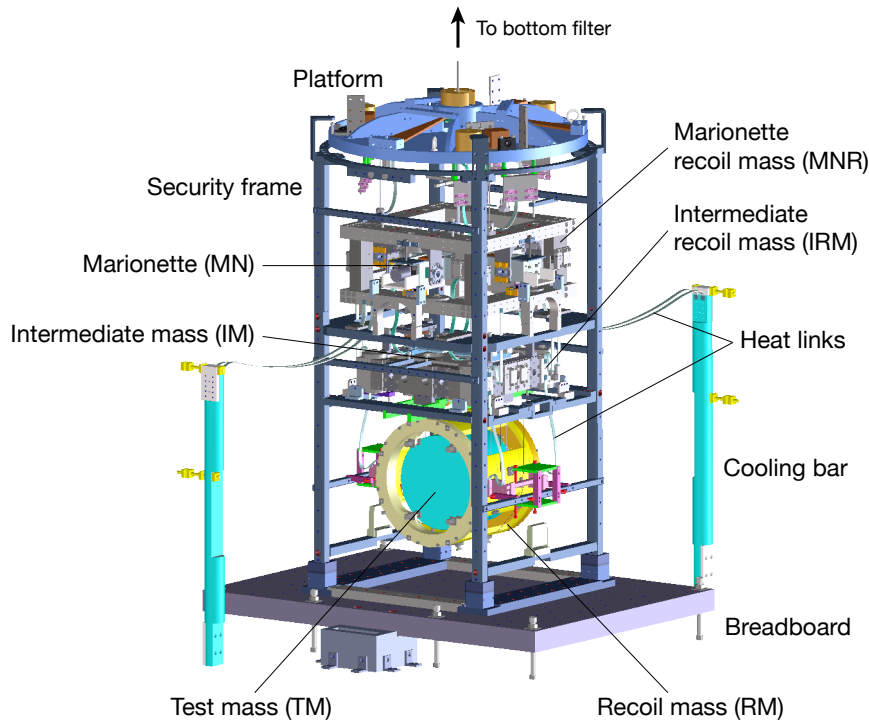
Fig. 3.14. An overview of the cryogenic payload.

suspended from the 4 wires made of beryllium copper. Finally the sapphire test mass (TM) is suspended with four sapphire fibers (35 cm long and 1.6 mm diameter), each of which is hooked on a sapphire blade springs attached on the IM. The use of same material in the TM substrate and the fiber improves thermal conductivity of the assembled system. These bottom three stages are accompanied with their reaction masses, providing controllability of relative position and alignment of the test mass independent of the seismic disturbances. There are permanent magnets on the TM-chain masses and coils on the RM-chain masses functioning as coil-magnet actuators to control each six differential DoFs of the MN-MNR and IM-IMR position, and three differential DoFs (namely longitudinal, pitch, and yaw) of the TM-RM position. Beside that, cryogenic photo-reflective sensors are additionally implemented in the configuration coincident with the coil-magnet actuators to produce local displacement of the TM-chain masses with respect to the RM-chain frames. In addition, static alignment control with respect to the ground structure can be performed with local angular sensors called optical levers.

The cooling of the cryogenic payload is based on the two paths of heat transfer, radiation cooling and conduction cooling. The whole of the cryogenic payload is housed in a double-layered cryostat which is formed by a 8 K inner shield and 80 K outer shield. The surfaces of the cryostat, payload, and the security frame are treated with black coating for the efficient radiation cooling. In addition, the stages of the cryogenic payload are connected
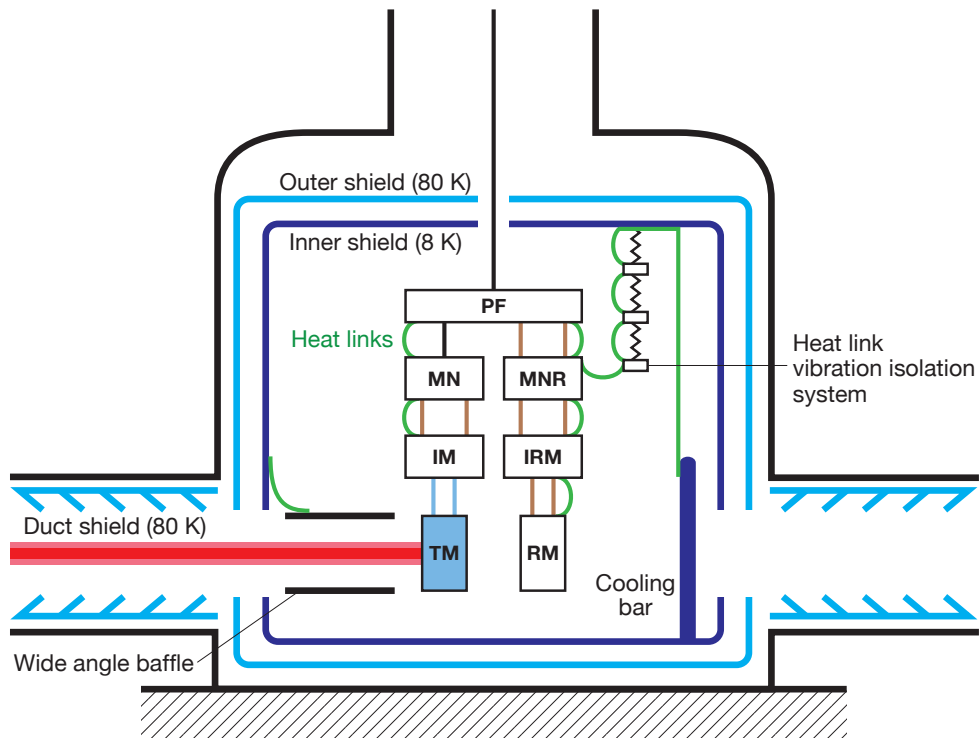
Fig. 3.15. Schematic diagram of the cooling system around the cryogenic payload.

each other with high purity aluminum cables, called *heat links*, for conduction cooling. The absorbed heat on the test mass flows to upper stages and is finally extracted to the cryostat structure through the heat links and cooling bars. Since this mechanical conduction path could reintroduce additional vibrational disturbances to the isolated stages, a three-stage vibration isolation system is implemeted on the cryostat to relay the heat links attached on the MNR. These cryogenic instruments are put under refridgeration with four units of pulse-tube cryocoolers. The cryocoolers have a doubled vibraiton reduction stages whose first stage is connected to the 80 K outer shield and whose second stage is conencted to the payload-cooling system and the 8 K inner shield. Although the shields of the cryostat have bore holes in front of the test mass so that the laser beam goes through, the holes can threanten the cooling time and attainable lowest temperature of the test mass by allowing intrusion of 300 K radiation from the room-temperature vacuum ducts. Therefore, 80 K duct shields are implemented inside the neighboring vaccum ducts to reduce the solid angle of the incoming 300 K radiation.
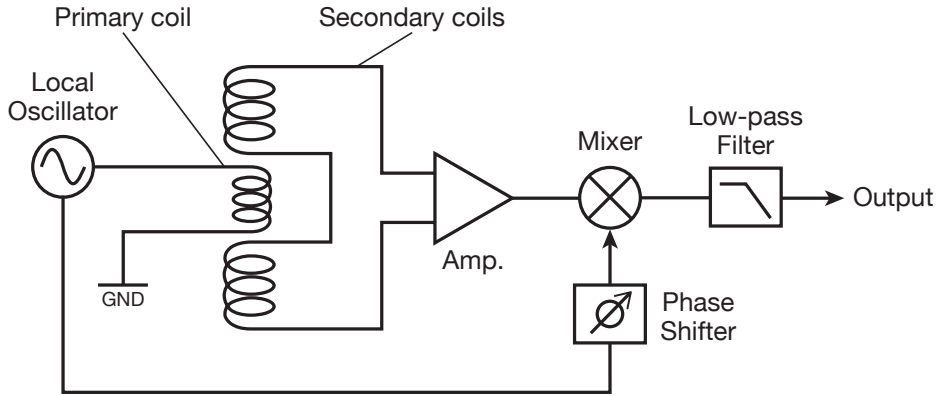
Fig. 3.16. Scheme of the LVDT position sensor

3.4 Sensors and actuators

3.4.1 Linear Variable Differential Transducer (LVDT)

The Linear Variable Differential Transducer (LVDT) is a relative displacement sensor using modulated magnetic field between inductively coupled coils [15]. Fig. 3.16 shows the schematics of LVDT position sensing. The two kinds of coils, the primary coil and the secondary coils, are set coaxially aligned. One sends sinusoidal modulation signals of ~ 10 kHz to the primary coil which produces oscillating magnetic field around it. Then the secondary coils in vicinity sense the variation of the magnetic field and generate induced voltages. Since the two secondary coils are identical but counter-wound to each other, the induced voltage is canceled when the primary coil is placed at the center of the secondary coils. Thus, the primary coil shifts from the center, the mutual inductance changes and the differential induced voltages appear as net voltages at the subsequent readout. The net differential voltage is amplified and sent to the mixer which demodulates the oscillating voltage to obtain low-frequency ($\lesssim 100$ Hz) signals of the displacement of the primary coil.

One feature of the LVDT is good linear response to the displacement over large dynamic range in axial direction. Our implementation has centimeters of its dynamic range with resolution of sub-micrometers, specific values of which depend on the applications. The KAGRA suspension systems have two types of LVDTs: a standard one used in the IP and GAS filters and a dedicated one used in the BF. As for the latter, it is designed that the secondary coils of the LVDT is shared by actuator coil.
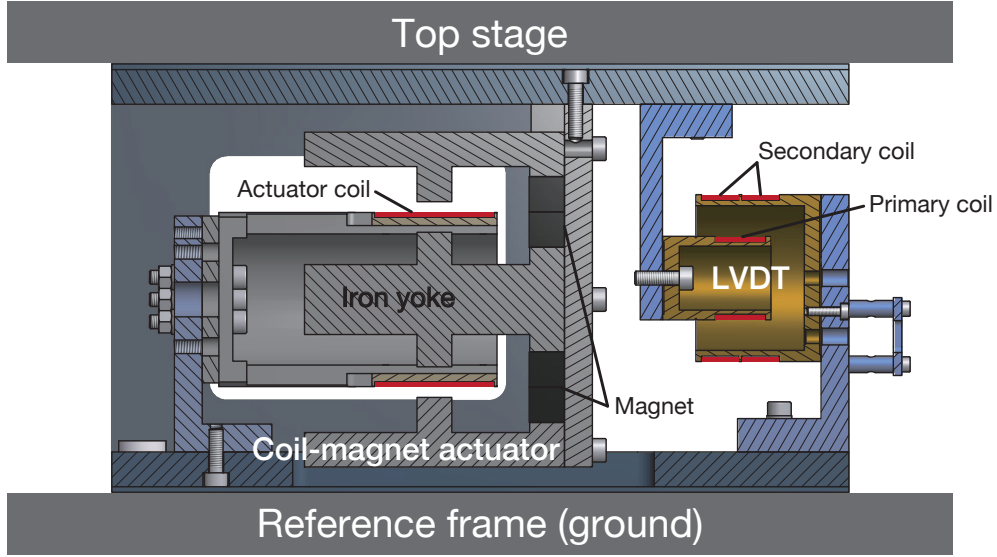
Fig. 3.17. Cross section of the unit of LVDT and coil-magnet actuator mounted on the Pre-isolator.

3.4.2 Geophone

A geophone L-4C is a commercial instrument of high-sensitivity seismometer manufactured by Sercel. The geophone outputs voltages proportional to velocity of its proof mass with respect to the housing. The proof mass with the weight of 1 kg is softly suspended with a spring and a damper with its resonant frequency of ~ 1 Hz. A coil wound on the proof mass generates voltages induced by a parmanent magnet attached on the housing. The geophone is a passive instrument; it doesn't need any controls for the internal oscillator unlike the accelerometers used in TAMA-SAS, that benefits in simple procedure of installation and maintainance.

The geophone has a 2nd-order high-pass frequency response below its resonant frequency. The frequency response of the geophone is written as

$$H_{\mathrm{geo}}(\omega) = \frac{G_{\mathrm{e}}\,\omega^2}{\omega_0^2 + 2i\eta\omega_0\omega - \omega^2} \ , \tag{3.6}$$

where G_{e} is the generator constant, η is the damping coefficient, ω and ω_0 are the angular frequency and angular resonant frequency, respectively. The conversion efficiency of the frame velocity to the output voltage is also plotted in fig. 3.18. While the geophone has a flat response above the resonant frequency of 1 Hz, it shows frequency dependence proportional to f^2 at lower frequenies. The nominal parameters of the geophone is specified in table 3.7.

The output voltage from the geophone is amplified by a pre-amplifier circuit for better S/N ratio before being sent to the control system. The pre-amplifier circuit used in KAGRA
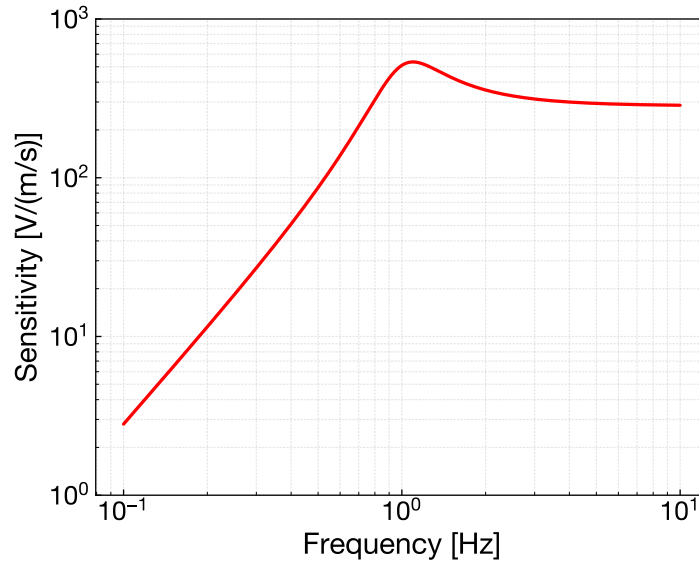
Fig. 3.18. Nominal frequency response of the L-4C geophone to ground velocity

Table 3.7. Nominal parameters of the geophone L-4C

Item	Value
Generator constant	276.8 V/(m/s)
Proof mass weight	1 kg
Resonant frequency	1 Hz
Damping coefficient	0.28
Coil resistance	5,500 Ω

suspension systems is designed in NIKHEF for the advanced Virgo. The first amplification stage with an operational amplifier CS3002, chosen due to its low voltage noise feature, magnifies the signals by a factor of 374.5, then the second amplification stage gains the amplitude by 2.5 times larger with converting the singals into differential outputs. Thus, the pre-amplifier applies totally 53.5 dB amplification in the equivalent differential signals.

On the other hand, the pre-amplifier also provides dominant noises limiting the sensitivity of the geophone. A measured voltage noise spectrum with a breakdown into several noise sources' contributions are presented in [14]. The measurement indicates that the pre-amplifier noise is determined by Johnson noise at high frequencies (> 0.3 Hz), which is the thermal noise from the resistance, and current noise at low frequencies (< 0.3 Hz) which comes from the operational amplifier.

Although the nominal parameters are given as summarized in table 3.7, the individual values of those parameters are calibrated by a simultaneous seismic vibration measurement with multiple types of seismometers. We uses additionally two units of Trillium Compact and one unit of Trillium 120QA seismometers produced by Nanometrics Inc., which are em-

ployed in KAGRA as environmental seismic monitors of the underground site. The Trillium seismometer series have flat response in broadband region (0.01–10 Hz) and therefore exceed in simplicity of the calibration procedure.

The geophone and the pre-amplifier requires in-air operation, while the whole of the suspension system is put in the vacuum environment. To secure the vacuum compatibility for the apparatus, we sealed them in vacuum pods made of stainless steel and kept insides at atmospheric pressure. Air leakage from the vacuum pods were confirmed as negligible at least for several months in the prototype test of the Type-B suspension in NAOJ [14]. The relative position of the geophone inside the vacuum pod is fixed with rubber rings in order to prevent rattling on the internal surface which will produce unwanted impulses in the readout signals. The damping effect of these rubber rings have been checked as negligible, indicating that the housing of the geophone and the vacuum pod can be regarded in a body.

3.4.3   Coil-magnet actuator

Suspension control in gravitational wave detectors requires vacuum-compatible and non-contacting actuators to apply force on the suspended bodies. A coil-magnet actuator is one instrumentation to meet such demands. One unit of the coil-magnet actuator consists of permanent dipole magnets and solenoid coils. It utilizes force of electromagnetism generated by the interaction between the static field of the permanent magnets and current sent to the coils.

The coil-magnet actuators used in the suspension systems can be classified into two types according to their working principle; voice-coil type and coaxial moving-magnet type. The voice-coil type actuator is a common implementation in audio speakers where the current in the coils feels Lorentz force by moving in a static magnetic field [16]. The lead wires of the coil are placed in a uniform magnetic field from the magnets shaped by high permeability iron yokes. Since the permanent magnets are fixed on the reference frame, the Lorentz force received by the current become actuation of on the coil itself, or the suspended body which the coil is attached on. On the other hand, the coaxial moving-magnet type actuator has the permanent magnets and solenoid coils coaxially aligned to each other. The induced magnetic field of the coil attached on the reference frame applies electromagnetic force on the permanent magnets glued on the suspended body. To mitigate dependence of the actuation force on the magnets' position, the magnets should be placed in the enough uniform region of the induced magnetic field of the coil. Any types of these actuators implemented in the KAGRA suspensions are designed so that they have sufficient linear region and dynamic range of the actuation force. In the case of Type-A suspension, the actuators on the IP and GAS are the voice-coil type and ones on the BF and payload are the coaxial type.

The design of actuators always involves a trade off between maximum actuation power

Table 3.8. Specification of the KAGRA coil drivers and assignment in the Type-A suspension [12]. The output resistances don't include the coil's impedance. The maximum current with the low power coil driver is 1.3 mA for the TM and 1.7 mA for the IM.

	OpAmp	Output resistance	Max current	Implemented on
Low power	AD8671	7.8 kΩ	1.3 mA or 1.7 mA	TM, IM
Modified low power	AD8671	1.4 kΩ	9.5 mA	MN
High power	OPA548	80 Ω	0.12 A	IP, GAS, BF

and force noise. An actuator with large actuation force will generate unwanted force noise driven by even a small amount of electric fluctuation. In the case of suspension systems, the actuators located closer to the optics have larger impact on the sensitivity of the interferometer. Considering the situation, we use three types of coil drivers to compromise the requirements on the available actuation range and force noise, as specified in table 3.8. These coil drivers have different operational amplifier of the current source and output resistance. As described in the following section, the actuation current sent to the coil is controlled with a digital system. The digital system has digital-to-analog converters (DACs) with an output range of ± 10 V which limits the maximum actuation current to the coils and the coil driver doesn't determine the available current.

3.5 Digital signal processing

There are hundreds of thousands of channels to be managed for the interferometer operation of KAGRA, even though the signals essential to the GW detection correspond to a few channels. Moreover, achieving the outstanding sensitivity to observe GW signals needs systematic noise hunting where the people must survey an enormous number of channels to localize the sensitivity-limiting noise source. Even if we narrow our scope into a single suspension system, it has tens of signals to be processed, some of which are closed locally while some are interconnected with other suspension or control subsystem. These situations are complicated enough to motivate us to govern the whole observatory with computational instrumentation.

Digital control with computational machines provides easy accessibility and operability of the huge system of the gravitational wave telescope. Use of digital control system enables us to acquire the following features.

- Real-time remote control of the instruments

- Easy management of the multiple degrees-of-freedom control

- Low noise control by quantization

Table 3.9. Specification of the KAGRA digital system.

Item	Value
Samping rate	2048 Hz (decimated from 65536 Hz)
Through delay	80 μs
ADC/DAC resolution	16 bit ($2^{16} = 65536$ digital counts)
ADC voltage range	± 10 V (1 count = 3.052×10^{-4} V)
DAC voltage range	± 10 V (1 count = 3.052×10^{-4} V)
ADC noise level	3 μV/Hz$^{1/2}$ (> 10 Hz)
DAC noise level	2 μV/Hz$^{1/2}$ (> 10 Hz)
Number of ADC channels	32 ch. differential inputs / 1 ADC board
Number of DAC channels	16 ch. differential outputs / 1 DAC board

- Data acquisition infrastructure

- Automated operation of the interferometer

The detailed specification of the KAGRA digital control system is summarized in [14].

Chapter 4

Control design

4.1 System modeling

Modeling of the suspension system is an important part of understanding its dynamic characteristics and also a powerful tool to design the control strategies. Here we start from the 3-dimensional rigid-body modeling. It means that internal dynamics of the suspended mass is ignored and we concentrate on the modes only associated with the coupled multi-degrees-of-freedom vibration of the rigid components. This assumption is generally accurate when studying the low-frequency ($\lesssim 10\,\mathrm{Hz}$) dynamics of such a mechanical system. Moreover, it is also combined to the frequency region of our interest where the control will be applied. As a simple model we consider, the problem of the control design can be solved in lower complexity.

Control problems of the suspension systems are addressed by the framework of linear control theory. Although the full dynamics of the mechanical oscillator includes non-linearity in general, the linear approximation stays valid since the suspension system will be operated in a small region around its equilibrium point. We have another naive reason to restrict the system to be linear that is to utilize well-studied tools of linear control theory developed in the long history of the control engineering. Modeling and control problems of a non-linear system make things much complicated, despite the fact that we are hardly interested in such a non-linear behavior.

4.1.1 Formulation of 3D rigid-body dynamics

In this study, a toolkit of 3D rigid-body modeling coded in Mathematica® is used which is initially developed by M. Barton for the LIGO suspensions and packaged into a GUI software by T. Sekiguchi. Here the concept of the 3D rigid-body modeling is briefly described.

The formulation of dynamic characteristics of multi-DoFs mechanical oscillator is based on the linearized equation of motion. Expressing a set of positions and velocities of the system

(= component masses) respectively as $\boldsymbol{x}$ and $\dot{\boldsymbol{x}}$, the derivation of the euation of motion has the followins steps.

1. Calculate the potential energy $U(\boldsymbol{x})$, dissipation function $R(\boldsymbol{x}, \dot{\boldsymbol{x}})$ and kinetic energy $K(\boldsymbol{x}, \dot{\boldsymbol{x}})$ of the sustem.

2. Minimize the potential energy to find the equilibrium point $\boldsymbol{x}_{\mathrm{eq}}$.

3. Differentiate the potential energy with respect to pairs of the coordinate of the equilibrium point to derive the *stiffness matrix* $\boldsymbol{K}$,

$$K_{ij} = \left. \frac{\partial^2 U(\boldsymbol{x})}{\partial x_i \partial x_j} \right|_{\boldsymbol{x}=\boldsymbol{x}_{\mathrm{eq}}} \tag{4.1}$$

4. In a same manner, differentiate the dissipation function and the kinetic energy with respect to pairs of the coordinate velocity at equilibrium to derive the *damping matrix* $\boldsymbol{G}$ and the *mass matrix* $\boldsymbol{M}$,

$$G_{ij} = \left. \frac{\partial^2 R(\boldsymbol{x}, \dot{\boldsymbol{x}})}{\partial x_i \partial x_j} \right|_{\boldsymbol{x}=\boldsymbol{x}_{\mathrm{eq}}} \tag{4.2}$$

$$M_{ij} = \left. \frac{\partial^2 T(\boldsymbol{x}, \dot{\boldsymbol{x}})}{\partial x_i \partial x_j} \right|_{\boldsymbol{x}=\boldsymbol{x}_{\mathrm{eq}}} \tag{4.3}$$

5. Finally the linearized equation of motion is written with the derived matrices as

$$\boldsymbol{M}\ddot{\boldsymbol{x}} + \boldsymbol{G}\dot{\boldsymbol{x}} + \boldsymbol{K}(\boldsymbol{x} - \boldsymbol{x}_{\mathrm{eq}}) = \boldsymbol{0}\,. \tag{4.4}$$

In this formulation, each suspended body has motions in 6 DoFs except for the IP stage which has only horizontal 3 DoFs, namely longitudinal, transverse and yaw. The GAS is treated as an 1-dimensional vertical spring, taking into account the saturation of attenuation performance caused by the imperfect cancellation of the center-of-percussion effect. We regard the suspension wires as massless springs with torsional elasticity and load elongation, neglecting their violin modes. To treat dissipation due to the internal friction of the elasric material, the spring constants of the vertical springs and wires have imaginary parts representing finite loss angle which is assumed to be constant over all frequency region (equivalent to structural damping process).

4.1.2   State-space representation

The techniques reffered in the control theory can be applied to systems whose time evolution can be described by a series of linear, time-invariant [1], first-order ordinary differential

---

[1] Here "time-invariant" implies that the outputs of the system given an arbitary inputs doesn't depend on the absolute time. In other words, the time-invariant system must produce the same outputs with respect to the given inputs.

equations. When the state of the system can be determined by a set of variables $\boldsymbol{x}$, called *state variables*, its time evolution will follow the equation,

$$\dot{\boldsymbol{x}}(t) = \boldsymbol{A}\boldsymbol{x}(t)\,, \tag{4.5}$$

where the matrix $\boldsymbol{A}$ is called *system matrix* which characterizes the dynamics of the state with dimension of $n \times n$ where n is the number of states corresponding the length of the vector $\boldsymbol{x}$. In this case, the system is said to be of order n. To incorporate the system with the available control input, one can extend the equation of state so as to include the response to a set of input $\boldsymbol{u}$ via an matrix $\boldsymbol{B}$ called *input matrix*. Then the equation of state of the sytem becomes

$$\dot{\boldsymbol{x}}(t) = \boldsymbol{A}\boldsymbol{x}(t) + \boldsymbol{B}\boldsymbol{u}(t)\,, \tag{4.6}$$

which associates the state of the system with the given input. When the input vector $\boldsymbol{u}$ has a dimension of m, the input matrix $\boldsymbol{B}$ must have a dimension of $n \times m$, same number of rows as that of state variables and same number of columns as that of the input.

On the other hand, the output from the system $\boldsymbol{y}$ will be a superposition of the system's state projected via the *output matrix* $\boldsymbol{C}$ and direct couplings from the input via the *feedthrough matrix* $\boldsymbol{D}$, such that

$$\boldsymbol{y}(t) = \boldsymbol{C}\boldsymbol{x}(t) + \boldsymbol{D}\boldsymbol{u}(t)\,. \tag{4.7}$$

The combination of these equations which can determine uniquely the dynamics of the system (often also reffered to as *plant*) is known as *state-space representation*, summarized as

$$\begin{aligned} \dot{\boldsymbol{x}}(t) &= \boldsymbol{A}\boldsymbol{x}(t) + \boldsymbol{B}\boldsymbol{u}(t) \\ \boldsymbol{y}(t) &= \boldsymbol{C}\boldsymbol{x}(t) + \boldsymbol{D}\boldsymbol{u}(t) \end{aligned}\,. \tag{4.8}$$

The interpletation of the suspension's equation of motion to the state-space representation has one more step. While the equation of motion for the suspension system has a form of second-order differential equation, one should introduce additional first-order differential equation $\boldsymbol{v} = \dot{\boldsymbol{x}}$, enabling to write the equation of motion as a form of state-space model. Hence, setting the state variables as $(\boldsymbol{x}, \boldsymbol{v})$, we can obtain the state-space model of the suspension system from eq. (4.4), which is written as

$$\frac{\mathrm{d}}{\mathrm{d}t} \begin{bmatrix} \boldsymbol{x}(t) \\ \boldsymbol{v}(t) \end{bmatrix} = \begin{bmatrix} \boldsymbol{O} & \boldsymbol{I} \\ -\boldsymbol{M}^{-1}\boldsymbol{K} & -\boldsymbol{M}^{-1}\boldsymbol{G} \end{bmatrix} \begin{bmatrix} \boldsymbol{x}(t) \\ \boldsymbol{v}(t) \end{bmatrix} + \boldsymbol{B}\boldsymbol{u}(t) \tag{4.9}$$

The equation of motion determines only the components of the system matrix $\boldsymbol{A}$. The other matrices will be designed depending on the configuration of the sensors and actuators.

The point of state-space representation is that it can simply describe the dynamics of the system as a time evolution of the state variables even if the system has multi-inputs and

multi-outputs (MIMO). In the conventional way of frequency domain analysis, the system is described by means of transfer function which projects the input onto the output. The transfer function is a useful tool to express a single-input-single-output (SISO) system.

4.2   Control topology

The KAGRA control system is composed of a set of parallelized single-input-single-output (SISO) feedback loops. The policy of the suspension control in KAGRA is to process the displacement signals on the Cartesian basis defined in section 2.3. The Cartesian signals can be obtained from the sensor readouts in their disposed basis through the matrix operation, then the generated feedback signals in Cartesian coordinate are distributed to the real actuators to produce feedback forces in a proper direction.

The control topology for the Type-A suspension is illustrated in fig. 4.1. There are mainly four loops in the local control of the Type-A suspension. The IP control provides mode damping of the horizontal motions and DC positioning of the whole suspension chain. The GAS control deals with resonant mode damping and stabilization of the DC drift of the keystone's height. The BF control allows us to apply torsion mode damping on the single-wire chain which is unfeasible in the IP control. Finally the payload control addresses damping of the internal mode inside the payload and alignment control of the mirror. Since the actuators in the payload has designed so that the lower stage actuators have smaller actuation power for mitigation of the force noise coupling, the payload control adopts a scheme of handing over the feedback signals to the upper stages with more powerful actuator which is called hierarchical control [5].
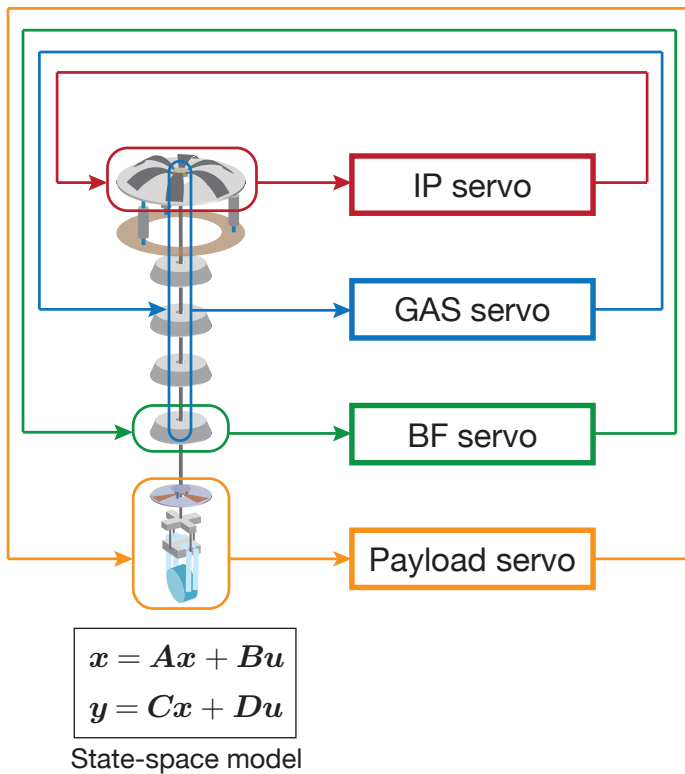
In the control simulation, the dynamics of the suspension system with multi-inputs and multi-outputs is represented as a state-space model. The inputs and outputs of the model are reshaped so as to correspond to the practial setup such as differential I/O for the GAS sensors and actuators.

4.3   1/e decay time reduction

The most important topic of the tower control is the mode damping of the mechanical resonances. Since the low-frequency oscillators are implemented at the tower stages, the eigenmodes with large amplitude in the tower stages' DoFs tends to have relatively low resonant frequencies and thus large impact on the RMS residual motion of the mirror.

The performance of the mode damping is evaluated as the exponential decay time for each eigenmode, as required in the calm-down phase. The simulated exponential decay time for the mechanical eigenmodes of the Type-A suspension is shown in fig. 4.2. While the Type-A suspension has totally 75 eigenmodes, the number of modes which shapes are mainly

Fig. 4.1. Block diagram of the local control of the Type-A suspension. In the model calculations in this chapter, the dynamics of the suspension system is represented as a state-space model with properly-arranged inputs and outputs. Here the global and hierarchical paths are omitted.

distributed over the tower stages is 36 and that which shapes are primarily contributed by the payload stages is 39. In absence of any control, the eigenmodes from the tower stages are distibuted in the lower-left region below $\sim 1\,\mathrm{Hz}$ with low Q-factors. By contrast, the eigenmodes from the payload stages have higher resonant frequencies with higher Q-factors which are mapped in the upper-right region in fig. 4.2. In practice, the quality of the mechanical resonances in the real suspension is generally limited by the actual installed setup such as the clamping of the suspension wires. Hence the model predictions of the quality factor or the 1/e decay time often lacks the precision to demonstrate the real system. Nevertheless, the following simulation of the damping control helps us to estimate achievable exponential decay times since the servo design gains suppression of the modal amplitude relying on the intrinsic high-Q peak of the mechanical resonances.

We can see the reduction performance of the 1/e decay times with tower damping control in fig. 4.2. In this damping control, servo filters are engaged in the IP loops for all 3 DoFs, one GAS loop at F0, and BF loops in 3 rotational DoFs. The design of the servo filters is a differential filter at the peak frequencies ($\lesssim 1\,\mathrm{Hz}$) generating feedback signals proportional to the velocity of the suspended stage, while forming a low-pass filter with a couple of poles in 1–5 Hz to reject the sensor noise reintroduction at high frequencies. Note that the damping control in the payload's DoFs is not discussed here because it will be addressed in the thesis
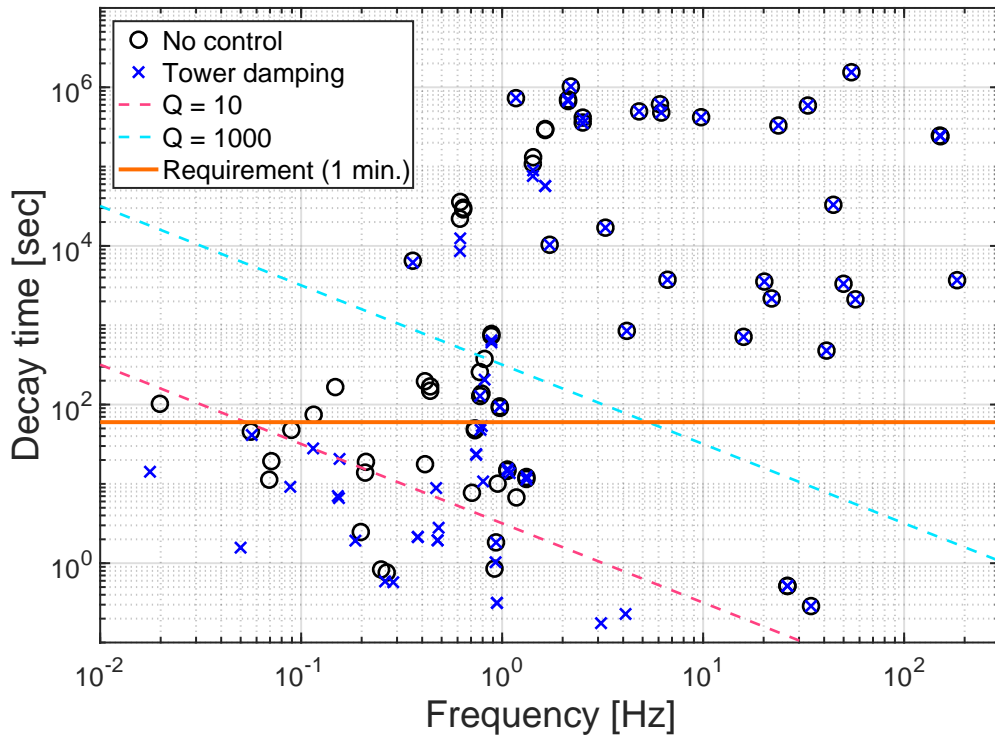
Fig. 4.2. Predicted 1/e decay time versus the mode frequencies of the mechanical resonances in the Type-A suspension. In the situation with the tower damping control engaged, the low-frequency modes

of the cryogenic payload development[2]. According to the simulaton, most of the eigenmodes comes from the tower stages can be successfully damped and its exponential decay times are reduced to less than 1 minute. Meanwhile, the decay time of the eigenmodes originating from the payload almost remains unaffected by the tower control loops. This fact illustrates a sense of significance of the performance test of the Type-A tower alone independently of the cryogenic payload. However, some of the tower modes which are plotted in the range of 0.5–1 Hz seem unrealistic to achieve the decay time shorter than 1 minute. Although these modes are identified as the DoFs corresponding to the tilts of the standard GAS filters, the Type-A suspension is unfortunately not equipped with sensing or actuating devices for these DoFs. Nonetheless, since it is expected that the modes in these rotational DoFs seem not to have substantial impact on the mirror's residual motions, the exponential decay time for these modes can be left as it is if one could confirm their couplings to the mirror motion are negligibly small.

---

[2] The thesis about the development of the cryogenic payload will be published in near future.

4.4 Modal damping control

Modal damping is a convenient way to decouple vibration into the normal modes of the system so that they can be damped independently. Control problems of a high dimensional system with many coupled DoFs can be simplified as a set of single DoF control problems, thereby minimizing complexity of the compensator design. As a result, it is relatively easy to find an optimal trade-off between damping performance and noise contamination in the damping control for each mode.

In this work, modal damping is applied to the vertical modes of the Type-A suspension originated from the chain of GAS filters. The advantage of these vertical DoFs is availability of many sensors and actuators distributed over most stages associated with the mode shapes. Since the resonant frequencies of the coupled GAS modes are localized in the range of about 0.1-1 Hz due to the softness of GAS, one should put importance on damping of those soft modes.

4.4.1 Modal decomposition

The method of modal damping handles vibration as displacement signals in *modal coordinate* and feedbacks them via controllers designed for each mode. The transformation matrix from the Cartesian to modal coordinate can be obtained using the mass matrix $\boldsymbol{M}$ and the stiffness matrix $\boldsymbol{K}$. Assuming the system has no damping, the linearized equation of motion in eq. (4.4) is written in the Fourier domain as follows.

$$(-\omega^2 \boldsymbol{M} + \boldsymbol{K})\tilde{\boldsymbol{X}}(\omega) = \boldsymbol{0} \tag{4.10}$$

This equation has a form of eigenvalue problem. Replacing the angular frequency as $\lambda = \omega^2$ and the displacement vector as $\boldsymbol{\phi} = \tilde{\boldsymbol{X}}$, it becomes

$$(\boldsymbol{K} - \lambda \boldsymbol{M})\boldsymbol{\phi} = \boldsymbol{0} \,. \tag{4.11}$$

Thus the set of eigenvalues λ and eigenvectors $\boldsymbol{\phi}$ of the system is obtained. Since $\boldsymbol{M}$ is positive-definite and $\boldsymbol{K}$ is non-negative definite, these eigenvectors are orthogonal and thus can become the basis of a coordinate which is called modal coordinate. The relationship between the modal coordinate and the conventional Cartesian coordinate is connected by the following equation.

$$\boldsymbol{x}(t) = \boldsymbol{\Phi}\,\boldsymbol{\eta}(t) \,, \tag{4.12}$$

$$\boldsymbol{\Phi} \equiv [\boldsymbol{\phi}_1 \; \boldsymbol{\phi}_2 \; \cdots \; \boldsymbol{\phi}_N] \,. \tag{4.13}$$

Here $\boldsymbol{\eta}(t)$ is a vector represents the position of the system in the modal coordinate. The matrix $\boldsymbol{\Phi}$ is the transformation matrix whose elements are the column-wise eigenvectors

(a) Stage-based   **(b)** Modal basis
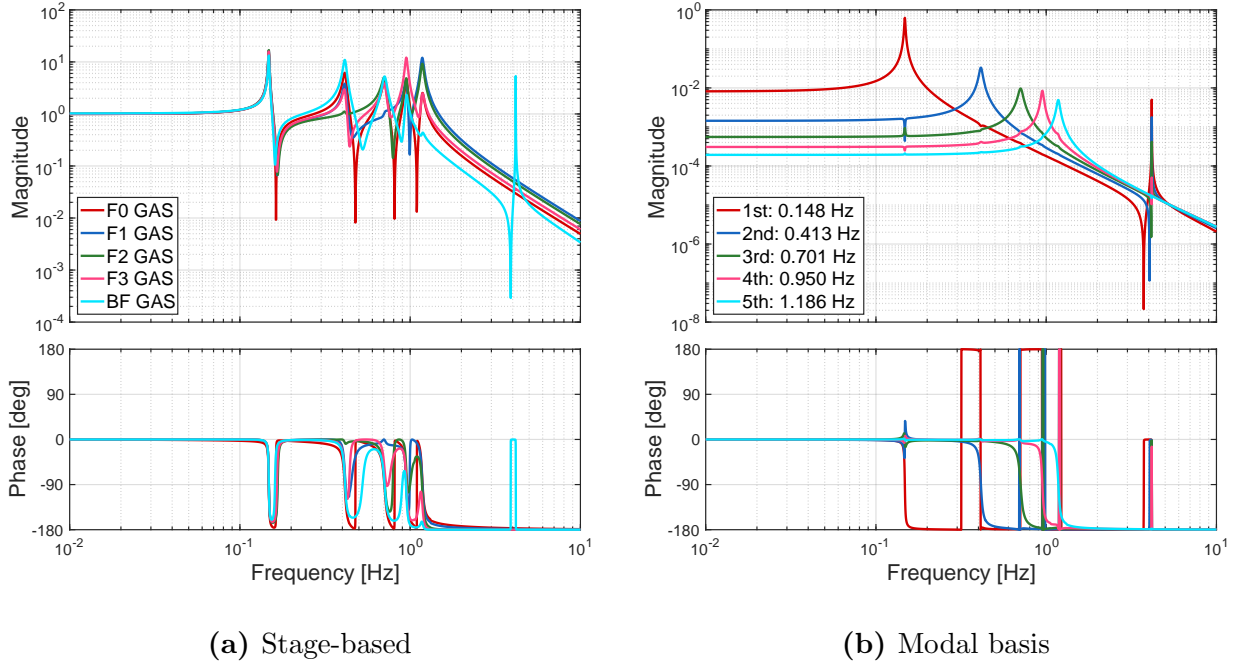
Fig. 4.3. Calculated transfer functions of the GAS stages in vertical direction. Every stage-based (LVDT- and actuator-wise) response in **(a)** has a fraction of all normal modes as a series of resonant peaks, while on the modal basis in **(b)**, the normal modes are separated into the responses of single second-order system.

aranged along the row from low to high order modes. Using the matrix $\boldsymbol{\Phi}$, the sensor signals can be converted to the displacement in the modal coordinate (called *modal displacement*) which indicates the amplitude of an specific mode in the system. Conversely, the feedback signals to damp the specific mode are distributed to the actuators via the matrix $\boldsymbol{\Phi}$ suited for the mode shape.

The calculated diagonal transfer functions of the GAS verical DoFs are shown in fig. 4.3, comparing those in unit-wise (LVDT- and actuator-wise) and in modal basis. Every unit-wise response is a mixture of all the normal modes which are shown as a series of resonant peaks in fig. 4.3a. On the other hand, the decoupled modal responses behave as a single second-order low-pass system like a simple harmonic oscillator, as shown in fig. 4.3b. Note that the norms of the eigenmode vectors used in the transformation matrix $\boldsymbol{\Phi}$ are normalized by their modal mass m_r so that $\boldsymbol{\phi}_\mathrm{r}^\mathsf{T} \boldsymbol{M} \boldsymbol{\phi}_\mathrm{r} = m_\mathrm{r}$ is satisfied for the r-th order mode. A large resonance which appears at 4.17 Hz comes from the internal mode of the cryogenic payload which was ignored in the modal decomposition. Although there remains a small amount of deviation from an ideal second-order response in the modal responses due to the accuracy of mode shape calculation, it is likely not to be a matter in terms of controller design because their phase distortion above the mode frequency less than 3 deg. In practical, the accuracy of

(a) F0 GAS loop

(b) 1st modal loop
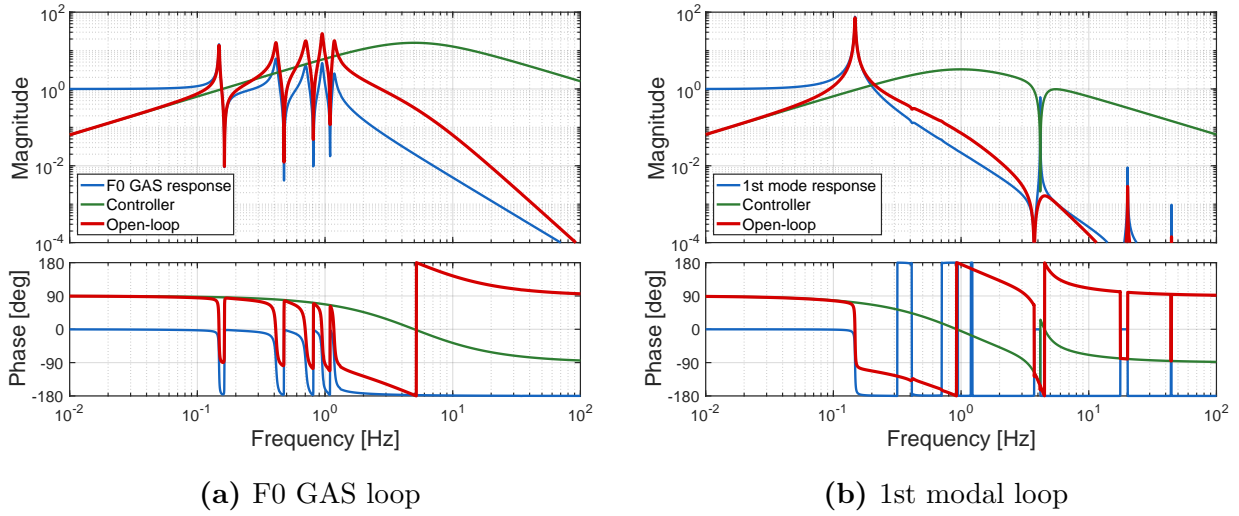
Fig. 4.4. Examples of the filter design and its open-loop transfer function for the damping control of the GAS vertical modes.

modal decomposition can be improved by diagonalization of the sensing and driving matrices.

4.4.2 Damping control performance

To see the damping performance of the modal control, we simulated the exponential decay time reduction of the vertical modes of the Type-A suspension with a simply-minded filter design. Since the damping control aims to suppress the vibration amplification at the mechanical resonances, one should design the servo filter so that the resulting open-loop transfer function has a gain more than unity at the resonant peaks. The basic strategy of the filter design here is placing one zero at a low frequency and several poles at a high frequency to cover the frequency region of the resonances. Such a zero-pole placement forms a differential controller at the peak frequencies, whereas it cuts off the high-frequency signals to prevent noise injection into the control loop. In this study, only the single-input-single-output (SISO) controllers are taken into account.

The examples of the filter design and their open-loop transfer functions are shown in fig. 4.4. In the stages-based control design, since almost all the mechanical resonances appear in a decade of the frequency region, it is difficult to reject the higher order modes out of the control and to lower the control bandwidth. On the other hand, the controller design in the modal basis shows much less complication due to the absence of the following higher order modes. Although some modes originated from the payload stay visible in the modal response, they can be easily rejected with notch filters due to its high quality factor and large separation in frequency from the lower-order modes of our interest. In the examples of the filter design, the bandwidth of the damping control is 1.1 Hz in the F0 stage-based loop
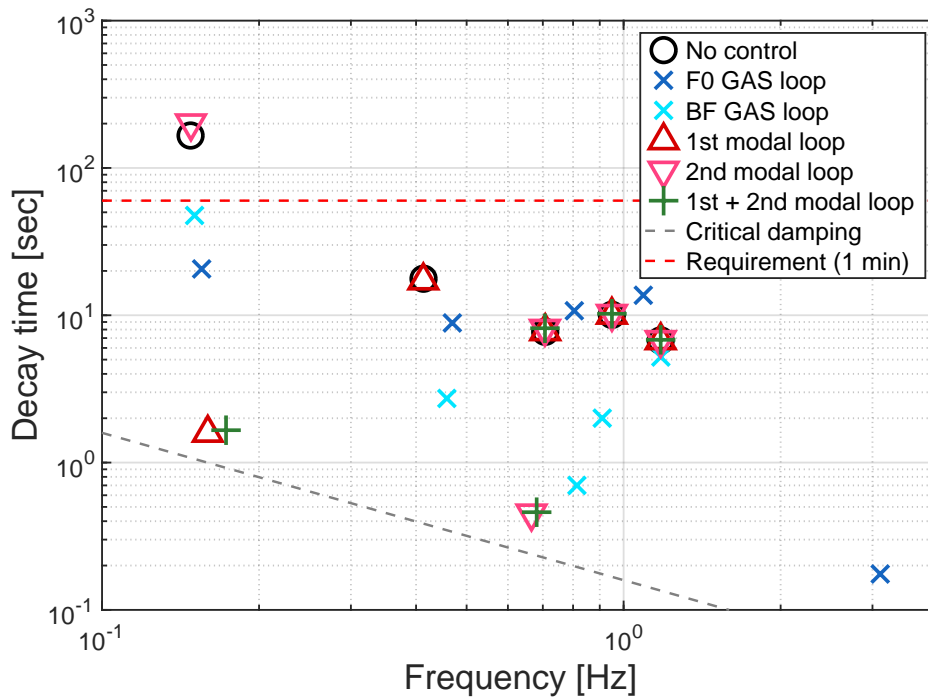
Fig. 4.5. Simulated exponential decay time for the vertical modes in the Type-A suspension. Only the lowest 5 modes originated from the GAS structure are plotted.

and 0.23 Hz in the 1st modal loop. The ignored higher-order mode at 4.17 Hz in fig. 4.4b, which comes from the blade spring at the platform stage, is rejected by a notch filter with a Q-factor of 3.

The result of exponential decay time reduction with various damping controls is shown in fig. 4.5. Here we simulated 5 setups of the control loop; two stage-based loops, two modal loops, and one combined modal loop. The F0 GAS and BF GAS loops are the conventional way to control the vertical modes using the sensor signal from a specific stage which is fed back to the actuator at the same stage. These F0 and BF are chosen as benchmarks of the conventional scheme because they are the top and bottom stage respectively in the tower part. The 1st modal and 2nd modal loops are the novel schemes proposed in this study. To check the selectivity of modal feedback to damp the specific mode, a setup with two modal loops closed is also investigated. All the controllers simulated here have designed in a similar manner described in the previous paragraph.

In a natural state without any control, it is predicted that only the 1st mode has a long decay time in excess of the requirement of 60 seconds. When a stage-based loop is closed, since its open-loop gain is more than unity at every resonant peak, the decay times for all the eigenmodes are reduced and the markers are replaced in fig. 4.5. However, the amount of the reduced decay time for each mode depends on its mode shape and thus one must dedicate

his/her effort to design the control topology to achieve a higher damping performance on a specific mode. On the other hand, the modal damping loops exhibit large decay time reduction in each specific mode with slightly interferring the other modes' property. The performance in the setup of two modal loops closed seems consistent with the setups of each single modal loop closed. In addition, the simplified system response allows us ealisy to design a controller achieving damping performance close to the critical damping. It can be explained that the information of a specific mode contained in the sensor signals is effectively used to suppress the vibration in the mode. Thus the modal control scheme can maximizes the effective sensor range and actuator range. Since the control of the suspension system deals with vibrations in many coupled DoFs, the modal damping is useful for not only the vetical modes but also other complinated DoFs such as payload control with longitudinal-pitch couplings.

Chapter 5

Performance test of Type-A tower

In this chapter, the experimental performance test of the Type-A suspension is presented. Even before the integration with the payload, the performance test of the tower part of the Type-A suspension is still worthwhile since the tower part contains important features of the low-frequency oscillator which determines a major fraction of the vibration isolation performance. Therefore, the explanation of the experimental setup, some of which are common to the full configuration but some are different, is described in section 5.1. In the following section 5.2, the measurement results for the system characterization in frequency domain is presented. Although all of the performance of interest could not be tested, the functionality of the torsion mode damping in yaw direction and modal damping for the GAS vertical modes were performed and reported in section 5.3 and section 5.4, respectively. In addition, we could perform a vibration isolation ratio measurement in the period of the test operation of the cryogenic Michelson interferometer, where the installed Type-A tower is integrated with the actual cryogenic payload. The result of the vibration isolation ratio measurement is finally presented in section 5.5.

5.1   Experimental setup

The performance test described in this chapter includes the results yielded from two different setups, the Type-A tower and full Type-A suspension. Due to the schedule of the KAGRA, the data for the performance test are taken in a period of the upgrade when the hardware installation of the Type-A suspension was ongoing and be incorporated into the interferometer. The study of this thesis focused on the

The two different setups for the performance test of the Type-A suspension is depicted in fig. 5.1. The clear difference of these setups is existence of the cryogenic payload, the bottom four stages. In the setup of Type-A tower, a dummy payload is suspended instead of the cryogenic payload from the bottom filter. As described in chapter 5, weight of the dummy

Table 5.1. Difference of the Type-A tower and full Type-A setup.

	Tower	Full
Stages	6	9
Height [m]	9.8	13.5
Eigenmodes	39	75
	Dummy payload	Cryogenic payload
Sensors	geophone L-4C	photoreflective sensor
		optical lever
		optical length sensor
Actuator	none	coil-magnet actuator

payload is adjusted to approximately coincide with that of the actual payload, while the length of the suspension wire for the dummy payload is 15 cm, much shorter than the actual maraging wire of 3.3 m because of the spatial constraint inside the vacuum chamber. Therefore, the Type-A tower is more than a little different from the full suspension in geometrical aspect.

Most of the test described in this chapter was performed with the setup of the Type-A tower before the integration with the cryogenic payload. Even without the actual payload, the Type-A tower can demonstrate the performance of vibration isolation and functionality of control. Of cource the dynamic characteristics of the system differs from that of the full configuration due to the difference of the mechanical geometry. The similarity and difference of these setups can be visualized in the eigenmode property shown in fig. 5.2. While the full Type-A suspension has totally 75 eigenmodes, the tower has 39 eigenmodes some of which are peculier to the tower setup such as ones associated with the tilt of the DP. We can see that the tower part includes most of the low-frequency eigenmodes common to both setups. Recalling the fact that,

- the lowness of the eigenmode frequencies determines the seismic attenuation performance in a given frequency region,

- the low-frequency eigenmodes have large impact on the residual RMS of the mirror fluctuation,

the characterization of the mechanical dynamics and demonstration of the damping control for the Type-A tower can be regarded as equivalent works to that of the full Type-A suspension. Moreover, since the tower or payload part itself is still a complicated multi-stage pendulum, necessity of examinations for each part alone is generally agreed in the view point of fault localization.
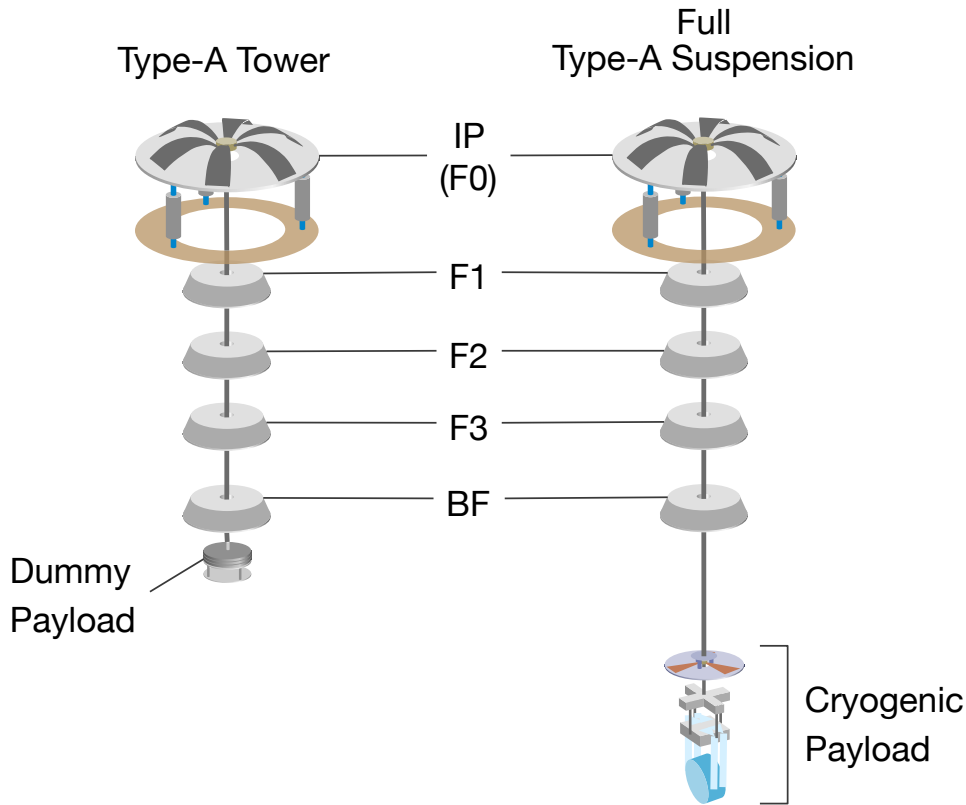
Fig. 5.1. An illustration of two setups for the performance test of Type-A suspension.

5.2 System characterization

The characteristics of the installed Type-A tower is determined by the accuracy of the mechanical assembling, that contains adjustment of the load or balance, geometrical positioning, and so many factors forth. In this section, the oscillatory behavior of the installed system was identified by measuring the mechanical transfer functions and spectra in a stationary state for the controllable and observable DoFs. The measured results were compared with a prediction of the 3D rigid-body model having the design parameters and hence its performance was discussed with their consistency.

5.2.1 Diagonal transfer functions

The mechanical responses of the suspension system are described in terms of force-displacement transfer functions of the suspended masses in frequency domain. For this purpose, virtual sensors and actuators based on the Cartesian coordinate are constructed in the digital system with linear combination of the real sensors and actuators.

The measurement was performed by injecting excitation from a virtual actuator in a certain DoF and taking a the resulting displacements measured with the virtual sensors. We
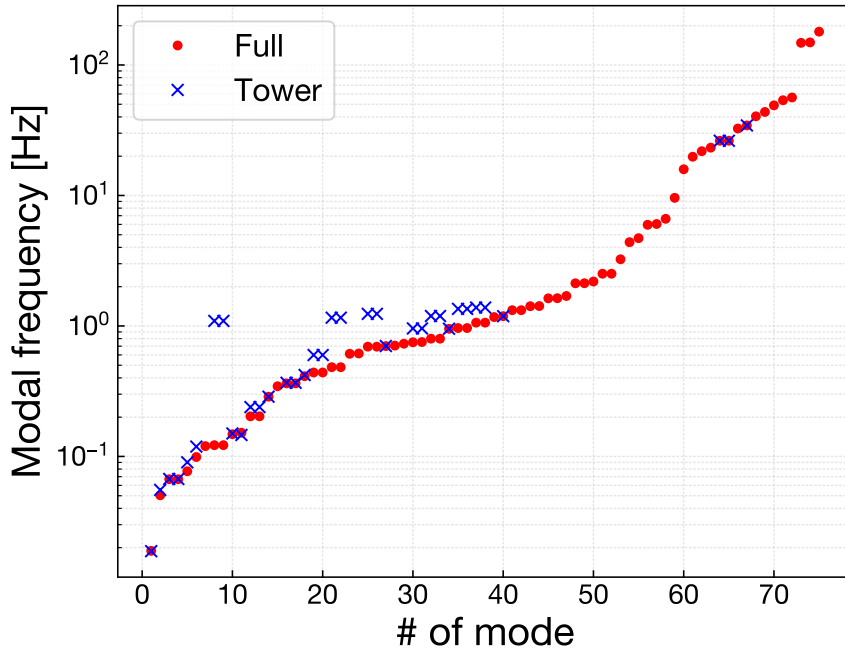
Fig. 5.2. Comparison of modal frequencies between the full configuration and the tower part of the Type-A suspension. The mode index of the tower is arranged so that their modal shapes are similar to that of the full suspension.

used two types of excitation signal; one is broadband Gaussian injection which can excite the system in a wide frequency range at one measurement, the other is monochromatic sinusoidal injection swept over the frequency range of interest. The formar has advantages of short measurement time, getting quick result in all over the frequency region and comparatively higher resolusiton of the sampled frequency points, while the latter is superior in S/N ratio of the measurement due to taking sampled data points one by one but instead needs long measurement time. We used the Gaussian injection in most measurements where vibration in the DoF is well excited due to the softness of the spring or the strength of the actuation power. Only some DoFs, especially ones at the bottom filter, are measured with the swept-sine excitation.

Note that all the DoFs of the stages as well as all eigenmodes are not sufficiently controllable and observable due to the configuration of the sensors and actuators.

Horizontal DoFs at inverted pendulum

The inverted-pendulum (IP) stage can move in horizontal three DoFs, namely longitudinal, transverse, and yaw direction. The measured diagonal transfer functions in the horizontal DoFs of the IP is shown in fig. 5.3. The gross feature of the transfer functions are consistent with the model prediction for all three DoFs. Nevertheless, several discrepancies between

the measurement and model are recognized. The discrepancies and possible explanations are detailed below.

- In longitudinal and transverse direction, the measured resonant frequency of the first mode deviates from the model's value. The model predicts that the resonant frequency is 67.3 mHz, while in the measurement it is 58.6 mHz in londitudinal and 65.7 mHz in transverse those are in the range of 13% from the model's value. The deviation can be explained by assuming asymmetry in stiffness of the IP legs. Considering the nominal value of 67 mHz for the resonant frequency of the IP stage, the installed system possesses sufficient low-frequency resonance for the first eigenmode. Note that the model doesn't take the asymmetry into account.

- A small bump appears at 0.4 Hz in the longitudinal and transverse transfer functions. This bump can be considered as a coupling from a resonance in yaw direction.

- In longitudinal and transverse transfer functions, the mismatch between the measurement and model in the frequency range from 0.7 Hz to 1.1 Hz reflects unmodeled dispersion of the suspension points on the GAS filters which affects mode frequencies in their rotational DoFs. Due to the change of mass distribution by load adjustment, the position of the center of mass is different for every GAS stages. In addition, the height of the GAS keystone is not constant; it drifts by a large amount with temperature change. Hence the distance of the suspension points from their center of mass changes over time which behavior is difficult to be modeled. However, the discrepancies can be acceptable since these not-well-modeled features coming from the tilt of the indermediate GAS stages have less impact on the residual motions of the mirror.

Vertical DoFs in GAS filter chain

In the chain of GAS filter stages, vertical motions are the only DoFs both measurable and controllable except for the bottom filter. Since LVDT sensors and co-axial coil-magnet actuators are implemented on the keystones with respect to their filter's body, we can only measure the relative transfer functions between the suspended stages. Since all the mode frequencies for the GAS vertical modes are expected to be above 0.1 Hz, the frequency responses above 0.03 Hz were measured with the Gaussian injection.

The measured diagonal transfer functions of the GAS vertical is shown in fig. 5.4. There are large deviations in the frequency responses between the measured results and model predictions. Since the GAS filter chain can be regarded as a 5-stage-coupled mass-spring system, one expects to observe nominally 5 mechanical resonances in its response. In fact, the model predicted 5 peaks in the frequency responses, the appearance of which (namely,

(a) Longitudinal

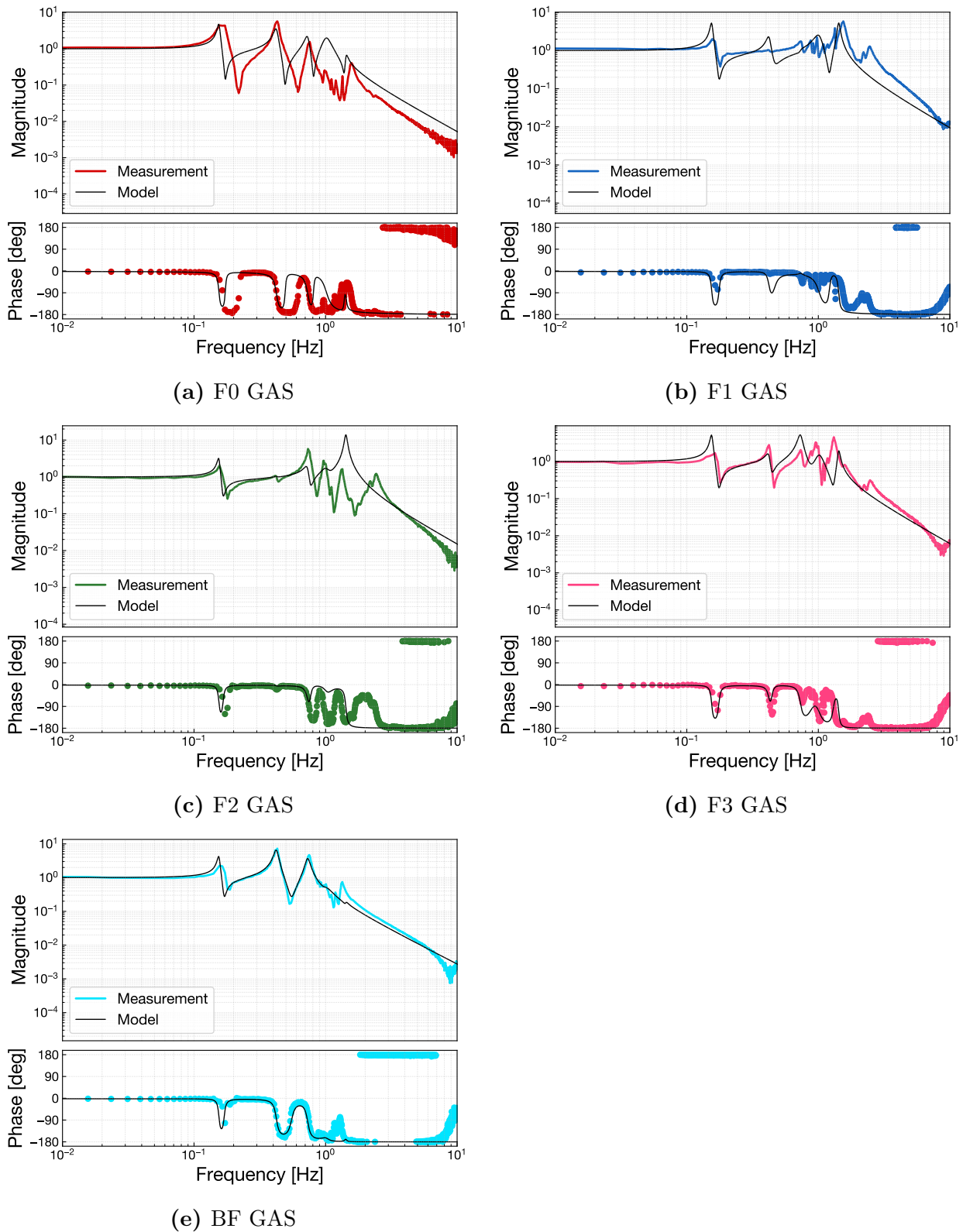**(b)** Transverse

(c) Yaw
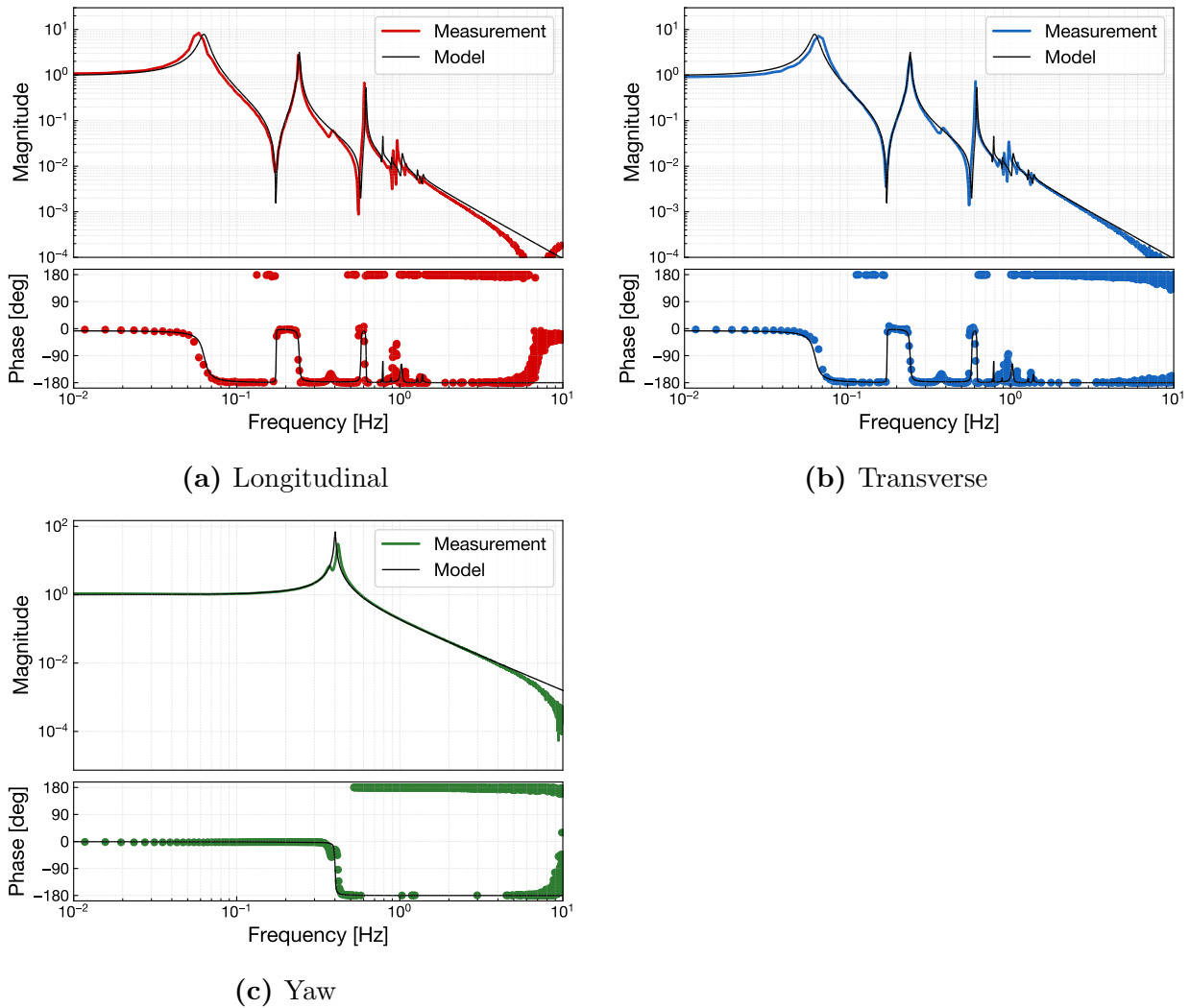
Fig. 5.3.   Diagonal transfer functions about the IP stage. The measured data are plotted as colored curves comparing with results of the rigid-body model plotted as black curves.

height distribution of the peaks) in each stage depends on their mode shapes. However, the measurement results show remarkable mismatch in their peak appearance for the higher order modes, although the modal frequencies for the lowest 1st, 2nd, and 3rd modes show coincindence between the measurement and model. These discrepancies seem caused by the uncertainty of the model using incorrect set of parameters such as mass, damping factor, and stiffness distribution. The uncorrelated deviation of the parameters in each individual stage affects especially the characteristics of higher order modes having finer mode shapes. The result indicates that the installed Type-A tower has many small deviations in the physical parameters in vertical direction.

In addition, small peaks not originating from the pure GAS vertical modes are visible in the measured frequency responses above ~ 0.8 Hz. These structures can be explained as

contributions of coupling from the tilt of the GAS filters. Given the horizontality of the GAS stages assembled by human hands, the tilt modes in pitch and roll rotation can cross-couple to the vertical translation. The resonant frequencies of such rotational modes are expected to be in the range of 0.8–2 Hz, depending on the static position of the keystone. Therefore, the unmodeled peaks being observed around 1 Hz in the measurement results are conceivable.

To summarize the discussions above, although the behavior of the lower order modes are realized as expected, the constructed Type-A tower has some level of discrepancy from the design or the expected model. Since the low-frequency behavior has an impact on the vibration isolation performance, it seems the total operationability of the vertical seismic attenuation is still valid. To investigate the performance further, the residual motion of the suspended dummy payload is discussed in the next section. Besides that, in the view point of constructing a model of the existing system, there is another approach to build a model based on the measured response which is known as a topic of system identification. This method of measurement-based modeling is a possible application to the Type-A suspension in the future.

(a) F0 GAS

(b) F1 GAS

(c) F2 GAS

(d) F3 GAS

(e) BF GAS

Fig. 5.4. Diagonal transfer functions about the GAS stages. The measured data are plotted as colored curves comparing with results of the rigid-body model plotted as black curves.

Six DoFs at bottom filter

The bottom filter has totally six LVDT-actuator units which enables us to measure transfer functions in all the 6 DoFs around the BF. Since these actuators on the BF were weak and broadband Gaussian injection couldn't excite the mechanical oscillation sufficiently, we performed the measurements with swept-sine excitation sampling 25 points per decade. Thus the resulting transfer functions have relatively worse frequency resolutions.

The measured transfer functions about six DoFs of the bottom filter is shown in fig. 5.5. Similarly to the results of IP and GAS, the model predictions are also plotted as black surves. The explanations and discussions for each panel are listed below.

- The frequency responses in longitudinal and transverse show good consistency up to the resonant peak of the 2nd mode at 0.241 Hz. However, the 3rd mode at 0.636 Hz which the model predicts is less visible in the measured longitudinal response and almost invisible in the meausured transverse response. It could be not-well-measured due to the worse frequency resolution or deterioration of coherence at the resonant peaks over averages of the measurements. Since the peak structure up to the 2nd mode is observed and well explained with the model, it is unlikely of malfunctioning such as mechanical contact on the surrounding instrument. In the frequency range of 0.8–1.4 Hz, there are several small peaks which seems coming from the tilt of the GAS filters coupled to the translational DoFs. These couplings are difficult to be modeled and below the problematic level in the results.

- The result in the vertical direction has, as discussed in the result of the GAS transfer functions, large deviation from the model, especially in the behavior of higher order modes. The possible explanations are similar to ones described in the GAS results.

- In roll and pitch, the bottom filter shows expected frequency reponses consistent with the model prediction. Some small structures other than the main peak of 0.907 Hz can be seen as far as the sampled points reconstruct.

- The frequency response in yaw shows good consistency in the measurement and model in the broadband region. Although the quality factors of the three resonant modes are not well predicted, it is within expectations because the quality factors in a real-world system are determined by the practical situations and therefore difficult to be modeled. The appearance of the 2nd mode at 60 mHz seems not matched with the model which seems also caused by the incorrect stiffness distribution of the model. Since the 2nd mode has nominally a mode shape less observable and controllable at the BF, a small deviation from the nominal parameters could result in comparatively large change in the behavior of that mode.

- At high frequencies above ~ 2 Hz, all the tranfer functions show f^2 dependency. This is known as a sprious couling in the BF LVDT where the excitation signals sent to the actuator directly transmit to the sensor coil due to the implementation of the shared coil.

According to the discussion above, we can summarize that the bottom part of the installed Type-A tower shows roughly expected performance as it being designed. In this test, the diagonalization of the sensor and actuator is not completed yet due to the limitation of the experiment period. Since the yaw rotation of the BF is extremely soft, the coupling between yaw and other DoFs may become an obstruction of the control design. The diagonalization of the sensor and actuator, reducing the cross couplings in the DoFs, is necessary in the further steps.
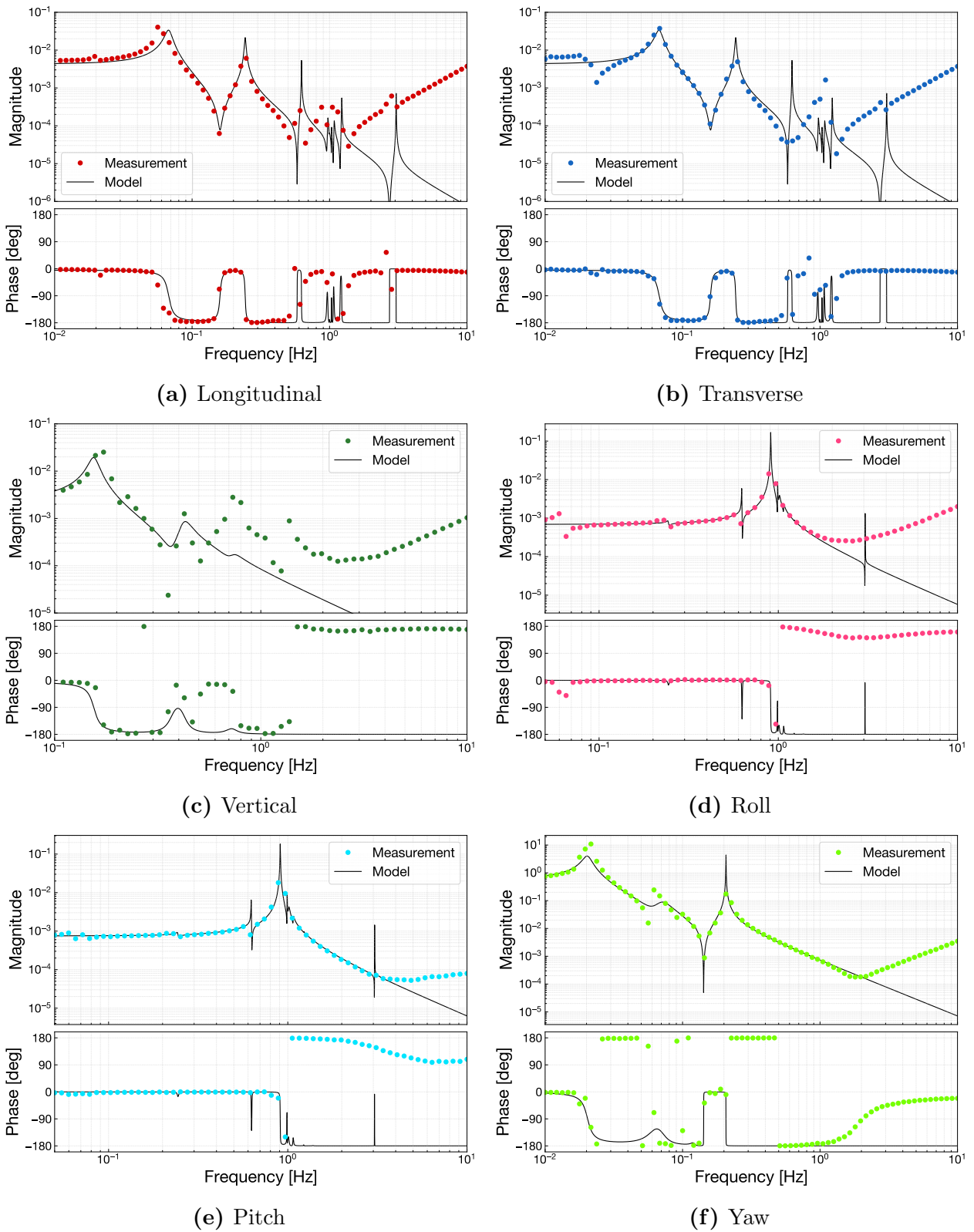
Fig. 5.5. Diagonal transfer functions about the bottom filter. The measured data are plotted as colored curves comparing with results of the rigid-body model plotted as black curves.

5.2.2   Residual vibration in a statinonary state

We measured residual motions of the stages in the installed Type-A suspension in a steady state. The amplitude spectral density of the residual motions in Cartesian DoFs are plotted in fig. 5.6, fig. 5.7, and fig. 5.8. Most of the peaks in the spectra correspond to the mechanical resonances of the suspension, while inclined floors are appearance of the background noises.

(a) Longitudinal

(b) Transverse

(c) Yaw
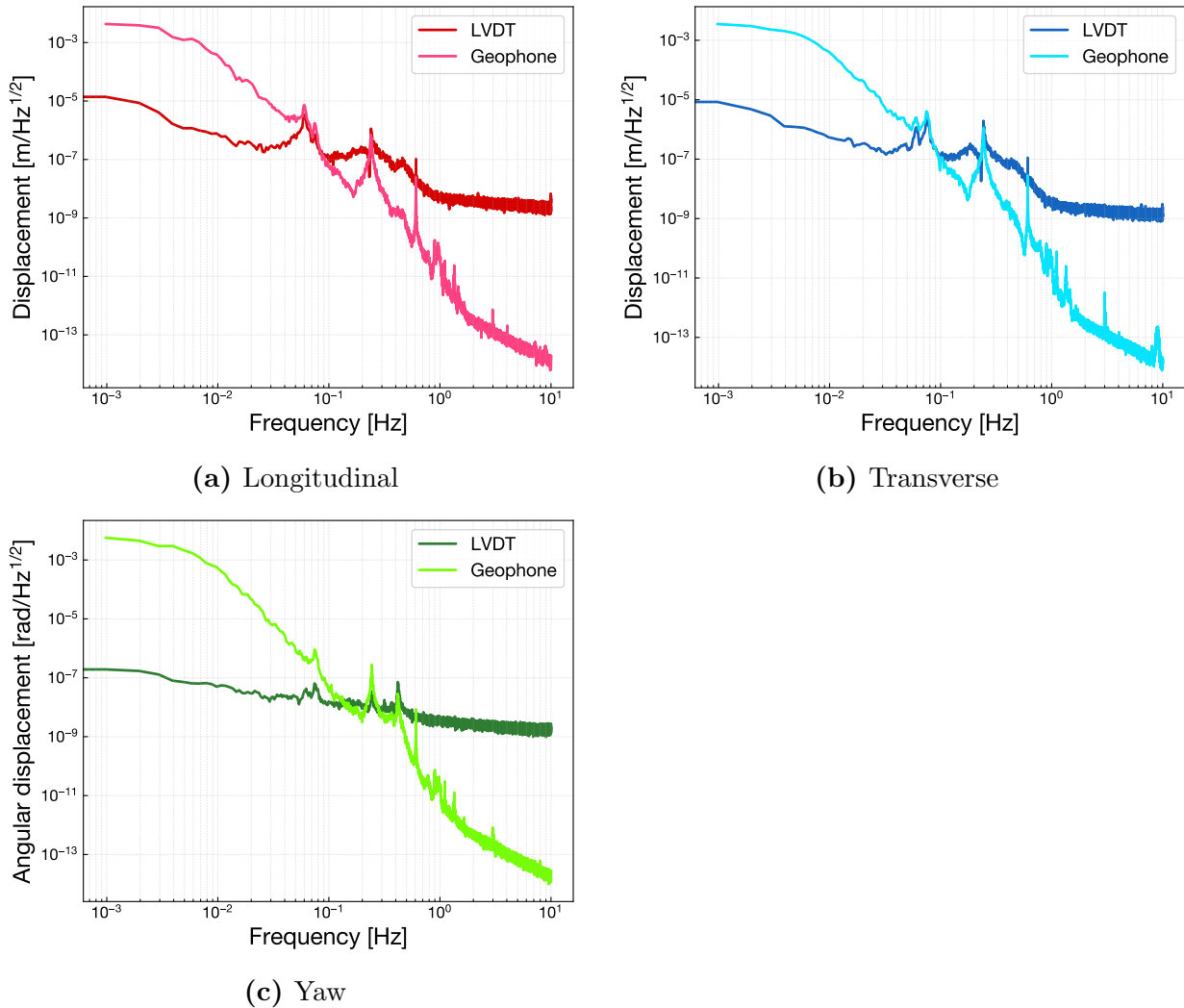
Fig. 5.6. Amplitude spectral density of the IP in a stationary state without any control.

IP pre-isolation stage

The residual motion of the IP stage is monitored with two kinds of sensors, LVDT and geophone. The measured speacta in fig. 5.6 shows clear difference in the characteristics of these sensors. Since the LVDT monitors displacement of the IP stage with respect to the

ground, the amplitude is dominated by the microseism in the range of 0.1–0.9 Hz, excepting some excesses of the mechanical resonances, in the spectra of the translational DoFs. By contrast, the geophone is less sensitive to the ground motion because it measures velocity with respect to the inertial frame. Therefore at the microseismic frequencies the geophone spectra has a floor level smaller by 1–2 orders of magnitude than the LVDT's. To damp some high-Q eigenmodes independently of the microseismic disturbance, one should use rather the geophone signals for a feedback control than the LVDT signals.

On the other hand, the LVDT exhibits superiority in position stabilization at lower frequencies below ~ 0.1 Hz. In terms of displacement, the inherent noise of the geophone is amplified as the frequency decreases due to its frequency response. Since the LVDT reads out displacement signals with less frequency-dependent noise floor, it is a natural way to use the LVDT to maintain the static position of the IP stage with respect to the reference frame.

GAS filter chain

The measurement results of the vertical residual motion in the GAS stage are shown in fig. 5.7. The first mode (0.18 Hz) and the second mode (0.46 Hz) appear as significant peaks, moreover the third mode peak is slightly visible at 0.77 Hz. However, the higher order modes, namely 4th and 5th modes, seem not observed in a stationary state. It indicates that the system of the Type-A GAS chain doesn't store oscillatory energy in the higher order modes large enough to be observed with the LVDT sensors. Note that the sensor noise in each GAS stage has different floor level since the LVDT noise has a DC position dependency of the keystone.

Bottom filter

Since the local sensors at the BF monitor the relative displacement of the BF body with respect to the ground, the residual motions of both the suspended stage and the ground itself can be observerd. In fig. 5.8a, whereas the many resonant peaks are standing with high quality factors, a broad bump of the microseismic motion appears in the range of about 0.1–0.8 Hz for all the translational DoFs. If the local control including this band is engaged, it will introduce the seismic noise into the suspended BF and can be problematic.

One potential problem at the BF is the large cross couplings between the DoFs. In this test, the diagonalization of the sensing matrix and driving matrix is not applied yet due to the limitation of the experiment period. Since one of the important role of the BF LVDT is to damp the torsion mode of the single-wire suspension chain, a cross coupling from the translations in the microseismic band can cause unexpected excitation into the yaw control. Actually, the some peaks of the yaw modes, located at 21 mHz and 63 mHz, are coupled to the translation DoFs and observed in their spectrum. Similarly, the spectrum in the rotational
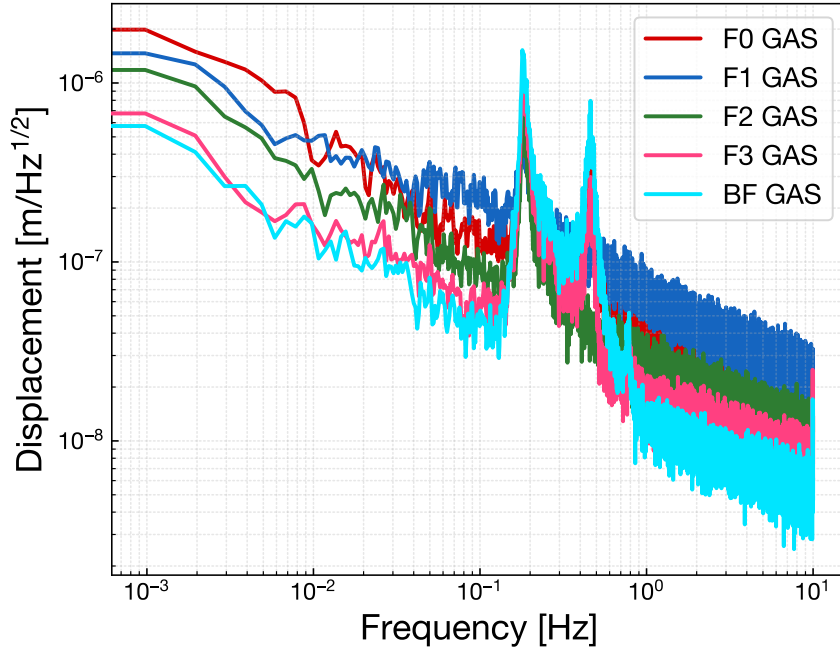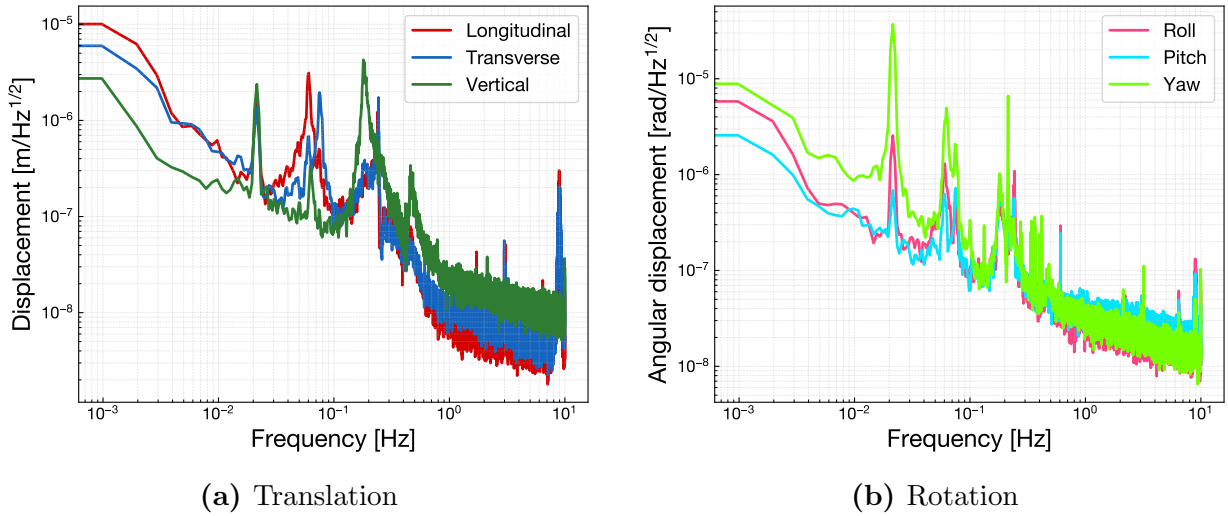
Fig. 5.7. Amplitude spectral density of the GAS LVDT in a stationary state without any control.

direction also shows some influence of coupling from the translations leading some peaks such as ones at 73 mHz and 0.18 Hz. To confirm the small enough magnitude of DoF-couplings, further handling of sensing and driving matrix will be necessary.

Residual motion at dummy payload

During the performance test of the Type-A tower, we have additional sensors at the dummy payload. Two geophones, a same type as mounted on the IP stage, are implemented on the DP for the horizontal and vertical motion sensing. The geophone is chosen since it can measure the residual motion of the attached object with respect to the inertial frame, independently of fluctuation of the reference frame such as the ground. However, owing to the limited capacity of the dummy payload, we have implemented on the two translational DoFs, namely one horizontal and one vertical, geophones and no angular sensing is available.

The measured residual vertical motion of the DP is shown in fig. 5.9. For comparison, the spectrum calculated with the model and the measured seismic noise is also plotted. The magnitude of the seismic noise in this measurement is roughly as large as the Kamioka High Noise Model (KHNM) which is mentioned in section 3.1.1. Although the measured transfer functions of the GAS stages are not well consistent with the responses predicted in the model as discussed in section 5.2.1, the spectra of the measurement and the model show good coincidence below 1 Hz except for the quality factors at the resonant peaks. This

(a) Translation

(b) Rotation

Fig. 5.8. Amplitude spectral density of the BF in a stationary state without any control.

result can be also one evidence to guarantee the total operationability of the vertical seismic attenuation for the constructed Type-A system, compensating the small consisntency in the results of the transfer function measurements. However, there is still unmodeled structure above 1 Hz which looks like a series of small resonant peaks. This is a common feature also observable in the measured frequency responses and seems originating from the tilt couplings of the GAS stages. Since the geophone is not sensitive to detect the residual motions above 2 Hz, we cannot conclude that the impact of these cross couplings are acceptable even in the observational band starting from 10 Hz. That should be tested after the integration into the full configuration of the Type-A suspension.

In a natural state under even the noisy seismic disturbance, the RMS residual motion of the DP is measured as 5.3 μm. Considering the requirement of the vertical RMS displacement is less than 0.1 mm, we can conclude that the resonant modes in the vertical direction will not amplify the residual motion of the payload more than the required level.

The measured residual horizontal motion of the DP is shown in fig. 5.10. Note that the horizontal geophone was aligned to the nominal longitudinal direction, but its orientation is possible to vary in the range of $\pm 1.4°$ due to the yaw motion of the suspension chain. The spectrum of measured residual motion of the DP has unnaturally small magnitude comparing to the model prediction. Although some of the visible peaks can be explained as the coupling from the vertical motion which amount is estimated as 0.3 %, the contribution at the other peaks are inconsisntent with either the model calculation with the measured seismic noise or the measured spectrum at the BF, the next upper stage. Since the spectrum measured at the BF shows coincidence with the seismic spectrum, in addition the unresolved peaks has the same frequencies with the longitudinal resonant modes such as 0.24 Hz and 0.63 Hz, it is reasonable that the horizontal geophone at the DP somehow failed to monitor the pure
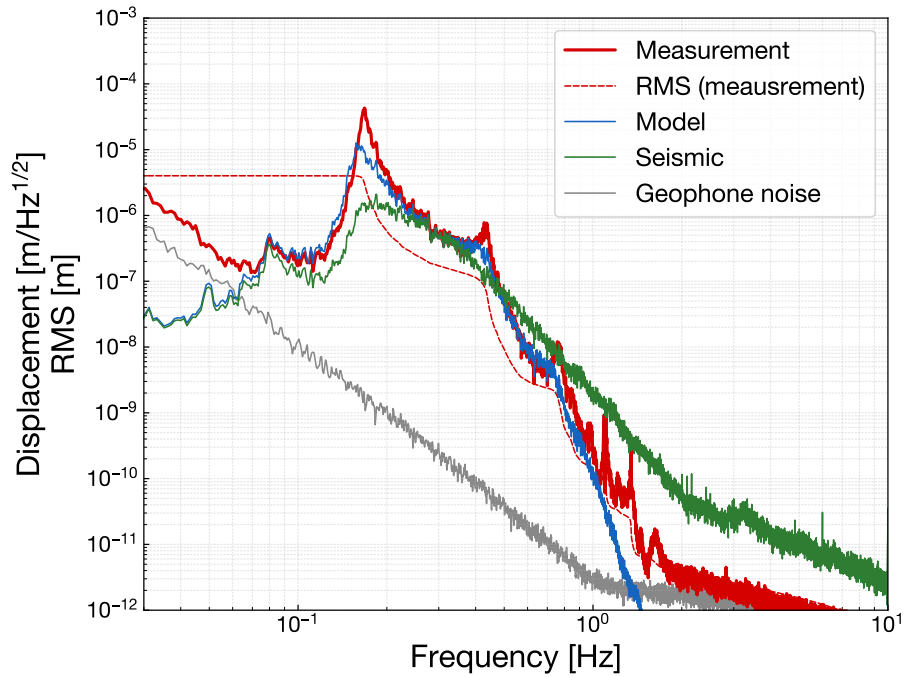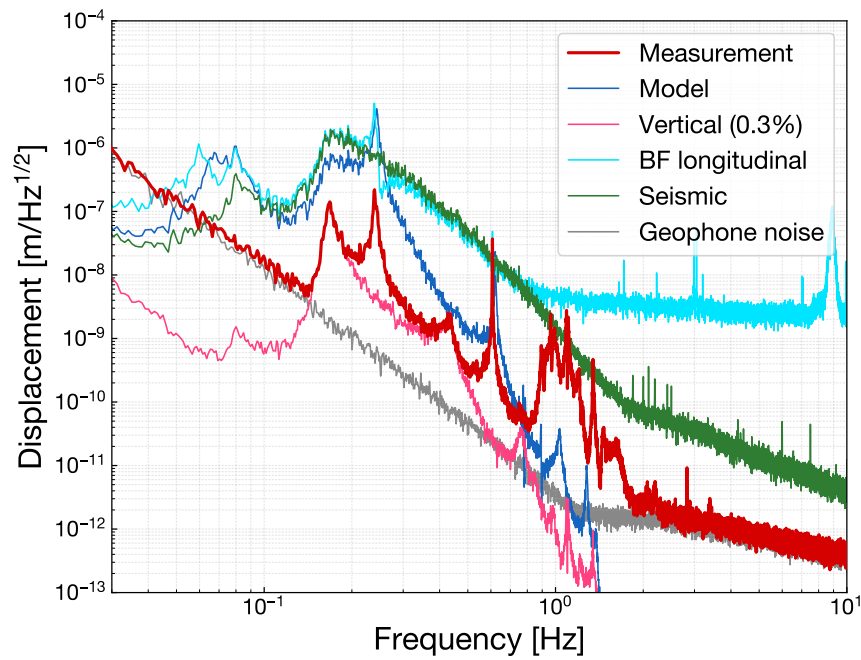
Fig. 5.9. Amplitude spectral density of the vertical motion of the DP in a stationary state. The spectrum labeled as "Model" is calculated from the measured seismic spectrum multiplied by the transfer function model from the ground to the DP.

translation of the DP. The measured spectrum also shows the bump structure around 1 Hz similar to the one observed in the vertical geophone spectrum. The contribution of this bump seems the same level as the vertical spectrum, without being attenuated unlike the peaks of the longitudinal modes. Although we cannot reveal any more the reason why the horizontal geophone observed such a strange spectrum, the descrepancy could be possibly caused by the improper attachment of the geophone with rattling, assymmetric positioning offset from the DP's center of mass, and so on.

The important RMS value in the longitudinal direction is the RMS velocity required for the smooth lock acquisition. In spite of the fact that the Type-A tower setup doesn't have the actual payload, it can give a reference value of an achievable RMS velocity for the whole center-of-mass motion of the suspended payload. However, as discussed above, the horizontal geophone attached on the DP is no longer useful to evaluate the residual motion of the DP. Thus instead, the RMS residual velocity was evaluated with the spectrum measured at the BF which is plotted in fig. 5.11. The RMS velocity is obtained as a cummulative integration from 3 Hz down to 0.03 Hz in order to take only the mechanical motion into account and not to include the sensor noise contribution at high frequency. Even assuming the resulted RMS velocity of the BF is contributed by the pure BF motion, the measured RMS velocity is 0.73 μm/s which is much less than the requirement of 240 μm/s. Thus, although the horizontal geophone at the DP couldn't give a meaningful result, it is indicated that the sufficiently

Fig. 5.10. Amplitude spectral density of the horizontal motion of the DP in a stationary state. The spectrum labeled as "Model" is calculated from the measured seismic spectrum multiplied by the transfer function model from the ground to the DP. The coupling from the vertical motion and the BF's longitudinal spectrum is also plotted for comparison.

small RMS velocity is achieved with the constructed Type-A tower instrument.
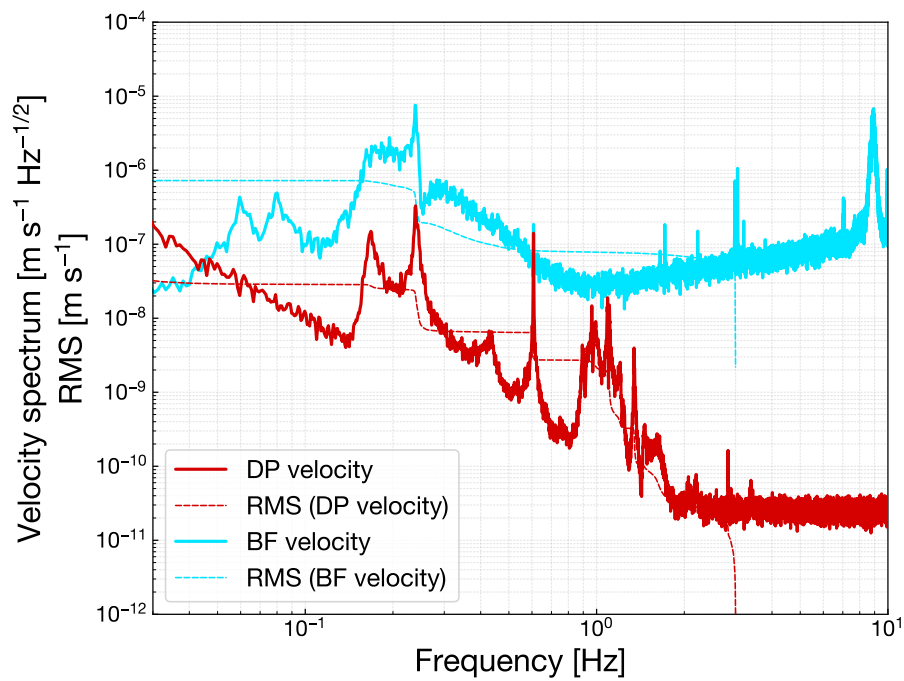
Fig. 5.11. Velocity spectral density of the longitudinal motion of the DP and BF in a stationary state. The RMS is integrated from 3 Hz down to the low frequencies in order to exclude the sensor noise contribution.

5.3   Torsion mode damping

The torsion mode of the Type-A suspension is one of the considerable-DoF oscillation. As mentioned in the previous chapters, the Type-A suspension has long single-wire chain which can also behave as a torsion pendulum with high quality factor. Nevertheless, the torsional motion of the suspended mirror leads misalignment of the interferometer, meaning large amount of beam spot fluctuation at the 3-kilometer distance. Therefore we need to implement apropriate damping function onto the oscillation in yaw direction of the Type-A chain.

The setup of the Type-A tower, in absence of the cyogenic payload, is still a suitable instrument for testing the torsion mode damping since the dynamics of the yaw motion is almost subject to the mechanical properties of the tower part accounting a major fraction of the total wire length. In the two angular DoFs for the mirror alignment, namely pitch and yaw, the yaw motion is contributed by single-wire components with low torsinonal stiffness distributed over the whole chain, while the pitch motion is dominated by the multi-wire suspension design inside the cryogenic payload. A single-wire connection has small torsional stiffness, whereas it has less coupling in the tilt of the masses when the suspension points are close enough to their center of mass. On the other hand, a multi-wire connection with some horizontal offsets from their center of mass has larger stiffness in pitch and yaw, causing strong mechanical coupling between the connected masses. Thus, although the pitch of the test mass is strongly coupled to the marionette with being less affected by the tower stages, the yaw will be substantially correlated to the torsion of the tower stages.

The only stage in the Type-A tower where we can apply the yaw control is the bottom filter. As described in section 3.4.1, the bottom filter is equipped with the sensor-actuator-integrated device BF LVDT for all 6 DoFs of the BF body with respect to the ground. Although the cryogenic payload in the full configuration has additional angular sensors such as optical levers and photo-reflective sensors, there is no other sensors and actuators available in the tower stages than ones at the BF. The LVDT at the IP is also useless as long as we discuss the yaw motion of the suspended stages with single-wires. Thus the torsion mode damping here is a topic of single-input-single-output (SISO) control problem at the BF.

In this study, torsion mode damping of the Type-A tower is performed in order to satisfy two types of requirements, $1/e$ decay time for the mechanical resonances and RMS residual motion in the frequency region above 10 mHz. The $1/e$ decay time is a requirement in the calm-down phase for quick recovery of the interferometer operation when a large disturbance excites the instruments. The RMS residual motion is one in the lock-acquisition phase so that the control can be switched to another which uses more sensitive but smaller-ranged sensors and actuators.
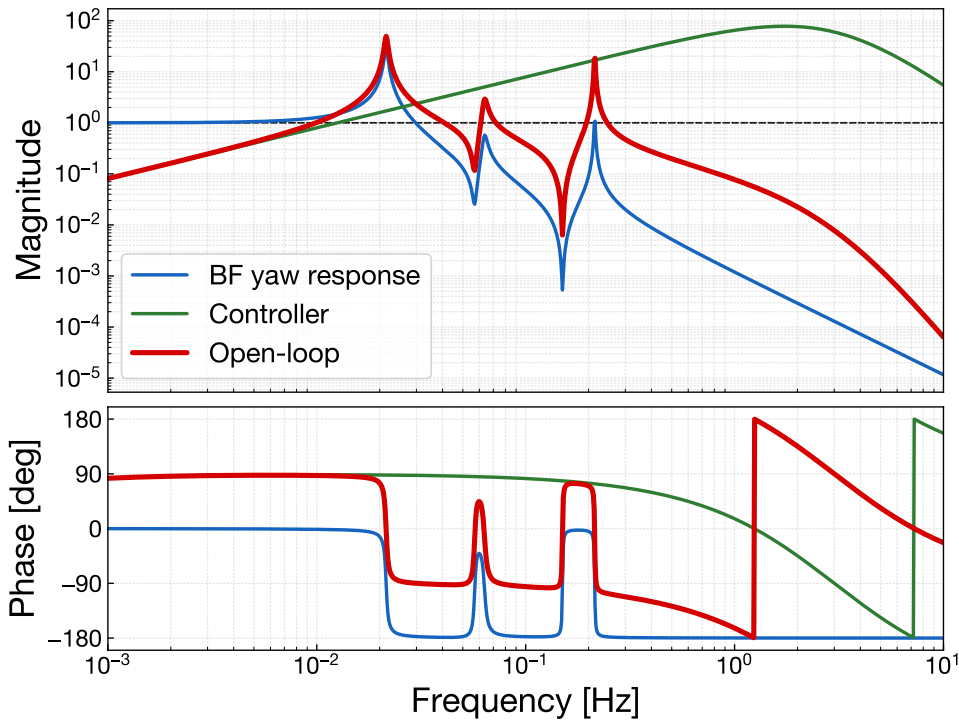
Fig. 5.12. The open-loop transfer function of the BF yaw damping control.

5.3.1   Controller design

The aim of the damping control is to suppress the mechanical resonances in the yaw direction. Since the lower resonant modes will often dominate the magnitude of RMS fluctuation, we focused on the three resonant modes from the lowest. This strategy is also natural considering the fact that the lowest three resonances are visible in the measured frequency response of the yaw DoF at the BF.

The open-loop transfer function of the BF yaw damping control is shown in fig. 5.12. The frequency response of the BF yaw is constructed as a SISO model Based on the measured transfer function in fig. 5.5f, and then normalized at the DC. The modeled BF yaw response has three mechanical resonances with the mode frequencies of 21.5 mHz, 63.5 mHz, and 214 mHz respectively which are identified in the spectrum in a stationary state. In fig. 5.12, the peak of the 2nd mode looks relatively small due to its mode shape, indicating this mode has poor controllability and observability for the input/output point of the BF.

The controller of the damping servo has a 1st-order high-pass feature up to 1 Hz and a 3rd-order low-pass feasure above 3 Hz. The overall character of the controller is designed so that the resulting open-loop transfer function has a gain of more than unity at and around the mechanical resonant peaks. The 1st-order high-pass character at the frequencies of the peaks guarantees the stability of the feedback loop, while the low-pass character at the high frequencies aims to reduce sensor noise reinjection through the sprious coupling in the BF

LVDT. The bandwidth of the damping control is up to the 3rd resonant mode, interpreted as a unity-gain frequency of 0.24 Hz. The stability of this control loop is parametrized as the minimum phase margin of 74.5° and the gain margin of more than 10.

5.3.2 Decay time measurement

To evaluate the damping performance required in the calm-down phase, the exponential decay time was measured for each resonant mode in the yaw motion. The procedure is as follows; first the target mechanical resonance was excited by sending the monochromatic sinusoidal-wave injection using the virtual yaw actuator. After the resonance was well-excited and the amplitude reached a steady state under excitation, we stopped the injection and monitored the time series of the decaying amplitude. The measured decay signal was fitted by a sine wave function with an exponential decay, which can be written as,

$$f(t) = A e^{-t/\tau_e} \sin(2\pi f_0 t + \phi_0) + x_0 \;, \tag{5.1}$$

where τ_e denotes the 1/e decay time when the amplitude decreases by 1/e from a given time, f_0 is the mode frequency, A is the initial amplitude, ϕ_0 is the initial phase, and x_0 is the DC offset, respectively. Sometimes it is difficult to excite a single higher-order mode alone due to the softness of the fundamental mode and resulting waveform becomes a superposition of some sinusoidal waves with different frequencies. In such a case, we assumed that the decay signal was a sum of two different decaying sine waves and fitted by a double-mode waveform written as,

$$f(t) = A_1 e^{-t/\tau_{e1}} \sin(2\pi f_1 t + \phi_1) + A_2 e^{-t/\tau_{e2}} \sin(2\pi f_2 t + \phi_2) + x_0 \;. \tag{5.2}$$

The measured decay signals of the yaw resonant modes are shown in fig. 5.13. As expected by intuition, in a natural state without damping control, the yaw modes have very long decay time more than 100 seconds. Whereas in the 1st mode and 3rd mode the measured signals are clearly observed and well fitted to the theoretical expression, the undamped 2nd mode in fig. 5.13c seems less visible and buried in the 1st-mode signal, owing to its poor observability at the BF. Anyway, these yaw modes with their intrinsic damping will continue for a long time when they are once kicked and can be an issue disturbing the interferometer opertaion.

As we can see in the right panels of fig. 5.13, with the damping control engaged, every yaw mode looks significantly damped in a enough short period of time. The fitting results of the decay time with/without the damping control is sumamrized in table 5.2. It indicates that the damping control at the BF can reduce the exponential decay time of the mechanical resonances in yaw motion and satisfy the requirement of less than 1 minute. Although some mismatches between the measurement and fitting can be seen in the damped oscillation in fig. 5.13, but the inaccuracy of the fitting seems doesn't have an impact on the result of satisfaction of the decay time requirements.

Table 5.2. Fitted decay time of the yaw modes.

Mode	Undamped			Damped		
	f_0 [mHz]	τ_e [s]	Q-factor	f_0 [mHz]	τ_e [s]	Q-factor
#1	21.3	961.4 ± 4.6	64.9	19.3	24.8 ± 0.8	1.5
#2	63.5	158.6 ± 4.6	31.6	62.9	43.9 ± 0.5	8.7
#3	213.3	1155.5 ± 1.9	774.3	215.2	9.5 ± 0.1	6.4

5.3.3   Reduction of RMS residual motion

The amplitude spectral density of the BF yaw with and without the damping control is measured. The result of the spectral measurement is shown in fig. 5.14. While the RMS residual motion in a natural state is dominated by the yaw-mode peaks, these resonant peaks are successfully suppressed by the damping control. When the damping is turned on, the RMS is dominated by the remaining structure around 60–70 mHz which seems to be the residual of the 2nd yaw peak and couplings from the 1st mode of the IP in longitudinal and transverse direction. Suppose that the spectrum below 0.01 Hz is contributed only by the sensor noise, the RMS residual motion in yaw is evaluated as 1530 nrad for the undamped state and 227 nrad for the damped state. This RMS level under the local damping control satisfies the requirement of less than 880 nrad for the lock-acquisition phase, indicating sufficiently small to hand over the angular control to the interferometer loop using the wave front sensor. Note that the higher accumulated RMS of the damped state above 0.2 Hz can be affected by the DC position dependency of the sensor noise floor.
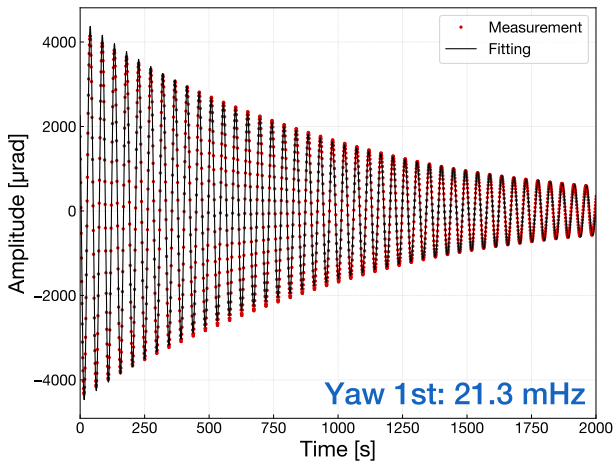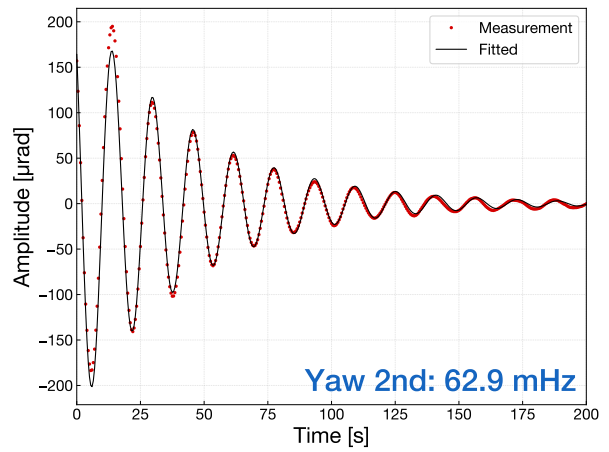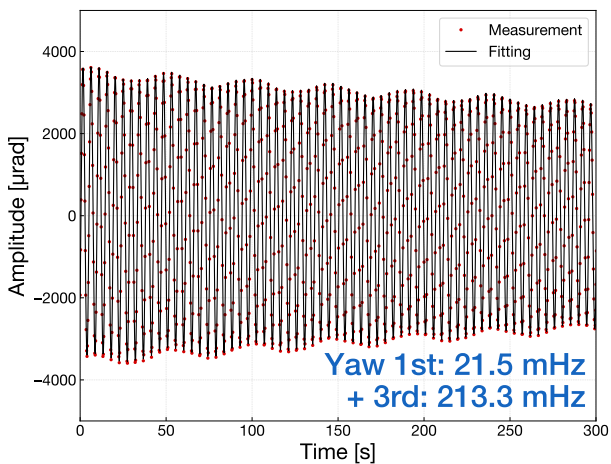
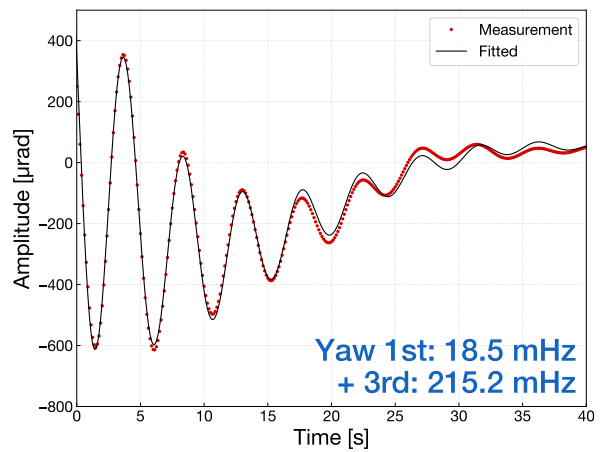**(a)** 1st mode (undamped)
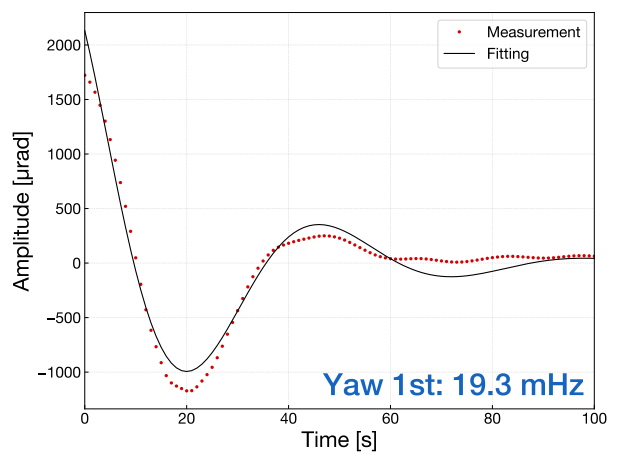
(b) 1st mode (damped)
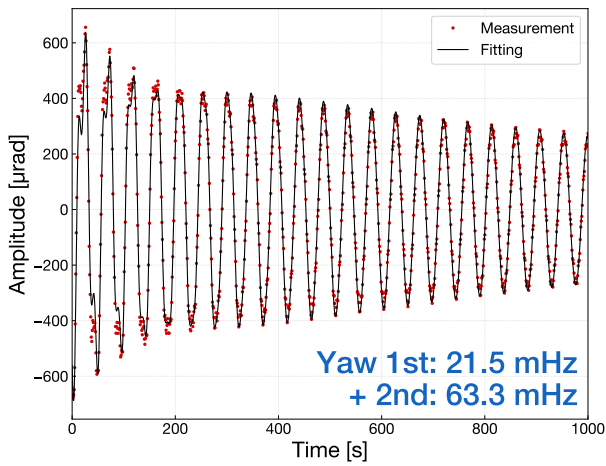
(c) 2nd mode (undamped)
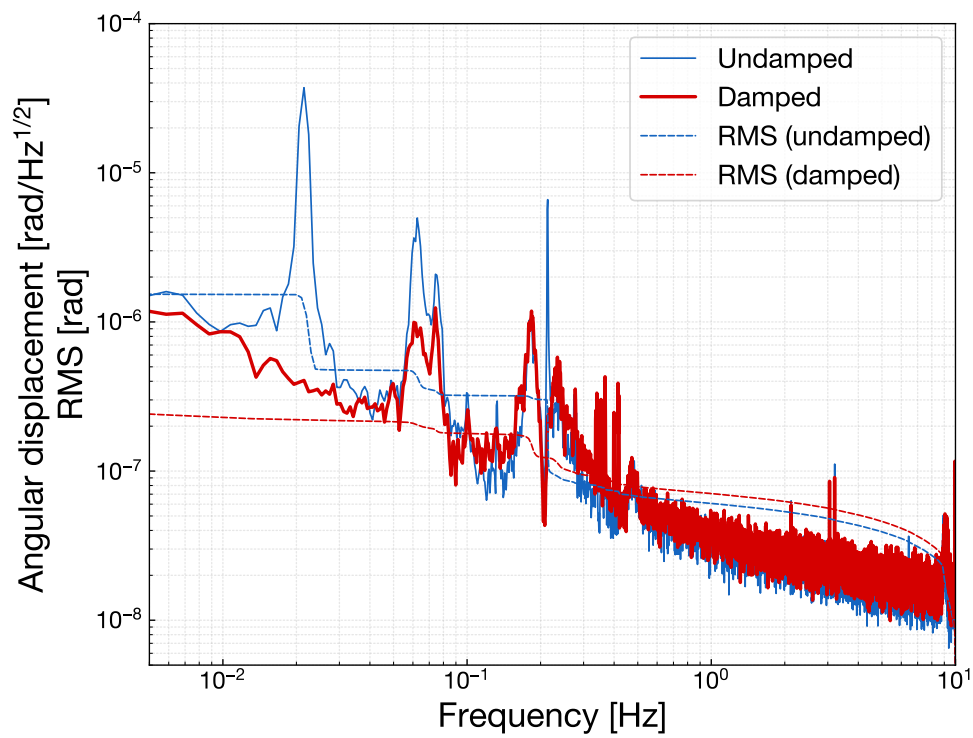

(d) 2nd mode (damped)

(e) 3rd mode (undamped)

(f) 3rd mode (damped)

Fig. 5.13. Decay signals of the yaw modes at the BF. The *left* figures, **(a)**, **(c)**, and **(e)**, are the decay signals without control, while the *right* figures, **(b)**, **(d)**, and **(f)**, are ones with damping loop closed. The fitted frequencies of the sine wave is also annotated in each figure.

Fig. 5.14. Comparison of the amplitude spectral density of the BF yaw with/without the damping control.

5.4 Modal damping for GAS vertical modes

We tested the modal damping mechanism in the vertical control of the Type-A tower. The vertical modes in the full configuration of the Type-A suspension can be divided into two groups, the GAS modes and the payload's internal modes. The GAS modes have mode frequencies in the range of 0.1–1.5 Hz due to the support with soft springs, while the payload's vertical modes are distributed above 4 Hz caused by stiff-spring suspensions. As far as we only consider the lower order modes which often have large impact on the RMS residual motion, the Type-A tower containing all the GAS stages is an adequate setup to demonstrate the lower-order vertical mode control.

The eigenmode matrix necessary to obtain the modal signals was generated by the vertical-DoF submodel extracted from the 3D rigid-body model of the Type-A tower which is also used in the fig. 5.4 for comparison. As discussed in section 5.2, this model has large deviation in the mode shape of the GAS vertical modes from the measured responses. In spite that, we used this imperfect model because it would be able to decouple the lowest-order modes at which frequencies the model prediction and the measurement result show reasonable consistency.

5.4.1 Diagonalization of the sensing and driving matrix

Even if we focus on only the lower order modes, one will predict that the nominal eigenmode matrix derived from the model is not accurate enough to go along with the real-world system. Therefore, we performed diagonalization onto the sensing and driving matrix of the modal sensors and actuators. The diagonalization lets the mode shape included in the sensing and driving matrix be aligned to the one in the actual system.

Suppose that, in an ideal case, the modal displacement signals $\boldsymbol{\eta}$ and the GAS LVDT signals $\boldsymbol{V}_{\mathrm{LVDT}}$ are connected with the following relationship,

$$\boldsymbol{\eta}(t) = \boldsymbol{\Phi}^{-1}\boldsymbol{S}\,\boldsymbol{V}_{\mathrm{LVDT}}(t)\,, \tag{5.3}$$

where $\boldsymbol{\Phi}$ is the eigenmode matrix and $\boldsymbol{S}$ is the conversion matrix from the LVDT signals to the Cartesian displacement signals of the stages. Now the multiplied matrix $\boldsymbol{\Phi}^{-1}\boldsymbol{S}$ is called *sensing matrix* which converts the raw sensor signals to the modal displacements. However, it is not the case in most systems in a real world which have unwanted cross couplings in the DoFs such as,

$$\boldsymbol{\eta}(t) = \boldsymbol{C}_{\mathrm{s}}\boldsymbol{\Phi}^{-1}\boldsymbol{S}\,\boldsymbol{V}_{\mathrm{LVDT}}(t)\,, \tag{5.4}$$

where $\boldsymbol{C}_{\mathrm{s}}$ denotes the coupling matrix, ideally $\boldsymbol{C}_{\mathrm{s}} = \boldsymbol{I}$. Similarly, we can write the incomplete driving matrix for the modal actuators such as,

$$\boldsymbol{A}(t) = \boldsymbol{D}\boldsymbol{\Phi}\boldsymbol{C}_{\mathrm{d}}\boldsymbol{V}_{\eta}(t) \tag{5.5}$$

where $\boldsymbol{A}$ is the feedback signals sent to the real actuators, $\boldsymbol{D}$ is the conversion matrix from the Cartesian feedback signals to the GAS differential actuations. The coupling matrix $\boldsymbol{C}_{\mathrm{d}}$ affects in this case from the right of the *driving matrix* $\boldsymbol{D\Phi}$.

The diagonalization is a procedure to let the coupling matrices, $\boldsymbol{C}_{\mathrm{s}}$ and $\boldsymbol{C}_{\mathrm{d}}$, be identity matrices $\boldsymbol{I}$. For this purpose, one should obtain the coupling matrices with some measurements and update the existing sensing or driving matrix by multiplying the inverse of the derived coupling matrices so that the non-diagonal elements of the coupling matrices turn into zero. In the case of the sensing matrix, the procedure is following:

1. Send a sinusoidal signal with one of the mode frequency and excite the suspension using the incomplete modal actuator.

2. Since the system has a property to store the total energy as a form of its natural vibration, all the modal signals at the excited modal frequency will be dominated by the contribution from the excited mode even by the incomplete modal actuator.

3. After the supension reaches the steady state under the excitation, measure the amplitude spectrum.

4. Calculate the coupling ratio of the non-diagonal modes to the excited diagonal mode from the transfer function at the frequency you excited.

5. Build a coupling matrix with normalizing every column so that the diagonal elements become unity.

6. Update the existing sensing matrix by multiplying the inverse of the derived coupling matrix from the left.

In the case of the driving matrix, the procedure is following:

1. Send broadband Gaussian injection using the incomplete modal actuator and measure the transfer functions from the modal actuator to the all modal sensors.

2. Select a frequency which is well below the all modal frequencies and calculate the coupling ratio of the non-diagonal modes to the excited diagonal mode from the transfer functions.

3. Build a coupling matrix with normalizing every row so that the diagonal elements become unity.

4. Update the existing driving matrix by multiplying the inverse of the derived coupling matrix from the right.

By repeating the procedure several times, the coupling matrices get asymptotically close to identity matrices.

Strictly speaking, the diagonalization of the driving matrix should take the frequency dependence into account since the coulings in the actuator include the mechanical response of the system. Therefore it is desirable replace the driving matrix to a SISO-filter-elemented matrix or a state-space model to implement a multi-input-multi-output (MIMO) operation. Nevertheless, a scalar-elemented driving matrix is chosen in this experiment due to the difficulty of the implementation of frequency dependence. Thus the driving matrix was diagonalized at a low frequency of 0.03 Hz, well below the modal frequencies where the phase of the frequency responses for every mode is aligned to zero.

5.4.2   Vibration in modal basis

After a few times repetition of those diagonalization procedure, the transfer functions of the GAS vetical mode in the decoupled modal basis were measured which is shown in fig. 5.15. As predicted from the modeling accuracy, the modal transfer functions of the lowest two modes, namely 0.155 Hz and 0.421 Hz, can be approximated by the response of a single-DoF oscillation system and hence the modal decomposition was successfully operated. Although the 3rd mode of 0.727 Hz seems also decoupled as well as the 1st and 2nd mode, its response has a non-trivial structure of the parasitic resonance at 1.2 Hz. The response of the following 4th and 5th modes are no longer well-decoupled to single-DoF systems due to the inaccurate guess of the mode frequency and its shape. The DC gain of the modal responses correspond to the inverse of the modal mass in theory since the norm of the eigenvectors are normalized as unity for every mode. However, in the real system the ratios of the DC gain is contaminated by calibration error of the sensors and the individual difference of the actuator efficiency. The uncertainty of the DC gain of the modal responses don't matter in the design of the damping controller since the overall loop gain can be obtained with the measured frequency response.

The modal spectrum of the GAS vertical modes in a stationary state is shown in fig. 5.16. For the 1st and 2nd mode which are well decoupled, their peaks appear significantly, whereas the higher modes don't show any meaningful structure in their spectrum. This can be also explained as the inaccurate modal decomposition for the higher order modes. Seeing the magnitude of the prominence among the noise floor, the 1st mode has the largest amplitude in a stationary state which is consistent with the intuitive understanding. Although the 3rd mode seems even not a little decoupled in the frequency response, there isn't a considerable peak at the corresponding frequency in the spectrum. It implies that in a natural state the higher order modes may store little energy in this vertical system.

The result in this experiment suggests that even if the model includes a measurable
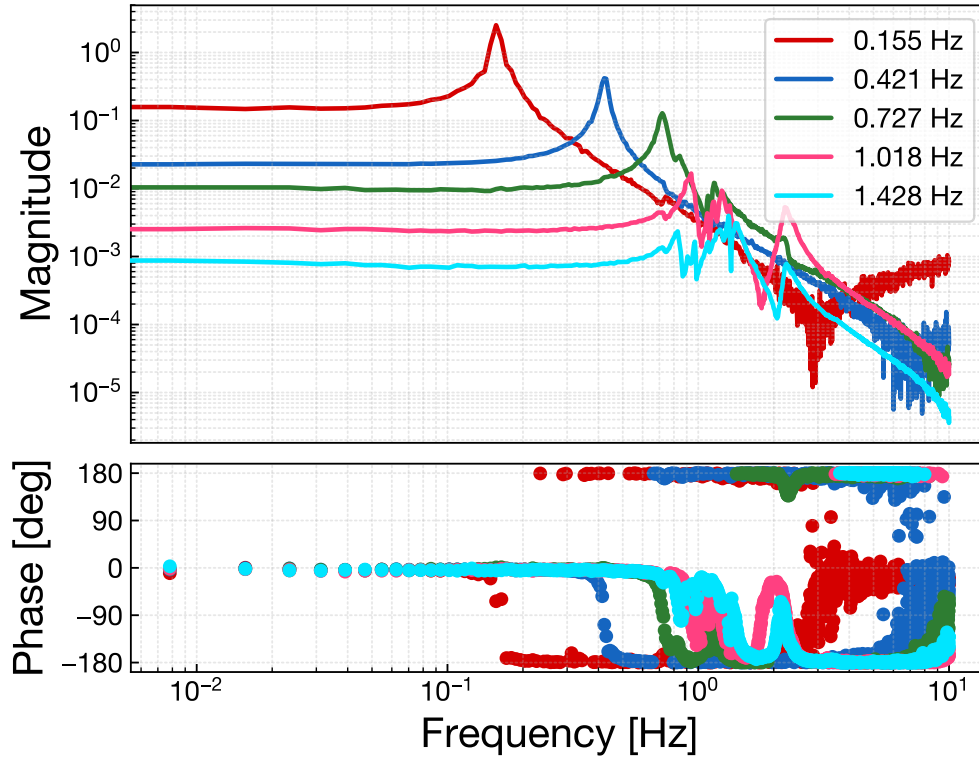
Fig. 5.15. Diagonal transfer functions in the modal coordinate for the GAS vertical modes.

amount of deviations from the real system, the modal decomposition can work on the lower order eigenmodes with the help of diagonalization of the sensing and driving matrices. In the control design of the suspension, we often focus on the lower-frequency mechanical resonances which have large impact on the fluctuation of the suspended optics. Therefore in the cases that the higher order modes are of less importance for the damping control, an model as inaccurate as used in this experiment can achieve the modal decomposition in an acceptable quality.

5.4.3   Damping with modal controllers

We applied the modal damping scheme to the 1st and 2nd mode of the GAS chain which are not only decoupled well with the diagonalized matrices but also having large peaks in a natural state and necessary to be damped. The controllers of the modal damping are the simple SISO filters engaged on the decoupled modal displacement signals. As simulated in section 4.4, the simplified system responses allowed us easily to design a damping filters which are shown in fig. 5.17. The controller has one zero at the 0 Hz and several poles above 1 Hz, resulting feedback force proportional to the modal velocity at the resonant peak and cuting off the high frequency signals. Initially the gains of the control is set so that the peak in the open-loop gain overlaps that in the modal response to realize an almost critical damping.
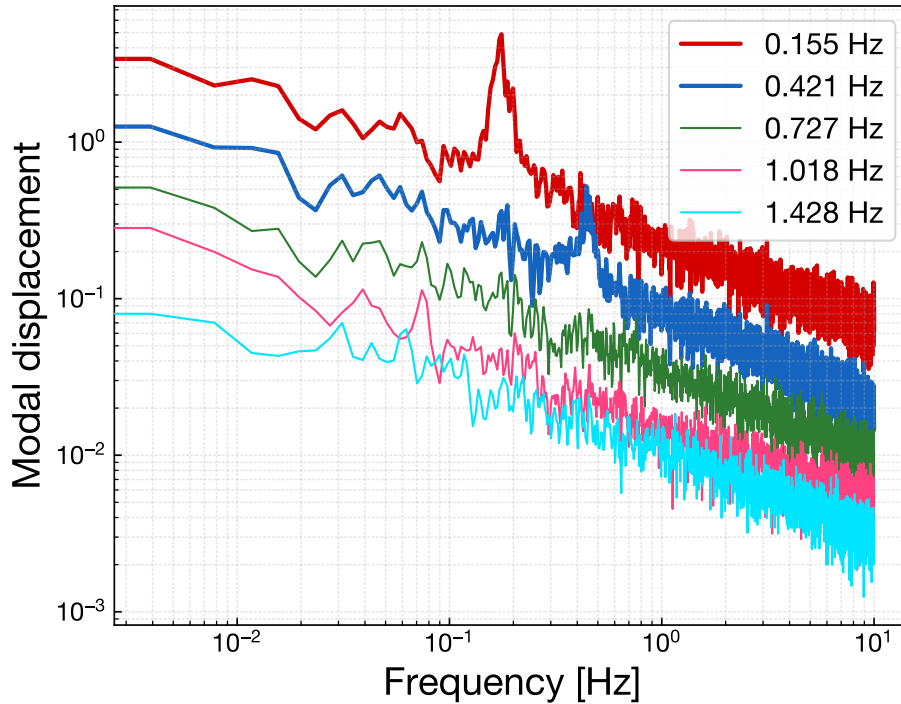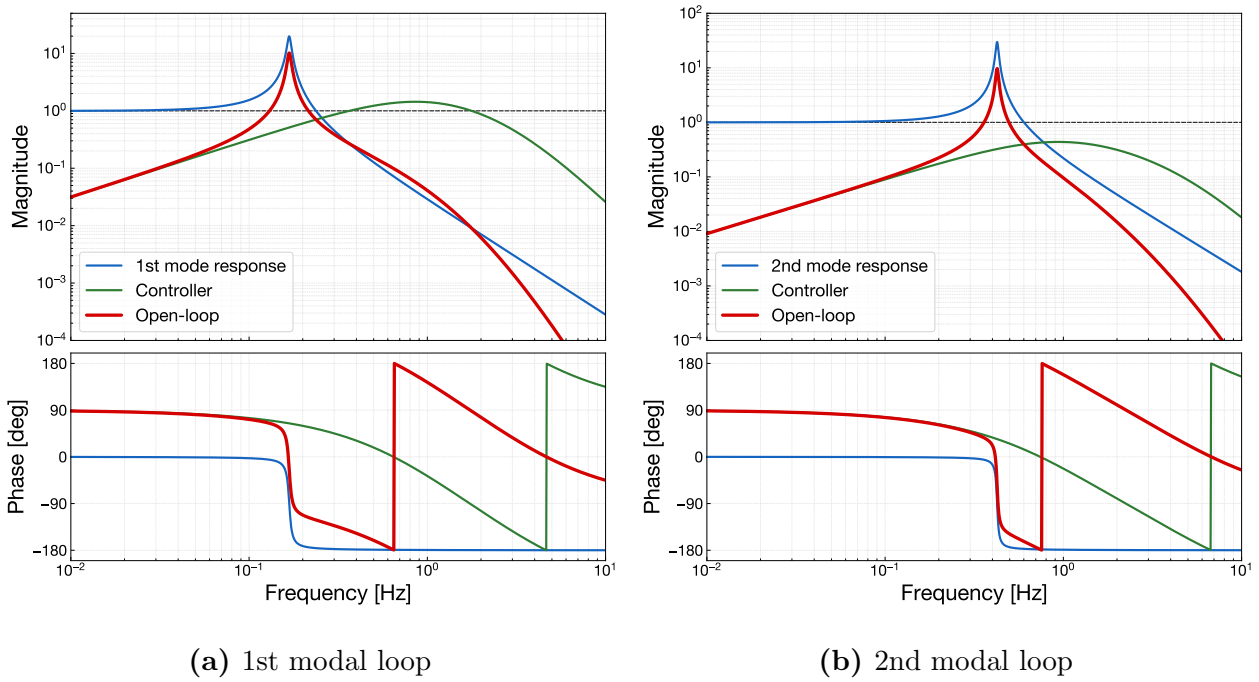
Fig. 5.16. Amplitude spectral density of the GAS in the modal coordinate in a stationary state.

However, through a few times test of engaging the loop, it seemed the initial gain leads to an overdamping condition and thus we adjusted the loop gain to be reduced to the plotted ones in fig. 5.17. Finally the unity-gain frequencies are 0.22 Hz for the 1st modal loop and 0.49 Hz for the 2nd loop, while their corresponding phase margins are 63.3° and 32.8°, respectively.

The result of closing these modal loops can be seen as a spectrum in fig. 5.18. The peaks in a natural state is successfully supressed to a comparable level with the contribution of the sensor noise. Thus we conclude that the modal damping scheme is applicable to the suspension control and can achieve effective damping of the mechanical resonances.

There are still some points which were not tested in this experiment. One is the confirmation of the decay time reduction. As predicted in section 4.4, the controller design of the modal damping should have an advantage to easily achieve the almost critical damping. It can be confirmed by comparing the exponential decay time between the stage-based control and the modal control. This measurement could not be performed in a limited period of the Type-A tower test. Moreover, the impact of noise coupling to the payload under the modal damping control should be tested as a further topic. Therefore, although the basic effectiveness of the modal damping control was validated, its sophisticaed use on the whole suspension control requires further experiments and verifications.

(a) 1st modal loop   **(b)** 2nd modal loop

Fig. 5.17. Open-loop transfer functions of the modal damping control for the GAS vertical modes.
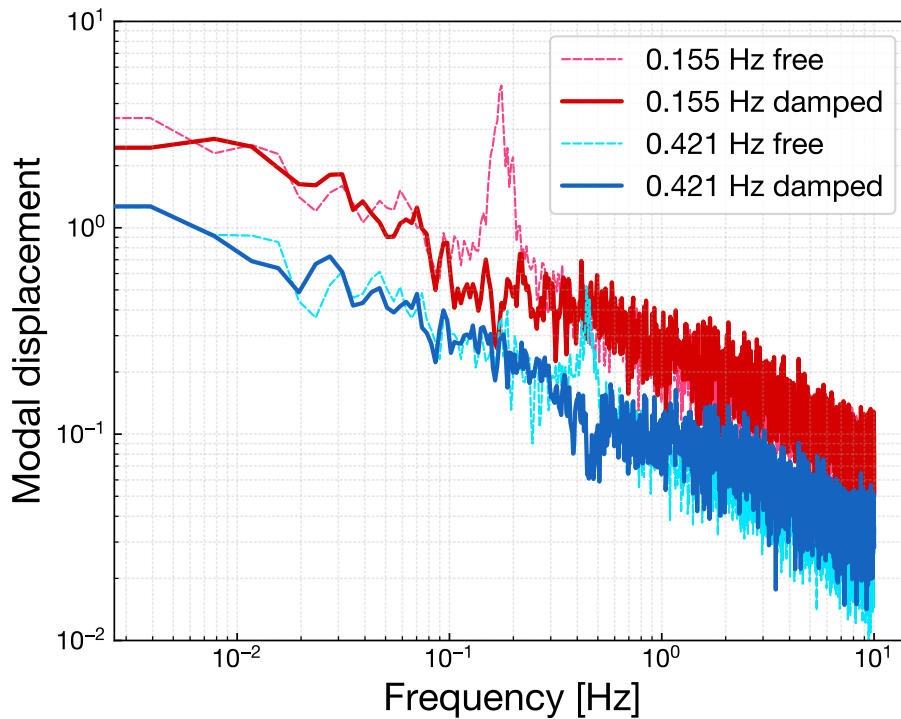
Fig. 5.18. Comparison of amplitude spectral density of the GAS in the modal coordinate with/without the damping control

5.5   Vibration isolation ratio measurement

A measurement of the vibration isolation ratio of the Type-A suspension is performed in a test run of KAGRA. Since the attenuation performance of the Type-A suspension reaches nominally $\sim 10^{-21}$ at 10 Hz, there is little hope to measure the vibration isolation performance directly due to poorer noise limitation of the local sensors. At the time of writing this thesis, KAGRA was in a period of upgrading in which the full-equipped apparatuses are installed and tested to achieve the baseline sensitivity.

The KAGRA test run is held in the configuration of simplified 3-km Michelson interferometer with no arm cavities nor recycling cavities, as illustrated in fig. The two end mirrors are suspended with the Type-A suspension, one is at a room temperature and the other is cooled down to cryogenic temperatures. Similarly, the optics at the center area are also suspended with their dedicated suspensions. The differential length of the Michelson interferometer is controlled by using the reflection light picked off at the Faraday isolator. The signals of this reflected power is fed back to the TM and IM of the beam splitter (BS) with the crossover frequency of ~ 0.1 Hz and the overall unity gain frequency of ~ 50 Hz. For alignment control, the ETMY mirror is stabilized by local feedback with an optical lever, while the ETMX mirror is controlled with global feedback so that the reflected light from the ETMX follows that from the ETMY projected on the BS.

The strain sensitivity of the interferometer during the engineering run is shown in fig. 5.19. Through the noise study, we found that the sensitivity was limited by angular control noise below 50 Hz and by the dark noise of the photodiodes receiving the error signal for the Michelson interferometer length control. Further discussions about the inteferometer sensitivity and stability can be seen in [**Akutsu2019**].

The method to obtain the vibration isolation ratio is a combination of direct transfer function measurements and an estimation with the tuned suspension model. We resolved the vibration isolation ratio into two factors, the transfer function from the ground to the top stage and the one from the top stage to the mirror at the bottom. The first transmission factor is identified by measuring transfer functions from the force exerted on the IP stage to the displacement of the longitudinal sensors at the IP and the BF. The measured transfer functions which are shown in fig. 5.20, were properly matched with the model predictions derived from the 3D rigid-body model of the full Type-A suspension. Due to the shortage of the actuation power, the measurement to the BF got deviated at the high frequencies above 1.5 Hz. Nevertheless, we can see a great consistency between the measurement and the model even in the peak distribution over the frequencies, although a tiny offset of the peak frequency for some higher order modes can be recognized.

Based on the consistency of the real system characteristics and the model prediction, we assumed that the model can generate an confident estimation of the vibration isolation ratio
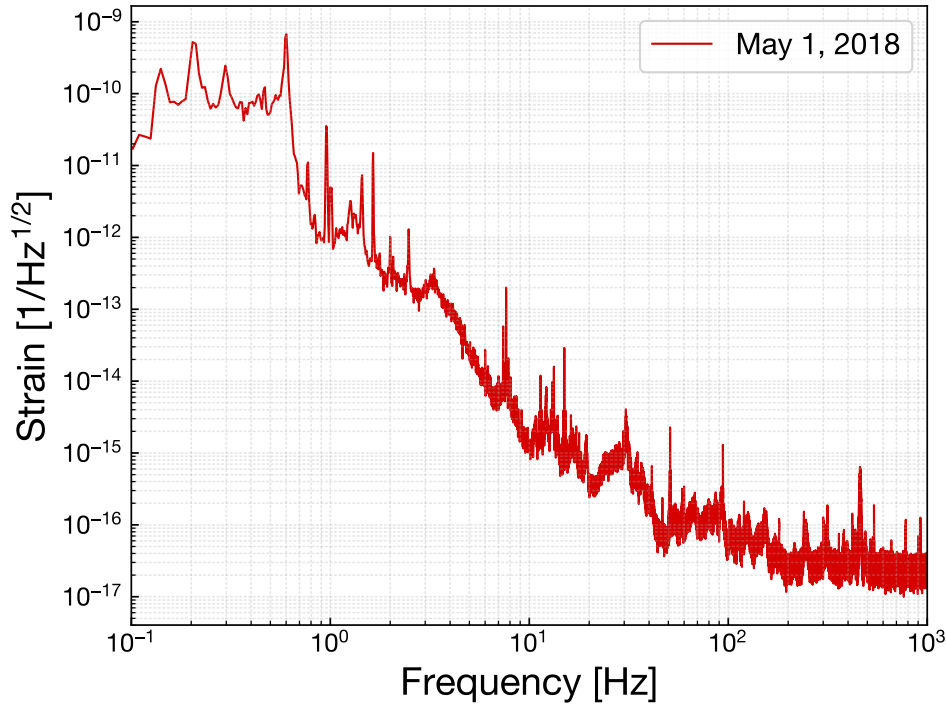
Fig. 5.19. Calibrated strain sensitivity of the KAGRA in the first engineering run.

for the installed Type-A suspension. Thus, since it is difficult to measure the transfer function from the seismic displacement to the IP stage, we derived it from the confident model which is shown in fig. 5.21.

The vibration transmission from the IP stage to the test mass was measured by sending a monochromatic sinusoidal injection to the IP and then monitoring the error signal of the Michelson interferometer length control. The sampled frequency of the excitation is chosen so as not to excit the mechanical resonance of the Type-A suspension since large disturbance may break the lock of the interferometer. Although the error signal of the Michelson interferometer can include the information of the other end mirror or the BS, the output is correlated with the excited IP displacement which is confirmed by measuring the coference of the local sensor of the IP and the inteferometer output.

Finally the vibration isolation ratio of the Type-A suspension was estimated by combining the derived model and the measured vibration transmission which is shown in fig. 5.22. In spite of the careful selection of the excitation frequency and amplitude, the extreme attenuation performance of the Type-A suspension didn't allow us to measure the well-correlated transfer function above 1.8 Hz. In addition, the calibration procedure was guaranteed in the frequencies down to ~ 0.5 Hz due to the response of the BS payload where the error signal of the Michelson interferometer was fed back. For these reasons, only the frequency points in 0.8–1.7 Hz could be measured with a coherence more than 0.6.
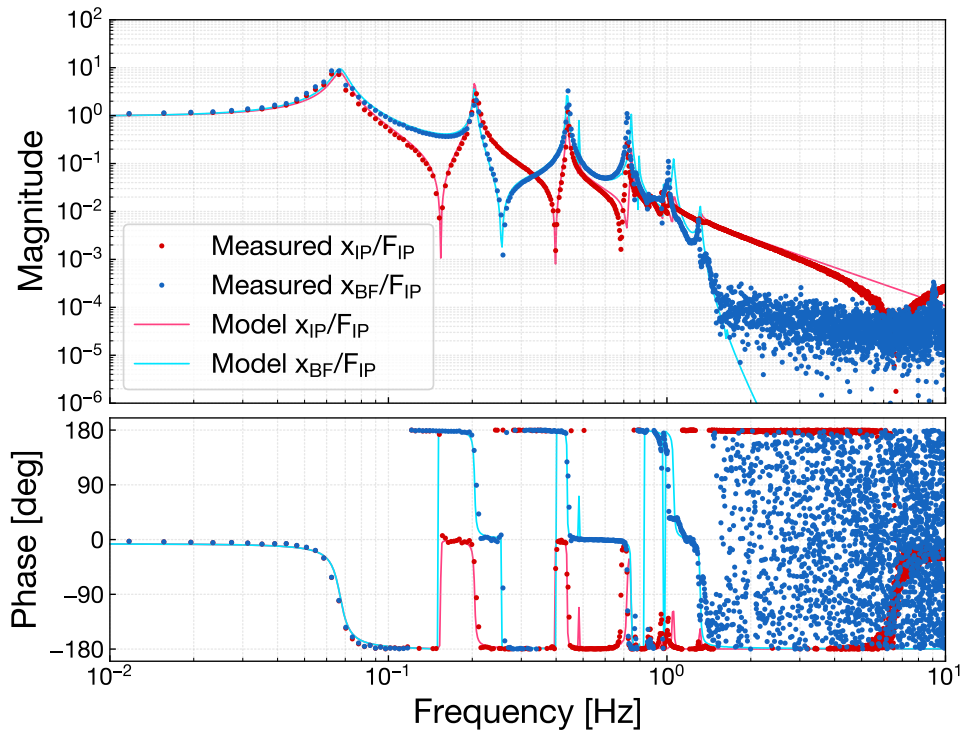
Fig. 5.20. Transfer functions from the force on the IP to the local sensor at the IP and BF in longitudinal direction of the full Type-A suspension.

The total tendency of the vibration isolation ratio seems appearing as expected. However, although the measured transfer functions were matched enough with the model in fig. 5.20, the vibration isolation ratio has some deviation from the model at the frequencies below 1.4 Hz in fig. 5.22. Seeing a zoomed subfigure in fig. 5.22, the maximum difference between the measurement and the model is at most an order of magnitude at 1.065 Hz. These distinguished points from the model prediction can be caused by some possible reasons: one is the inaccurate modeling of the cryogenic payload. The resonant peaks aroung 1 Hz will originate from the internal modes of the payload such as not only the pure longitudinal modes but also the coupled pitch modes both of which have resonances in this frequency region. In this study, the characterization of the payload was not covered in its scope, the improvement of the model based on the transfer function measurements in the DoFs of the payload can resolve the mismatch of this result. Another possible cause of the mismatch is the error in the calibration procedure of the Michelson interferometer. The calibration assumed a simple f^{-2}-response in the actuator including the BS response, whereas it is known that the BS has a resonant peak at 0.5 Hz in its longitudinal response. It can contribute the deviation of the measured vibration isolation ratio from the model prediction in the low frequency.

Even based on the possible concerns about the mismatch in this measurement mentioned above, the model has some extent of reasonanble consistency with the real system of the
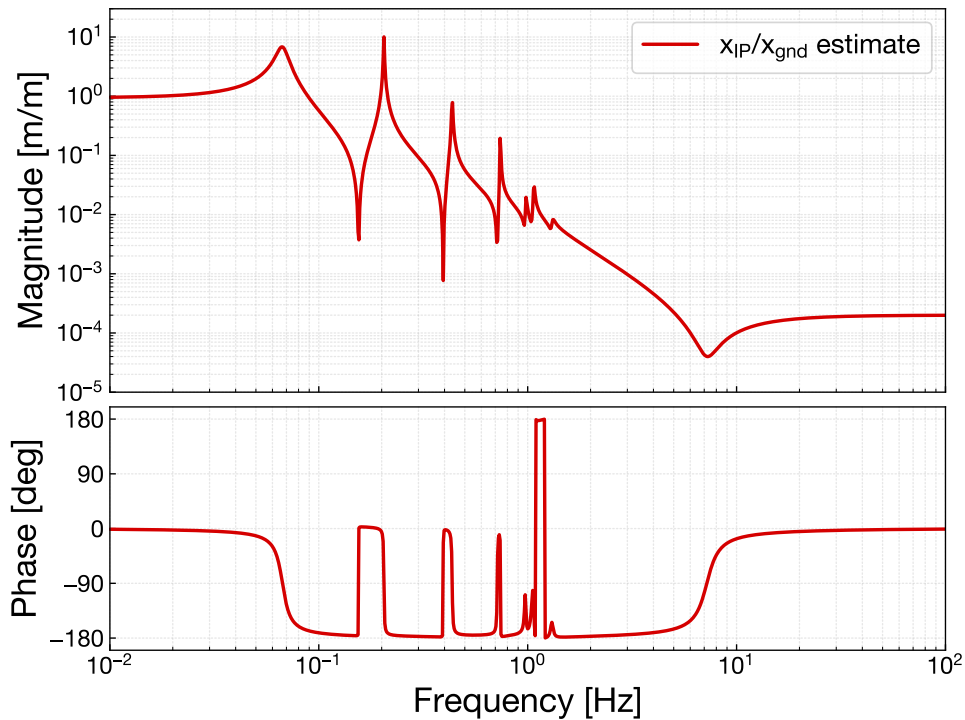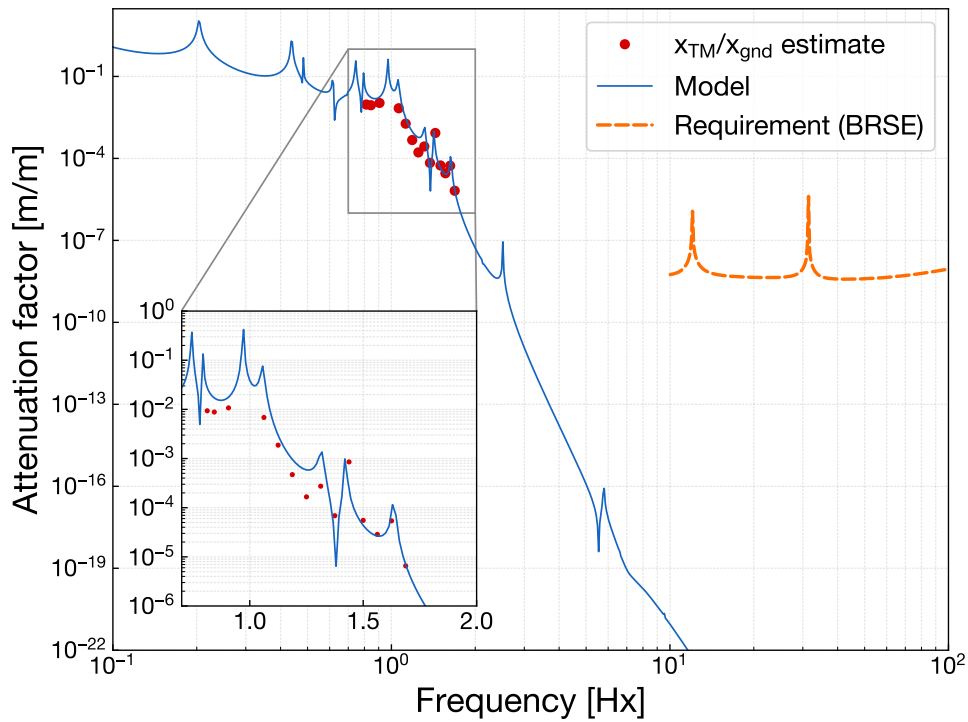
Fig. 5.21. Estimated vibration isolation ratio from the ground to the IP stage.

Type-A suspension. Thus, by extrapolating the estimated vibration isolation ratio to the high frequencies, we can obtain an indication of the vibration isolation performance of the constructed Type-A suspension. Taking the saturation effect of the IP into account, the seismic attenuation factor of the Type-A suspension at 10 Hz is estimated as 9×10^{-22}, plotted as a blue curve in fig. 5.22. Assuming the seismic noise model of the KHNM, the requirement of the vibration isolation ratio corresponding to the required longitudinal displacement noise can be also derived. Comparing the estimated vibration isolation ratio to the requirement of 5×10^{-9} at 10 Hz, the Type-A suspension possesses sufficient capability to attenuate the seismic noise coupling in purely longitudinal direction.

It would be seen that the Type-A suspension with the estimated performance is over engineered against the requirement. Although this attenuation performance in longitudinal direction is the result of a number of stages cascaded from the top, this design aims rather to secure the vibration isolation in vertical direction. The five stages of the GAS filter chain is a reasonable design to reduce the contribution to the displacement noise through vertical-to-longitudinal coupling. Thus it is necessary to confirm the vibration isolation performance in vertical direction which we put off as a subject of forthcoming tests.

The future upgrade of this experiment is the direct measurement of the in-band seismic attenuation performance using the interferometer with arm cavities. The measurement reported in this section could argued no further than the in-band vibration isolation ratio with

Fig. 5.22. Estimated vibration isolation ratio from the ground to the mirror (TM).

the model estimation since the measured data covers only a limtied frequency region. It can be overcome by using the cavity-implemented interferometer with an outstanding sensitivity. In addition, unlike this experiment, the performance should be tested with the payload in a cryogenic temperature which is the actual operational condition.

Chapter 6

Conclusion

In this study, we developed the Type-A suspension, a vibration isolation system for the test masses in KAGRA. We have constructed so-called Type-A tower which is the key part for the vibration isolation. Through the experiments summarized below, we concluded that the installed Type-A tower can provide sufficient seismic attenuation and control performance in order to achieve the design sensitivity of the KAGRA interferometer. There is still necessity of testing the Type-A suspension after integration with the cryogenic payload and through commissioning of the global system in many aspects, this study has contributed to accomplishment of KAGRA toward the beginning of gravitational wave observation.

System characterization

The system characterization validated that the installed Type-A tower system basically has the designed dynamic characteristics which satisfies the requirements. The frequency responses of the Type-A tower are measured and compared to the predictions of the nominal model. Although there is some amount of deviation, the obtained frequency responses can be regarded as acceptable to achieve the required vibration isolation performances except for the vertical direction. As for the vertical direction, the dynamics of the Type-A tower shows discrepancies between the measurement results and the model predictions, in particular in the mode shapes of its higher order resonances. It is suspected that the higher order oscillatory behavior has stronger dependence on the divergence of the mechanical parameters from the nominal values. However, due to the facts that the higher order modes have smaller impact on the RMS residual motion and that the measured mode frequencies are roughly distributed as expected, the discrepancies in the vertical mode dynamics seem to be within the permissible range. This tolerance is also plausible from the measured displacement spectrum at the dummy payload which is suspended instead of the actual cryogenic payload. One problem still remains is the effect of couplings from non-straightforwardly-controllable degrees of freedom such as a tilt of the middle GAS filter stages. The impact of the couplings on the test mass

or the interferometer should be confirmed after integration with the cryogenic payload.

Torsion mode damping

Torsion mode damping of the Type-A tower is tested. Since a major fraction of the height of the Type-A suspension is accounted by a series of single suspension wires, the system possesses a behavior of a torsion pendulum with extremely low stiffness and then have a long duration of the torsional modes which turns to an issue in stabilizing alignment of the mirror. The Type-A tower is responsible to address this issue by providing a function of active damping control at the tower's bottom stage. The test of torsion mode damping proves that the long exponential decay time of the resonances can be successfully reduced to less than 1 minute by the active feedback control. In addition, the in-loop sensor indicates that the RMS residual angular fluctuation in torsion is suppressed sufficiently to a level of acquiring arm cavity lock. Therefore, it is concluded that the Type-A tower has satisfactory performance of the torsion mode damping.

Implementation of odal damping

This study presented an advanced control scheme called modal damping. The modal damping processes feedback signals in a decoupled modal basis instead of a conventional Cartesian basis, allowing us to simplify the servo design optimization and to access efficient actuation for a coupled oscillatory system. The control test demonstrates feasibility of modal damping for the coupled vertical modes of the Type-A suspension. Deriving a conversion law between the Cartesian basis and the modal basis from the mathematical model, coupled signals of the vertical modes can be decomposed into those of each orthogonal eigenmode. Moreover, the result of the modal damping shows that the eigenmodes can be damped independently of other modes. Although the availability of modal controllers is validated only for the vertical modes in this test, one can expect to apply this technique to other stages having less-powerful actuators such as the cryogenic payload.

Measurement of vibration isolation ratio

The installed Type-A tower was integrated with the cryogenic payload and incorporated into a global system of the KAGRA interferometer. This thesis includes the measurement of the vibration isolation ratio from the ground to the test mass. During the first cryogenic test operation of the simplified 3-km Michelson interferometer, we measured the vibration transmissivity from the top stage to the error signals of the inteferometer output. Combining the measured result with a model prediction of the transmissibity from the ground to the top stage derived from the tuned mathematical model, the total vibration isolation ratio of the Type-A suspension is estimated as 9×10^{-22} for the pure longitudinal contribution at 10 Hz.

Although the estimated result is pursued by some amount of mismatch with respect to the nominal model prediction, the seismic attenuation performance of the real system seems to be a reasonable level to achieve the design sensitivity of KAGRA.

Bibliography

[1]   B. P. Abbott et al., *Astrophys. J.* **818** (2), p. L22, (2016). "Astrophysical implications of the binary black hole merger GW150914", (cited on p. 14).

[2]   B. P. Abbott et al., *Phys. Rev. Lett.* **119**, p. 141101, (2017). "GW170814 : A three-detector observation of gravitational waves from a binary black hole coalescence", (cited on p. 15).

[3]   B. P. Abbott et al., *Phys. Rev. Lett.* **119** (16), p. 161101, (2017). "GW170817: Observation of Gravitational Waves from a Binary Neutron Star Inspiral", (cited on p. 15).

[4]   B. P. Abbott et al., *Phys. Rev. Lett.* **116** (6), pp. 1–16, (2016). "Observation of gravitational waves from a binary black hole merger", (cited on p. 14).

[5]   F. Acernese et al., *Astroparticle Physics*, **20** (6), pp. 617–628, (2004). "A local control system for the test masses of the Virgo gravitational wave detector", (cited on p. 88).

[6]   T. Akutsu et al., *Prog. Theor. Exp. Phys.* **2018** (1), pp. 1–23, (2018). "Construction of KAGRA: an underground gravitational-wave observatory", (cited on p. 51).

[7]   Y. Aso et al., *Phys. Rev. D*, **88** (4), p. 043007, (2013). "Interferometer design of the KAGRA gravitational wave detector", (cited on p. 50).

[8]   E. D. Black, *Am. J. Phys.* **69** (1), pp. 79–87, (2001). "An introduction to Pound–Drever–Hall laser frequency stabilization", (cited on p. 63).

[9]   Y. Enomoto, Y. Michimura, and K. Izumi, *KAGRA Internal Document*, **JGW-T1808343**, (2018). "Definitions for the X arm commissioning", (cited on p. 65).

[10] URL: https://www.gw-openscience.org/catalog/ (cited on p. 15).

[11] K. Izumi, *Master's Thesis*, University of Tokyo, (2009). "レーザー干渉計型重力波検出器のための Fabry-Perot 共振器の共振引き込み研究", (cited on p. 64).

[12] Y. Michimura et al., *Class. Quantum Grav.* **34** (October), p. 225001, (2017). "Mirror actuation design for the interferometer control of the KAGRA gravitational wave telescope", (cited on p. 83).

[13] A. J. Mullavey et al., *Optics Express*, **20** (1), p. 81, (2012). "Arm-length stabilisation for interferometric gravitational-wave detectors using frequency-doubled auxiliary lasers", (cited on p. 64).

[14] T. Sekiguchi, *PhD thesis*, University of Tokyo, (2016). "A Study of Low Frequency Vibration Isolation System for Large Scale Gravitational Wave Detectors", (cited on pp. 62).

[15] H. Tariq et al., *Nucl. Instrum. Methods Phys. Res. A*, **489** (1-3), pp. 570–576, (2002). "The linear variable differential transformer (LVDT) position sensor for gravitational wave interferometer low-frequency controls", (cited on p. 79).

[16] C. Wang et al., *Nucl. Instrum. Methods Phys. Res. A*, **489** (1-3), pp. 563–569, (2002). "Constant force actuator for gravitational wave detector's seismic attenuation systems (SAS)", (cited on p. 82).